Development of a test setup for miniature antennas for millimeter frequencies

Yan Fu

UNIVERSITÉ DE GRENOBLE

THÈSE

Pour obtenir le grade de

DOCTEUR DE L'UNIVERSITÉ DE GRENOBLE

Spécialité : **Optique et radiofréquence**

Arrêté ministériel : 7 août 2006

Présentée par

Yan FU

Thèse dirigée par **Fabien NDAGIJIMANA**
codirigée par **Laurent DUSSOPT** et
co-encadrée par **Tan - Phu VUONG**

préparée au sein du **Laboratoire IMEP-LAHC**
dans **l'École Doctorale EEATS**

Development of a test bench for characterization of integrated antennas at millimeter-wave frequencies

Thèse soutenue publiquement le **18 juillet 2012**,
devant le jury composé de :

M. Mohamed HIMDI
Professeur, Ecole Supérieure d'Ingénieurs de Rennes, Président
M. Cyril LUXEY
Professeur, Université de Nice Sophia-Antipolis, Rapporteur
M. Moncef KADI
Enseignant-chercheur, ESIGELEC/IERSEEM, Rapporteur
M. Romain PILARD
Ingénieur, ST Microelectronics, invité
M. Fabien NDAGIJIMANA
Professeur, Université Joseph Fourier, Directeur de thèse
M. Laurent DUSSOPT
Ingénieur, CEA/LETI, Co-directeur de thèse
M. Tan - Phu VUONG
Professeur, Grenoble INP, Co-encadrant de thèse

Acknowledgement

I would like to express my deep and sincere gratitude to my supervisors, Professor Fabien Ndagijimana at IMEP-LAHC and Laurent Dussopt at CEA-LETI, for their patient guidance and inspiration. Their profound knowledge and enthusiasm repeatedly helped me to overcome the unexpected-yet-inevitable difficulties that I encountered during my thesis. Working with them is also a pleasure thanks to their great sense of humor. Likewise, I express my great appreciation to my co-supervisor Tan-Phu Vuong at IMEP-LAHC for his scientific support during this thesis.

I thank Professor Mohamed Himdi from the Ecole Supérieure d'Ingénieurs de Rennes, Professor Cyril Luxey from the Université de Nice Sophia-Antipolis, Professor Moncef Kadi from ESIGELEC/IERSEEM and Romain Pilard from ST Microelectronics for kindly accepting to be my reviewers and jury members for this thesis and for their interesting questions and discussions during the defense.

I am also extremely grateful to the all the people at the IMEP-LAHC Laboratory for their help, particularly Nicolas Corrao, for being permanently available to re-calibrate the apparatus. Furthermore, I would thank to Irene Pheng at CIME Nanotech, for her dedication in realizing the flip-chip connection.

I would also like to thank to my friends, Alina Ungureanu, Leonce Mutwewingabo, Karim Haj Khlifa, Walaa Sahyoun, Xin Xu, Yong Xu, Xiaolan Tang, Jing Wan, Cuiqin Xu, Tekfouy Lim, Tong Shao, Lin You, Chuan-Lun Hsu, Fanyu Liu, Hao Shen. Thanks for the friendship and we really had very good time together.

Finally, I thank all the members of my family and Dr. Christopher Dance for their persistent support and encouragement.

Contents

List of abbreviations

The following table describes the significance of various abbreviations and acronyms used throughout the thesis.

Abbreviation	Meaning
AC	Alternating Current
ACP	Air CoPlanar
Al	Aluminum
APDs	Avalanche Photo-Detectors
AR	Axial ratio
Au	Gold
AUT	Antenna Under Test
BOX	Buried OXide
CEPT	European Conference of Postal and Telecommunications Administrations
CPS	CoPlanar Stripline
dB	Decibel
DC	Direct Current
DUT	Device Under Test
ECC	Electronic Communications Committee
EDFA	Erbium-doped fiber amplifier
EFO	Electronic Flame-Off
FCC	Federal Communications Commission
GS	Ground-Signal
GSG	Ground-Signal-Ground
HDMI	High Definition Multimedia Interface
HR	High Resistivity
IC	Integrated Circuits
IMD	Inter Metal Dielectric
LTCC	Low-Temperature Co-fired Ceramic
MEMS	MicroElectroMechanical Systems
MMIC	Monolithic Microwave Integrated Circuits
MZM	Mach-Zehnder-Modulator
PC	polycarbonate
PD	Photo-Detector
PDMS	PolyDiMethylSiloxane
PEN	PolyEthylene Naphthalate
PES	PolyEtherSulfone
PET	Polyethylene terephthalate
PI	PolyiMide

PMD	Pre Metal dielectric
PR	PhotoReceiver
RCS	Radio-Cross-Section
Si3N4	Nitride
SiO2	Silicon oxide / Silicide
SIP	System In a Package
SG	Signal-Ground
SIW	Substrate Integrated Waveguide
S-MMIC	Submillimeter-wave Monolithic Integrated
SoC	System On a Chip
SOI	Silicon On Insulator
SOLT	Short-Open-Load-Through
STI	Shallow Trench Isolation
TC	Thermocompression
T-line	Transmission line
TS	Thermosonic
TSV	Through-Silicon-Vias
US	Ultrasonic
UTC-PD	Uni-Ttravelling-Carrier Photo-Detector
VCO	Voltage-Controlled Oscillator
VNA	Vector Network Analyzer
WLAN	Wireless Local Area Networks
WPAN	Wireless Personal Area Networks

General Introduction

I Problem

There is increasing demand for high data-rate and short-range wireless communications. For instance, multi-Gbps high-definition media streams could be transmitted simultaneously between different devices in a household. The 60 GHz band is a good candidate for such applications as in the 60 GHz band a large free licensed spectrum is available. In this range of frequencies, there has recently been an intensive study of fully-integrated front-ends with low-directivity antennas using different micro-system technologies.

However due to the small size of millimeter-wave antennas (smaller or of the order of 1 mm in dimension) their characterization is sensitive to the testing environment. This is particularly the case for antennas with large beamwidth, eg omni-directional antennas, which are difficult to characterize as the size of the testing apparatus (such as RF probes, connecting bond wires and transmission lines) is much bigger than the AUT (antenna under test). One consequence is the masking effect caused by the apparatus on a significant angular sector of the radiation pattern. Another consequence is the reflection and scattering effects of the waves radiated by the antenna on the apparatus. Thus the characterization of integrated antennas has been a blocking point for the validation and further study of the integrated antennas at millimeter-wave frequencies.

II Objective of the thesis

In order to solve the problem, we firstly designed and fabricated an original 3D gain characterization test bench on which experiments were performed. This is a semi-automatic setup with a compact dimension of 90×60×65 cm^3 and it is designed for integrated antennas with frequencies above 26 GHz.

Then we studied three techniques for feeding the AUT: the probe-fed technique, the flexible-transmission-line-fed technique and the RCS (Radio-Cross-Section) method. First we address the probe-fed technique, where instead of using a standard probe

which provokes a limited effective scanning zoom [-10° 90°] and significant ripples, we propose two customized probes with a coaxial extension of 5 cm. One probe has a custom orientation for its connector and the other has a reversed orientation for its connector. Using these two customized probes, we significantly improve the performance of radiation gain pattern characterization: the scanning zone achieves [-50° 90°] for the long probe with customized connector and [-76° 90°] for the long probe with reversed connector. Furthermore, the ripples decrease with both customized probes.

Next we address the flexible-transmission-line-fed technique. The main advantage of this technique is that it is easy to use and the there is no masking zone. We used a flip-chip connection to avoid suspending bond wires thereby having better control of the impedance match. This technique improves the scanning zone to [-90° 90°].

Finally we study the radar-cross-section (RCS) method. In this technique, the AUT is connected to three different loads (50Ω, short, open). The simulation results demonstrate that there is insufficient variation in the ratio of received power to incident power as the load on the AUT is varied in order to make precise measurement with conventional measurement equipment.

This thesis was done in the laboratory IMEP-LAHC (l'Institut de Microélectronique Electromagnetisme et Photonique et LAboratoire d'Hyperfréquences et de Caractérisation) in cooperation with CEA-LETI (Commissariat à l'Energie Atomique - Laboratoire d'Electronique des Technologies de l'Information). The type of the thesis is a BDI (Bourses de docteur ingénieur), financed by the CNRS (Centre National de la Recherche Scientifique).

III Structure of the thesis

Chapter I presents the state of the art, pre-existing millimeter-wave test benches and some feeding techniques. These techniques include the probe-fed technique, waveguide-fed technique, transmission-line-fed technique, optical-link-fed technique and the VCO-fed technique.

Chapter II is a presentation of some antenna characteristics and two integrated antennas with low-directivity that we used for the radiation pattern characterization.

One is an integrated spiral antenna on CMOS SOI and the other one is an integrated folded dipole on high-resistivity silicon.

Chapter III presents a new 3D low-directivity integrated antenna test bench and a customized probe-fed technique.

Chapter IV presents the characterization of integrated antennas at millimeter-wave frequencies with a flexible line. To achieve this, we designed, fabricated and validated a transmission line on a flexible substrate. We connected this transmission line with the AUT using modified flip-chip technique.

Chapter V is about a feasibility study of characterization of an integrated antenna using a RCS method.

The thesis finishes with a general conclusion and outlook for future work.

Chapter I
State of the art

I Introduction

Millimeter waves are waves whose wavelength is between 1 mm to 10 mm. For electromagnetic waves in free space, this corresponds to frequencies roughly between 300 GHz and 30 GHz. The very first millimeter wave applications were in radio astronomy [1-4], and meteorology, where clouds and precipitation can be sensed with the help of a millimeter-wave radar, for instance to investigate the sizes, motions and distribution of cloud particles [5-9]. Millimeter waves are also widely used in military and defense applications [10-13]. More recently they are of substantial interest for commercial applications, such as short-range high date rate wireless communications in the 60 GHz band, such as automotive radar systems at the allocated frequency band of 76-77 GHz, which enable long-range intelligent cruise controls [14-17] and such as radar, imaging systems, remote sensing and active denial for the homeland security in the 94, 120 and 194 GHz bands [18-20].

There is a perceived latent demand for radio-communications at higher data-rates than the data-rates that are presently widely available for radio-communication. This has prompted the commercial sector, from startups to large multi-national companies, to investigate the appropriate choice of frequency bands for such applications. Generally speaking, the outcome of these investigations is an investment in research and development in the 60 GHz band.

In particular there is a significant demand in the following high-data-volume markets: short-range high-data-rate connections via Wireless Personal Area Networks (WPAN); Wireless Local Area Networks (WLAN); and real-time video streaming wi-HDMI (high definition multimedia interface). The idea is that in future, multiple Gbps media streams will be shared simultaneously across multiple devices connected to the same WLAN.

The 60 GHz band is usually the selected candidate for such envisioned applications for three main reasons. Firstly, a large proportion of this band is free spectrum, as

shown in Table 1. In particular, no license is required in the US by the Federal Communications Commission (FCC) for this band, and in Europe, 9 GHz around the 60 GHz band is freely-licensed by the Electronic Communications Committee (ECC) of European Conference of Postal and Telecommunications Administrations (CEPT) [21]. One potential reason for requiring no license for this band is the high absorption and attenuation of such frequencies by oxygen and water (rain) which is illustrated by Figure 1.

This limitation is in fact the second reason for interest in the 60 GHz band for short-range applications. In other words, the high attenuation makes it possible to ensure some network security. Therefore, let us re-examine Figure 1. 1. Line A shows the attenuation as a function of frequency at sea level, at 20℃, a humidity density of 7.5 g m^{-3}, while line B is for 4 km elevation, 0 ℃ and a humidity density of 1 g m^{-3} [18]. We can see that oxygen and water resonate at certain frequencies leading to a peak in attenuation in the 60 GHz band. Figure 1. 2 shows the atmospheric attenuation as a function of the rainfall rate. We can see that attenuation increases with frequency. These attenuation characteristics limit the data transmission distance in the presence of oxygen and water, hence increasing network security. Finally, a third reason for interest in the 60 GHz band is its high propagation loss, since this loss leads to limited wall penetration, resulting in low likelihood of interference with other systems.

Table 1: Wireless unlicensed 60 GHz bands.

Region	**USA / Canada**	**Europe**	**Japan**	**Korea**	**Australia**
Band (GHz)	57.0-64.0	57.0-66.0	59.0-66.0	57.0-64.0	59.4-62.9

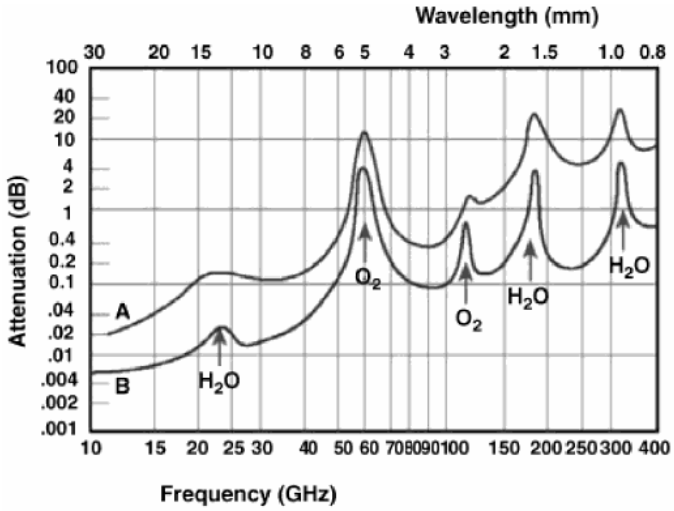

Figure 1. 1 Average atmospheric absorption of millimeter waves.

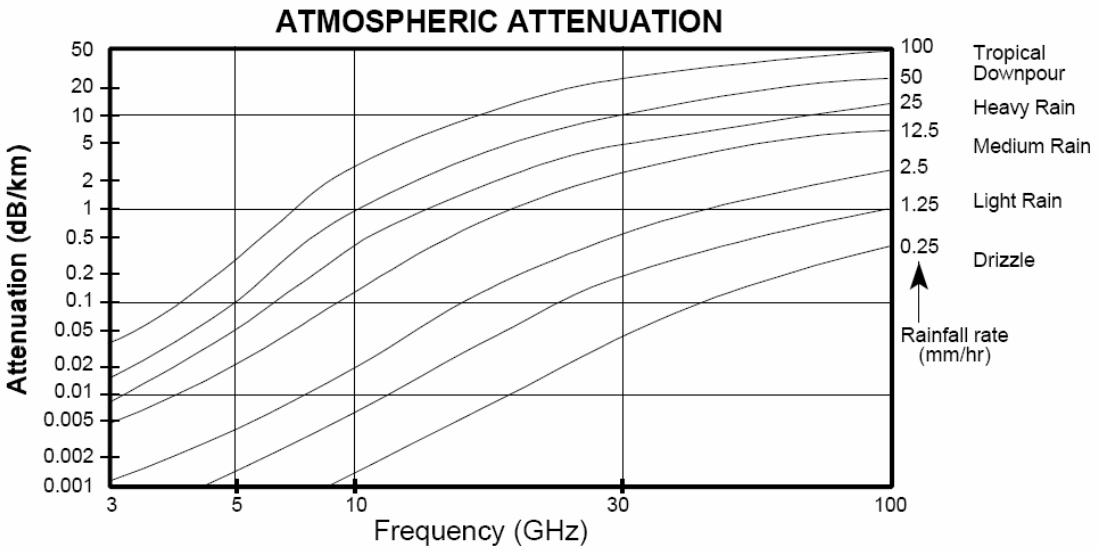

Figure 1. 2 Atmospheric attenuation due to rainfull rate.

The 60 GHz band can achieve a net data-rate of multiple gigabits per second over short distances [22]. Examples of applications are wireless gigabit Ethernet [23], and short-range wireless multimedia applications [24]. Furthermore in Japan, a wireless home link which can transmit broadcast TV signals from TV antennas to a TV set while also distributing them to other devices in the household has been presented in [25], while [24] proposes a scenario using dual-band operation (i.e. a 60 GHz system in combination with a 5 GHz WLAN) for the office and home environment.

The tendency in recent decades has been to make more cost-effective systems while preserving the same performance as older systems. Here, improving the cost-effectiveness corresponds to minimizing the substrate surface, and thus to integrating the entire millimeter meter wave system in a package (SiP) or even on a chip (SoC).

Some 60 GHz band highly-integrated transmitter- and receiver-chipsets for data transmission have been recently reported in [26-33,37-40]. They include front-end circuits such as power amplifiers (PA), low noise amplifiers (LNA), frequency multipliers, mixer, filters, voltage controlled oscillators (VCO), phase locked loops (PLL) and switchers. Integrated transceivers using CMOS technology have been described in [35-40].

A complete SoC should take fully-integrated antennas into consideraton as well as the transceiver. Early work in this direction has begun to appear, for instance [41]

presented a transistor amplifier integrated with a very simple 60 GHz microstrip array antenna with a simple etched pattern on an alumina substrate. References [34-36,42,43] present packaging of 60 GHz chip with an antenna. Reference [43] gives a configuration of SIP with the antenna using LTCC technology. More recently, [44,45] presented low-directivity integrated antennas on CMOS SOI (Silicon On Insulator) substrates, while [46] presented an integrated folded dipole on high-resistivity silicon.

The size of such antennas is frequently smaller or of the order of 1 mm in dimension, and therefore is much smaller than modern probing devices. Thus, their radiation performance is difficult to characterize as they are perturbed by their testing environment such as RF probes, connecting bond wires and transmission lines. So in this chapter, firstly we present some existing test benches which were developed recently. Secondly we present some existing or preexisting techniques to characterize integrated antennas at millimeter wave frequencies. These techniques include the probe-fed technique, waveguide-fed technique, transmission-line-fed technique, optical-link-fed technique and the VCO-fed technique.

II Test benches

In the classical gain pattern characterization setup, the two antennas (i.e. the AUT and the measuring antenna which is usually a horn antenna) should be placed in the far-field range at same altitude above the ground. The horn antenna is fixed while the AUT rotates around its own positioner's axis. The transmission energy is recorded by the apparatus at each position, and the Friis transmission equation is applied to get the radiation pattern in one plane. Subsequently, the AUT is rotated through 90° and the polarization of the horn antenna is changed to get all the co- and cross-polarization measurements of the E- and H- fields. Figure 1. 3 show the classical setup with the measuring antenna (horn antenna) on the left and the AUT on the right. The AUT is fixed on a motorized axis. This setup can be used up to several hundred GHz if the AUT is highly directive, but will not usually be suitable for other AUTs.

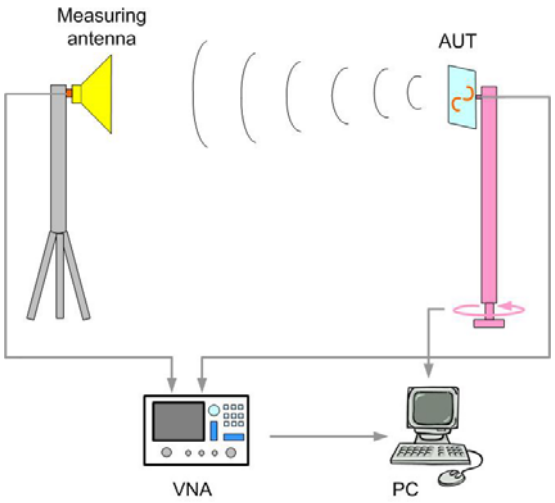

Figure 1. 3 Classical radiation pattern characterization setup.

At millimeter-wave frequencies and for millimeter-size antennas, the classical test bench is no-longer applicable. Instead, the radiation pattern is conventionally characterized with the help of a probe system. It is impractical to rotate the AUT with the probe system, thus the AUT is fixed and the measuring antenna rotates about two perpendicular horizontal axes with the AUT at the centre.

Several 3D radiation pattern measurement benches have been previously developed [47-57]. In [47,49,51,53], instead of being placed on a conventional probe station chuck, the AUT is placed on a extended thin dielectric sample holder. This minimizes the reflection and obstruction of the radiation pattern (Figure 1. 4 b). Rather than using a dielectric sample holder, [48] places an on-wafer AUT on top of a cavity filled with cavity resonance absorber (Figure 1. 5) which is suited for a cavity-backed superstrate antenna. Another way to minimize such reflection and obstruction is described in [47], which places the positioner and the probe leveling system outside an anechoic chamber,

Another important aspect of 3D radiation pattern measurement benches is the ability to measure at different angles, [49,51,53] describe a rotating arm where the measuring antenna is fixed. These rotating arms have two rotary stages and two rotary axes which enable different AUTs with different beam propagation senses. References [49, 53] use two quarter-circle-shaped rotary stages (Figure 1. 4) while [51] uses two L-shaped rotary stages.

Normally, two polarizations (co- and cross- polarization) must be measured and the

conventional way to make these measurements is to rotate the measuring antenna manually or to insert a rotary waveguide. However [50] proposed that the horn antenna connects to a small motor by a belt. As the small motor is fixed on the rotating arm, this setup can achieve arbitrary polarizations.

Rather than having the measuring antenna rotate with the arm, [52,55,57] use a fixed curvilinear rail to guide the path of the measuring antenna. While [52] and [55] (Figure 1. 6 (a) and (b)) move the measuring antenna through a quarter-circle around the AUT, [57] is able to measure a half circle. Furthermore the setup described in [57] places the feeding probe in the upper hemi-sphere while measuring the radiation pattern in the lower hemi-sphere, thereby eliminating the influence of the feeding system (probe body) on the radiation pattern. On the other hand, the setup described in [57] is only applicable for AUTs with contacts on the backside of the antenna's ground plane, since for AUTs with other contact configurations the RF probe would alter the radiation pattern.

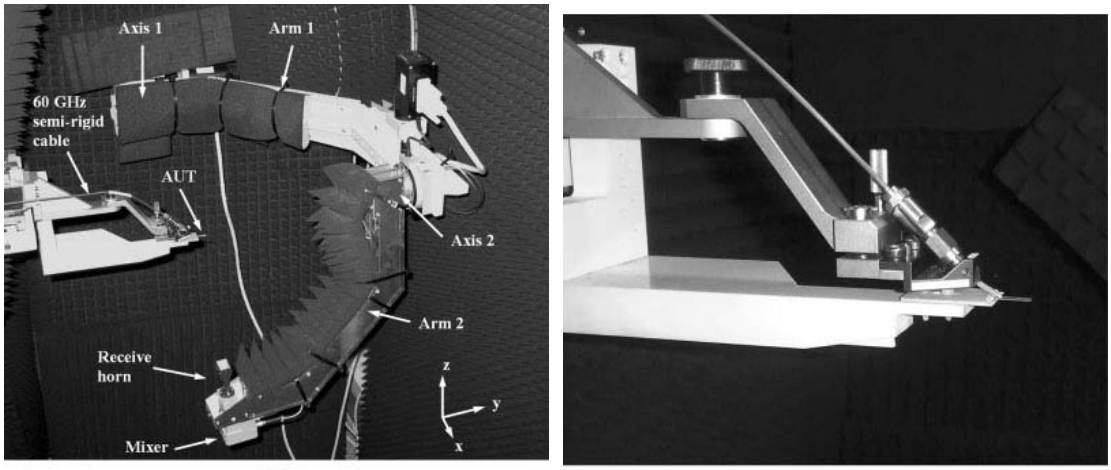

Figure 1. 4 Photos of (a) the measurement setup in LEAT; (b) close up of the probe and AUT holders [49].

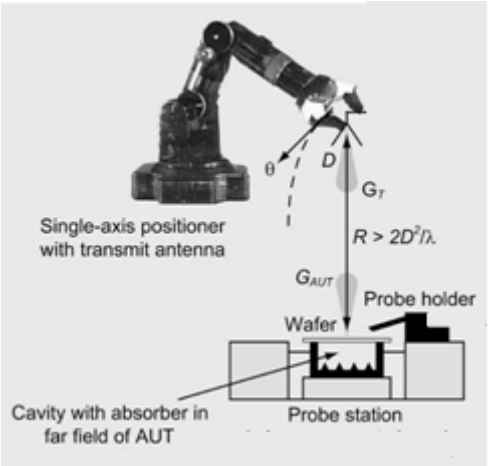

Figure 1. 5 Schematic of the setup for measurement of radiation pattern in the University of Michigan [48].

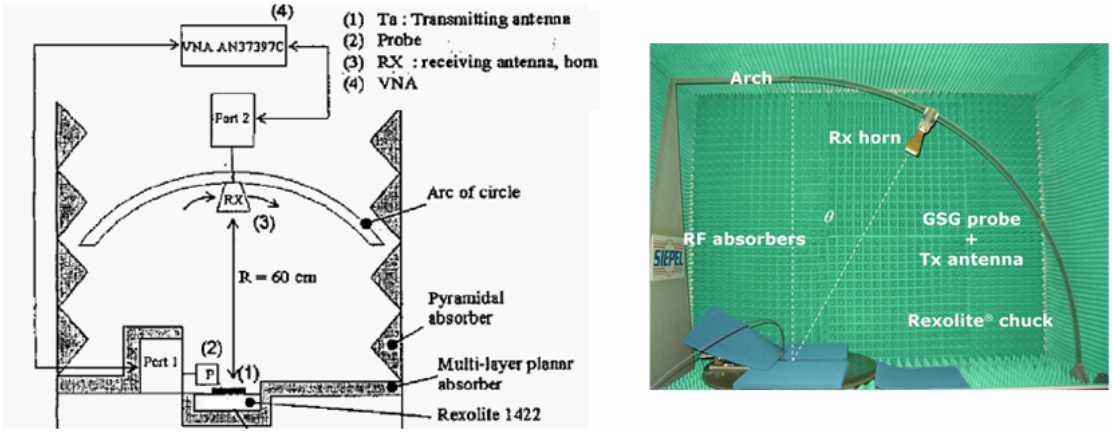

Figure 1. 6 (a) Schematic of the test bench with a quarter-circle above the AUT [52]; (b) Photo of a test bench with a quarter-circle of curvilinear rail above and to the side of the AUT [55].

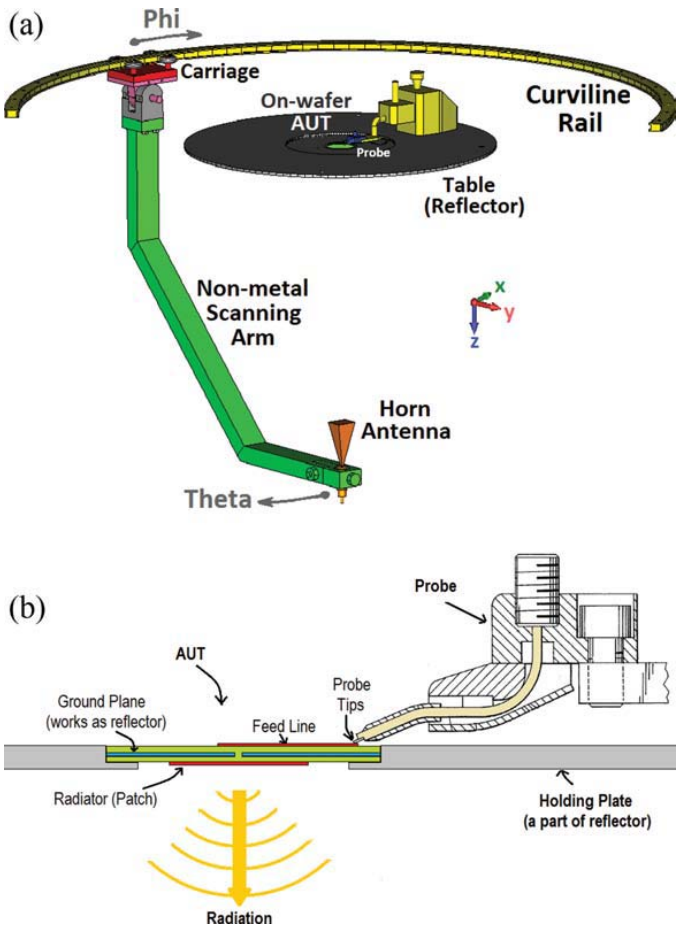

Figure 1. 7 On-probe antenna measurement setup with backside probing technique. (a) Main parts of the proposed antenna measurement setup; (b) details on feeding from backside for aperture coupled antennas [57].

All the test benches presented above can be used for radiation pattern characterization with a standard-probe-fed technique, but they all have significant limitations. The curvilinear rails in [52,55] do not cover the whole range of measuring angles. All the techniques described in [47-56] fail to address the influence of the probe on the radiation pattern, and although the method in [57] manages to prevent this influence, this method is not applicable to most on-chip integrated antennas, which have the radiating element and the contact on the same metal layers. Finally, none of the above authors discuss the precision of the relative position of the probe and AUT although this is important because the radiation pattern can exhibit acute spatial variations.

In conclusion, it remains to design a test bench which covers the entire upper hemisphere, ensures precise relative positioning of the AUT and measuring antenna, is (semi-)automatic and minimizes the influence of the probe on the radiation pattern. Perhaps this can be achieved by a *non-standard probe feeding technique*? Indeed we

discuss a suitable non-standard probe feeding technique in Chapter III.

III Probe-fed technique

The probe-fed technique is the conventional way to characterize radiation patterns for millimeter-wave frequencies. As reviewed in the previous section, all the test benches from references [47-57] used the probe-fed technique. One of the main problems with this technique is that millimeter-wave antennas are usually much smaller than modern probes (1 mm versus 2-3 cm), so that if we put a probe about 1 cm away from the AUT (as in [47-56]), there is a severe limitation on the angular sector over which measurements can be taken.

Furthermore the probe is typically metallic, which adds diffraction effects to the radiation pattern. To counteract this, a microwave absorbing material can be placed on the probe station's metal surfaces. However, in view of the size of a probe, the absorber can induce even more masking effect on the radiation pattern – see Figure 1. 8. Reference [57] eliminates reflections / diffractions by placing the probe under the ground plane of the AUT, hence improving the angular sector available for measurement. However, this configuration is not applicable to most on-chip integrated antennas, which have the radiating element and the contact on the same metal layers (Figure 1. 7 b).

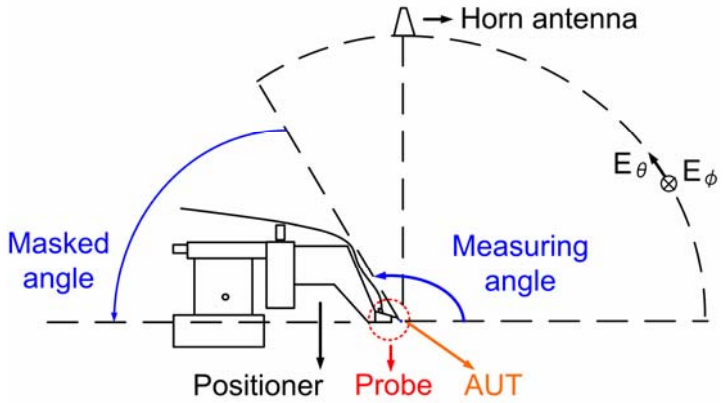

Figure 1. 8 Schematic of a test bench using probe-fed technique.

To improve on the previously proposed methods, we present two customized probes in Chapter III, that simultaneously maximize the angular range available for measurement while remaining compatible with most on-chip integrated antennas.

IV Transmission-line-fed technique

One way to improve the performance of previously-proposed measurement techniques [47-56] is to supply the AUT with a long feed line to extend the distance between the probe and the AUT. The feed line can be integrated on the same substrate as the AUT, as in [49, 51, 59], or it can be connected to the AUT via bond wires, as in [58]. One advantage of using bond wires is that multiple AUTs can be connected to the same measuring apparatus. However, bond wires are difficult to handle at such high frequencies, because it is difficult to maintain a good impedance matching and the wires may trigger parasitic radiation if they are too long. A V-connector is generally used as an interface between the feed line and the instrumentation [49, 58], but the transition between this connector and the feed line has to be carefully controlled to guarantee a good impedance matching, and the connector can also mask a part of the desired scanning zone.

Introducing a transmission line between a probe and the AUT or between a V-connector and the AUT reduces parasitic scattering from the probe or V-connector. However, the masking effect remains unsolved, which is a major limitation when characterizing a low-directivity antenna.

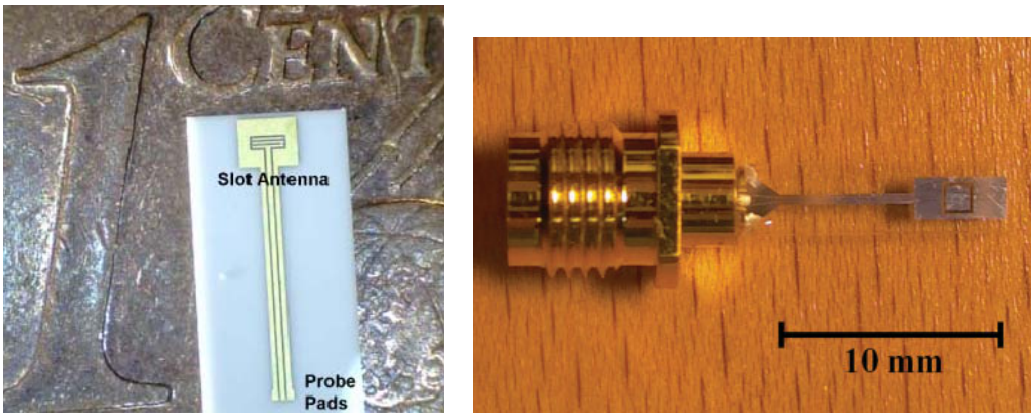

(a) (b)

Figure 1. 9 (a) Slot antenna with feeding line and GSG pads in [51]; (b) planar antenna with feeding line and connector in [49].

To improve on the previously proposed methods, we use a transmission line made of a flexible substrate coupled with a flip-chip connection in Chapter IV, which simultaneously maximizes the range of available measurement angles and (attempts to) minimize parasitic radiation.

V Waveguide-fed technique

Another way to improve the standard probe-fed technique reviewed in Section II is to use a standard waveguide to feed the antenna. In [59-62], the authors describe feeding patch antennas with specially-designed waveguides located under the AUTs. The electromagnetic energy couples to the AUT from the waveguide via a slot (Figure 1. 10). One disadvantage of this technique is that it is complicated to design a waveguide on the backside of an integrated AUT because a transition is needed between the feed line and the waveguide.

Some work on waveguide-to-microstrip transitions appears in [63-65]. Among these references [65] uses low-temperature co-fired (LTCC) technology at millimeter-wave frequencies. The final module consists of a 2×2 antenna array, a microstrip line and a substrate integrated waveguide (SIW)-microstrip transition. It is mounted on and fed by a commercial waveguide flange WR 15 as shown in Figure 1. 13 (a) and (b).

While [65] proves the feasibility of a standard waveguide-fed technique, this technique is not very economical as it requires the complete design of a transition to feed the AUT from the rear (i.e. under the antenna) for every new AUT and every new technology (CMOS, LTCC, HTCC, GaAs, SiGe…).

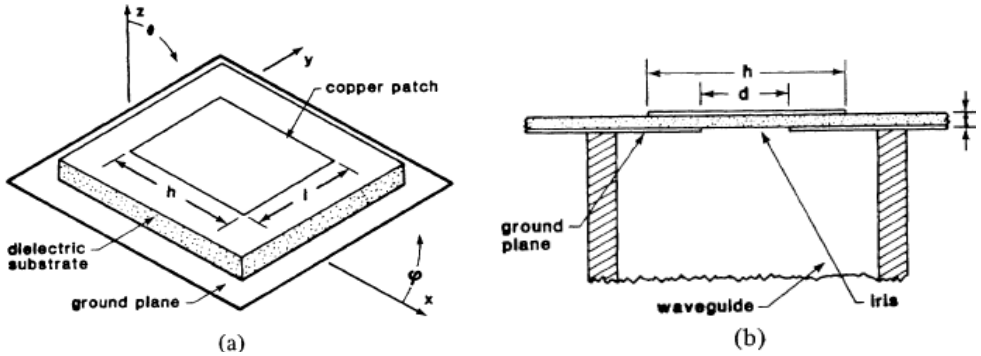

Figure 1. 10 (a) Rectangular microstrip patch antenna; (b) cut-away view; from [61].

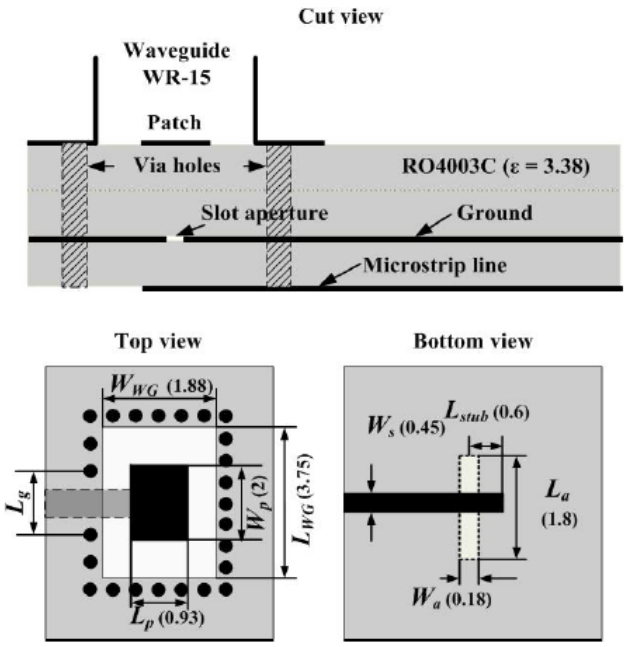

Figure 1. 11 General view of the waveguide to microstrip line transition [65].

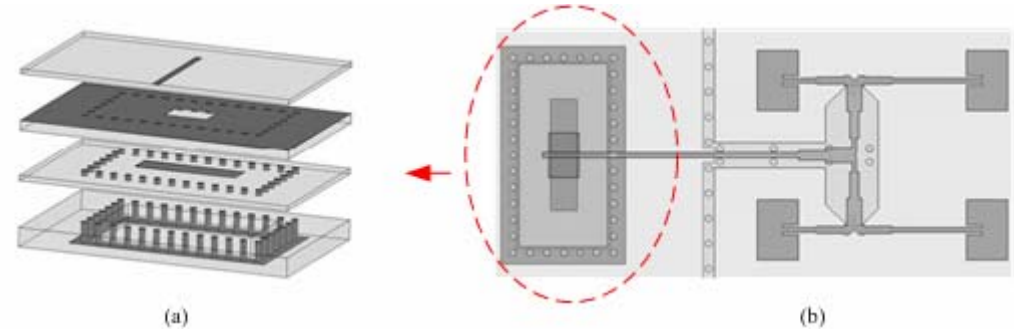

Figure 1. 12 (a) Waveguide-to-microstrip transition layer stack; (b) top view of the 60 GHz patch antenna array including the waveguide transition [65].

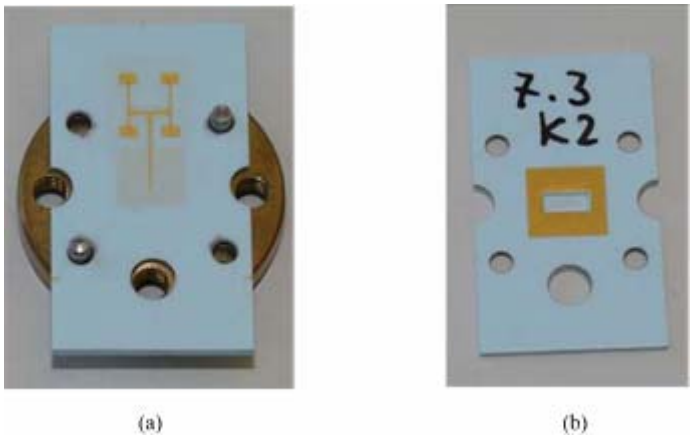

Figure 1. 13 Photograph of the LTCC module (a) The top side of the antenna array is seen mounted on a waveguide flange; (b) the bottom side with the waveguide contacting metal ring around the air cavity [65].

VI Optically-fed technique

Another way to improve the standard probe-fed technique reviewed in Section II is an optically-fed technique. There are two main advantages of using an optical link rather than a coaxial cable to feed the AUT. First, it is possible to minimize masking effects as the feeding source can be placed far from the AUT. The transmission loss in optical fiber is negligible compared to a coaxial cable, so with the help of a long optical fiber, *all* the apparatus can be easily placed several meters away from the AUT (outside of the anechoic chamber) without any substantial loss. Second, optical fiber is not metallic thus it does not cause the any parasitic diffraction and reflection.

Some fibre-optical millimeter-wave transmission links use two horn antennas as their transmitting and measuring antennas. Thus a conventional photo-detector (PD) is used in [66-68]. However for integrated antennas, the big difference in scale between the PD and the AUT make it currently impractical to use a conventional PD for measurement. Rather, configurations involving the integration of a PD with an AUT are preferred [69-73].

Several recent works have investigated optically-fed structure with the use of different PD, such as pin PDs, uni-travelling-carrier photo-detector (UTC-PDs) and avalanche photo-detectors (APDs). This work investigated: planar antennas fed by a pin PD at 20 GHz [69] and at 25 GHz [70]; References [71-73, 76] are all fed by a UTC-PD and the AUTs in these works are: a 60 GHz slot antenna in [76]; a 120 GHz integrated slot antenna [71, 72]; and a 280 GHz integrated TEM horn [73]. Only in [70], the optical fibre is integrated with the AUT's substrate and arrives in the active area of the PD. The PDs described in [71-73,76] do not integrate the optical fibre, thus during the characterization of the AUT, a *lensed* fibre (i.e. with lenses between the end of the fibre and the PD) is used to point carefully to the active area of the PD (Figure 1. 17).

Figure 1. 14 presents a 20 GHz planar photonic band-gap dipole antenna fed by an integrated photo-detector (PIN photodiode) through a MMIC amplifier [69]. The dipole slot antenna is etched on a RT Duroid substrate.and the photo-detector is grown on a semi-insulating GaAs substrate. Figure 1. 15 shows the feeding chain of the measurement setup. A Mach-Zehnder-Modulator (MZM) modulates the optical carrier with an RF signal (f_m=20 GHz) and the modulated signal is amplified by an Erbium-doped fiber amplifier (EDFA) and then divided by a power divider (D). The divided signal is coupled with the photo-detector which feeds the slot antenna.

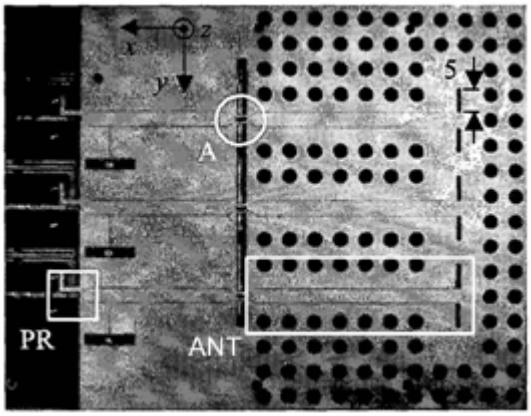

Figure 1. 14 PBG antenna (ANT) with integrated photoreceiver (PR) and MMIC amplifier (A) [69].

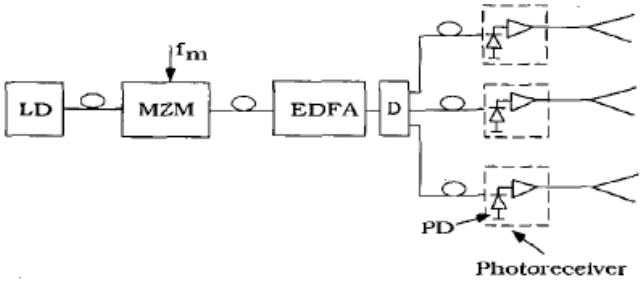

Figure 1. 15 Measurement setup [69].

Figure 1. 16 shows a 120 GHz integrated photonic transmitter [72]. It consists of a CPW-fed slot antenna, a uni-traveling-carrier photodiode (UTC-PD) [74,75] and a Si lens. The slot antenna is fabricated on a high-resistivity Si substrate and the UTC-PD is flip-chip-bonded to the CPW pads. The photo-detector receives a 120 GHz sinusoidal optical wave (1.55 μm), then it generates a millimeter-meter wave which is transmitted to the slot antenna. Given the presence of the Si lens, the electric fields mainly radiate on the substrate side. The radiation power of the AUT is measured by a horn antenna through two Teflon lenses. The experimental setup for radiation power measurement shown in Figure 1. 17. The output power of the transmitter exceeds 100μw at 120 GHz.

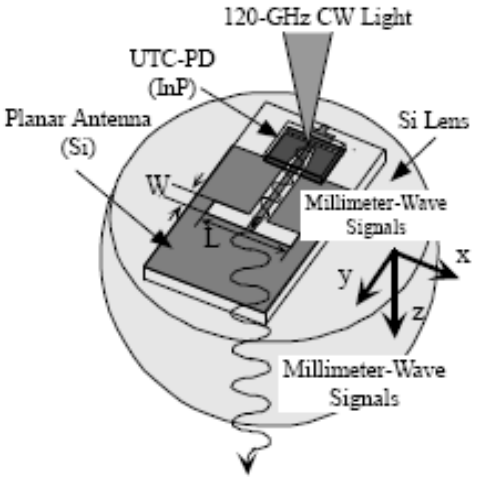

Figure 1. 16 Diagram of the 120-GHz integrated photonic transmitter [72].

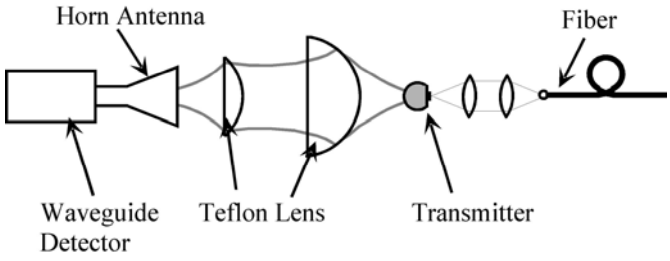

Figure 1. 17 Measurement setup of the transmitter [72].

Reference [76] demonstrates the feasibility of the integration of a photo-detector with an AUT at 60 GHz. However all the above references which operate at a frequency superior to 25 GHz have used lenses between the fibre and the PD. There are two consequences of this design: a risk of parasitic radiation originating from the support of these lenses; and a potential difficulty in ensuring the same coupling between the optical signal and the PD each time that the apparatus is set up. It is surprising that no-one has attempted to implement a lens-free characterization technique (i.e. with an optical fibre directly integrated with a photo-detector without lenses) for higher frequencies.

In conclusion, the integration of optical fibres with PDs will be necessary for successful implementation of the optically-fed technique for most AUTs (e.g. other than very simple cases such as slot antennas described in [76]) at 60 GHz or above.

VII VCO-fed technique

Integrated antennas may also be fed using a voltage-controlled oscillator (VCO)

[78-87]. References [78-80] present antennas integrated with a VCO for the X-band (8-12GHz), [81-83] for the K-band (18-26 GHz), [77,84-86] for the V-band (50-75GHz) and [87,88] for the sub-millimeter-wave band (300 GHz-1THz).

For RF signals, there are three ways to combine a VCO with an integrated antenna: one is to have the VCO and the antenna integrated on the same substrate, e.g. at 21 GHz in [81] (Figure 1. 18 (a)) and at 60 GHz in [77] (Figure 1. 20); a second way is to use a flip-chip connection, although such flip-chip connections involve the use of an upside-down VCO; and a third way is to use bond wires e.g. [84] at 60 GHz (Figure 1. 19), but we do not believe that bond wires are a good solution at millimeter-wave frequencies.

These three methods may also be used to supply a VCO which is feeding an integrated antenna, bearing in mind that a VCO is a tunable circuit whose output frequency varies as a function of the input voltage and that a VCO itself needs to connect to a supply voltage. So firstly, we might use a standard probe system [89], but as described previously, this would cause masking effects, so it is not a good solution (Figure 1. 18 (b)). Secondly we might use bond wires and try to keep enough space between the AUT and the bond wires to avoid parasitic coupling and diffraction (Figure 1. 18 (a)). Finally, one might also use a flip chip connection.

The main advantage of using a VCO to feed an integrated antenna, relative to using a standard probe or a transmission line, as described in the previous sections, is that a VCO can be small compared to a standard probe or compared to the connector to a transmission line, and thus using a VCO can minimize reflections and parasitic radiation.

In conclusion, references [81, 77] prove the feasibility of the VCO-fed technique at 21 and 60 GHz. However this technique (similarly to the waveguide-fed technique) is not particularly economical as it is necessary to design an integrated VCO antenna circuit for each AUT. A VCO-fed technique with a flip-chip connection appears promising, but has not been previously investigated, and may be of interest for future work.

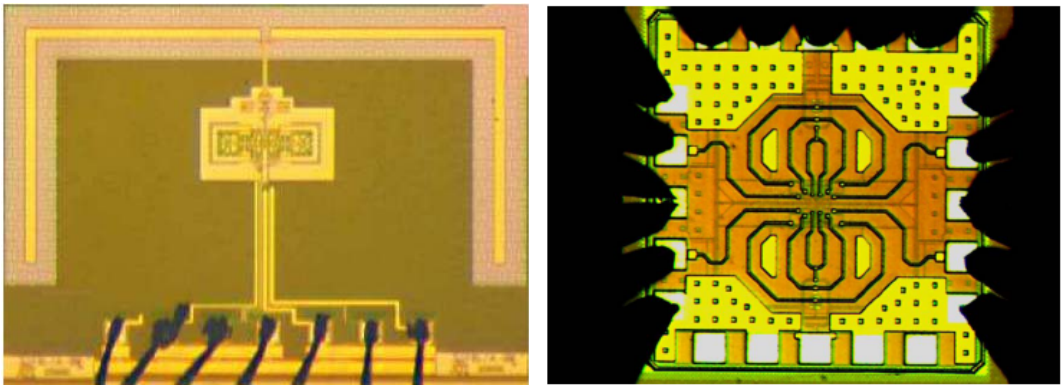

(a) (b)

Figure 1. 18 Photo of (a) the 21 GHz chip (dipole antenna and VCO) under measurement [81] (1.5 ×2.4 mm^2) (b) the 60 GHz QVCO chip under measurement (0.7×0.65 mm^2) [89].

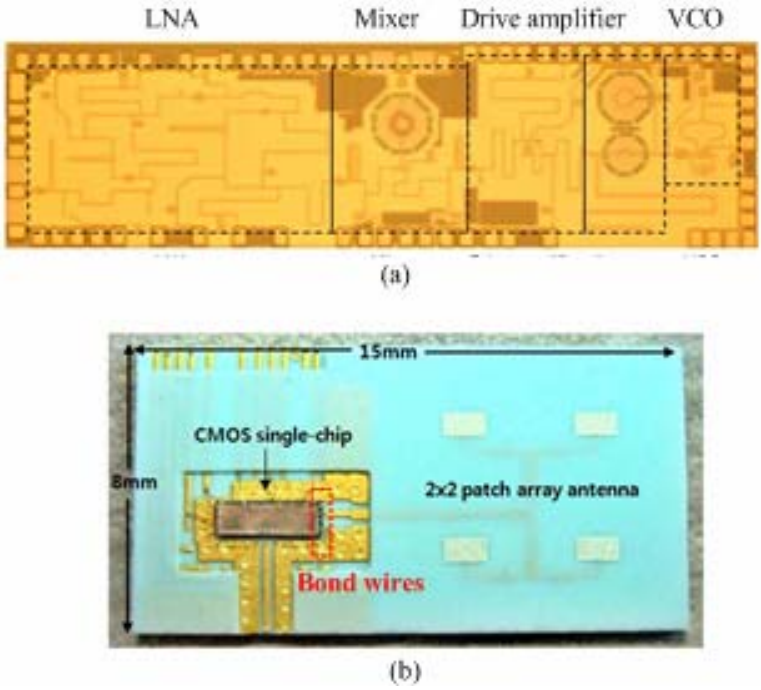

Figure 1. 19 Photos of (a) a receiver chip (2.67×0.75 mm^2) (b) 60 GHz LTCC SiP module [84].

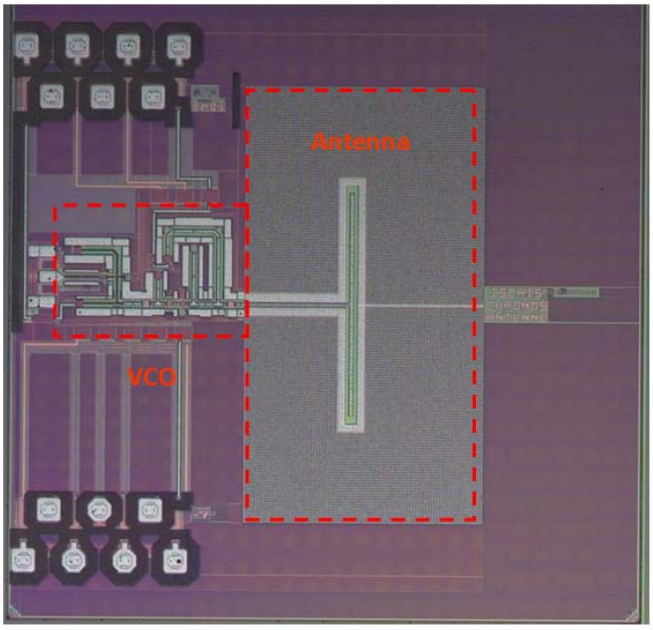

Figure 1. 20 Photo of the 60 GHz impulse transmitter with integrated antenna [77].

VIII Conclusion

In this chapter, we presented several existing test benches and several feeding techniques for millimeter-wave frequencies, including the probe-fed technique, transmission-line-fed technique, waveguide-fed technique, optical-link-fed technique and the VCO-fed technique.

The angular-range limitation and parasitic reflection from the apparatus (a standard probe, a V-connector and wirebonding at 60 GHz band) are the two main problems with the standard-probe-fed and transmission-line-fed technique.

The standard-waveguide-fed, optically-fed and the VCO-fed techniques all concern the integration of the feeding source with the AUT. They could be implemented with the same or different technology as the AUT, but it may be challenging to ensure a good impedance match, for instance, using wire bonding in the 60 GHz band is not a good solution. It is possible to use several layers of LTCC to form a transition from a substrate-integrated waveguide to a microstrip line [65], however no-one has investigated this approach with other integrated technologies. VCOs are quite mature components for multiple technologies, they have been successfully integrated with antennas using the same technology, although this can be expensive, and it may be

interesting to attempt to connect a VCO to an AUT with a flip-chip connection. Finally, the optically-fed technique is quite promising however if the optical fibre is not integrated, but rather supplies a photodetector via lenses, it becomes necessary to build a positioning system which may also cause masking effects and parasitic reflection.

Thus, this thesis (as described in the overview of General Introduction) focuses on the standard-probe-fed and transmission-line-fed techniques and discusses improvements of these two techniques in Chapters III and IV, since these techniques are easy to reproduce and are suitable for most integrated on-chip antennas.

References:

[1] R. Wielebinski, "Microwaves -- The New Horizons of Radio Astronomy," *Microwave Conference, 1987. 17th European*, pp. 19-24.

[2] J.W.M. Baars and H.J. Karcher, "Design features of the Large Millimeter Telescope (LMT)," *Antennas and Propagation Society International Symposium, 1999. IEEE*, pp. 1544-1547 vol.1543.

[3] J. Davis and J. Cogdell, "Astronomical refraction at millimeter wavelengths," *Antennas and Propagation, IEEE Transactions*, vol. 18, no. 4, 1970, pp. 490-493.

[4] A.Karpov, "Optimizing receivers for ground based mm-wave radio telescopes," proceeding of the 2th ESA workshop on millimeter wave thchnology and applications. IRAM technical report 250/98, 1998.

[5] J.B. Mead, A.L. Pazmany, S.M. Sekelsky and R.E. McIntosh, "Millimeter-wave radars for remotely sensing clouds and precipitation," *Proceedings of the IEEE*, vol. 82, no. 12, 1994, pp. 1891-1906.

[6] R.P. Bambha, J.R. Carswell, J.B. Mead and R.E. McIntosh, "A compact millimeter wave radar for airborne studies of clouds and precipitation," *Geoscience and Remote Sensing Symposium Proceedings, 1998. IGARSS '98. 1998 IEEE International*, pp. 443-445 vol.441.

[7] J.R. Wang and P. Racette, "Airborne millimeter-wave radiometric observations of cirrus clouds," *Geoscience and Remote Sensing, 1997. IGARSS '97. Remote Sensing - A Scientific Vision for Sustainable Development., 1997 IEEE International*, pp. 1737-1739 vol.1734.

[8] T. Toshiaki, Y. Jun, A. Hideji, F. Ken-ichi, Y. Shin-ichi, K. Hiroshi, A. Ken-ichi, K. Youhei, O. Yuichi, T. Tamio, N. Teruyuki, O. Hajime, F. Yasushi and S. Nobuo, "Observations of cloud properties using the millimeter- wave FM-CW radar of Chiba Univ," *Microwave Conference, 2006. APMC 2006. Asia-Pacific*, pp. 560-563.

[9] T. Takano, Y. Nakanishi, H. Abe, J. Yamaguchi, S.I. Yokote, K.I. Futaba, Y. Kawamura, H. Kumagai, Y. Ohno, T. Takamura and T. Nakajima, "Performance of a Developed Low-Power and High-Sensitivity Cloud Profiling Millimeter-wave Radar : FALCON-I," *Microwave Conference, 2007. APMC 2007. Asia-Pacific*, pp. 1-4.

[10] J.H. Wehling, "Multifunction millimeter-wave systems for armored vehicle application," *Microwave Theory and Techniques, IEEE Transactions*, vol. 53, no. 3, 2005, pp. 1021-1025.

[11] D.N. McQuiddy, Jr., "High volume applications for GaAs microwave and millimeter-wave ICs in

military systems," *Gallium Arsenide Integrated Circuit (GaAs IC) Symposium, 1989. Technical Digest 1989., 11th Annual*, pp. 3-6.

[12] V.I. Antyufeev, V.N. Bykov, A.M. Grichaniuk, V.A. Krayucshkin and S.A. Shilo, "Radiometric observability estimation of military equipment samples in a millimeter-wave band," *Physics and Engineering of Microwaves, Millimeter, and Submillimeter Waves, 2004. MSMW 04. The Fifth International Kharkov Symposium on*, pp. 196-198 Vol.191.

[13] J. Altmannm, "Millimetre Waves, Lasers, Acoustics for Non-Lethal Weapons? Physics Analyses and Inferences," Technical University of Dortmund, 2008.

[14] M. Schneider, "Automotive Radar – Status and Trends," Proc.German Microwave Conference GeMiC, Ulm, Germany, pp. 144-147.

[15] I. Gresham, N. Jain, T. Budka, A. Alexanian, N. Kinayman, B. Ziegner, S. Brown and P. Staecker, "A compact manufacturable 76-77-GHz radar module for commercial ACC applications," *Microwave Theory and Techniques, IEEE Transactions*, vol. 49, no. 1, 2001, pp. 44-58.

[16] D.M. Grimes, and T.O. Jones, "Automotive radar: A brief review," *Proceedings of the IEEE*, vol. 62, no. 6, 1974, pp. 804-822.

[17] Australian communications Authority, "A review of automotive *radar systems* - devices and regulatory frameworks," 2001.

[18] K-C. Huang and Z. Wang, "Millimeter Wave Communication Systems," John Wiley & Sons, 2011.

[19] I. Chee-Hong Lai amd M. Fujishima, "Design and Modeling of Millimeter-Wave CMOS Circuits for Wireless Transceivers," Springer, 2008.

[20] D.X. Liu, U. Pfeiffer and J. Grzyb, "Advanced Millimeter-Wave Technologies: Antennas, Packaging and Circuits", John Wiley & Sons, 2009.

[21] D. Wang and N. Cahoon, "60 GHz high speed wireless link - technology and design challenges," *Solid-State and Integrated-Circuit Technology, 2008. ICSICT 2008. 9th International Conference.* pp. 1343-1347.

[22] P. Smulders, Y. Haibing and I. Akkermans, "On the Design of Low-Cost 60-GHz Radios for Multigigabit-per-Second Transmission over Short Distances [Topics in Radio Communications]," Communications Magazine, IEEE, 45 (2007), 44-51.

[23] K. Ohata, K. Maruhashi, M. Ito, S. Kishimoto, K. Ikuina, T. Hashiguchi, K. Ikeda and N. Takahashi, "1.25 Gbps wireless Gigabit ethernet link at 60 GHz-band," Radio Frequency Integrated Circuits (RFIC) Symposium, 2003 IEEE, Philadelphia, 2003.

[24] P. Smulders, "Exploiting the 60 GHz band for local wireless multimedia access: prospects and future directions," Communications Magazine, IEEE, 40 (2002), 140-147.

[25] K. Hamaguchi, Y. Shoji, H. Ogawa, H. Sato, K. Tokuda, Y. Hirachi, T. Iwasaki, A. Akeyama, K. Ueki and T. Kizawa, "A wireless video home-link using 60 GHz band: Concept and performance of the developed system," *Proc. 30th Eur. Microw. Conf.*, Paris, France, Oct. 2–6, 2000, vol. 1, pp. 293–296.

[26] M. Siddiqui, M. Quijije, A. Lawrence, B. Pitman, R. Katz, P. Tran, A. Chau, D. Davison, S. Din, R. Lai and D. Streit, "GaAs components for 60 GHz wireless communication applications," *GaAs Mantech Conf. Tech. Dig.*, San Diego, CA, Apr. 11, 2002, pp. 243–246.

[27] K. Fujii, M. Adamski, P. Bianco, D. Gunyan, J. Hall, R. Kishimura, C. Lesko, M. Schefer, S. Hessel, H. Morkner and A. Niedzwiecki, "A 60 GHz MMIC chipset for 1-Gbit/s wireless links," *IEEE MTT-S Int. Microw. Symp. Dig.*, Seattle, WA, Jun. 2–7, 2002, vol. 3, pp. 1725–1728.

[28] O. Vaudescal, B. Lefebvre, V. Lehoué and P. Quentin, "A highly integrated MMIC chipset for 60

GHz broadband wireless applications," *IEEE MTT-S Int. Microw. Symp. Dig.*, Seattle, WA, Jun. 2–7, 2002, vol. 3, pp. 1729–1732.

[29] Y. Mimino, K. Nakamura, Y. Hasegawa, Y. Aoki, S. Kuroda and T. Tokumitsu, "A 60 GHz millimeter-wave MMIC chipset for broadband wireless access system front-end," *IEEE MTT-S Int. Microw. Symp. Dig.*, Seattle, WA, Jun. 2–7, 2002, vol. 3, pp. 1721–1724.

[30] H. Zirath, T. Masuda, R. Kozhuharov and M. Ferndahl, "Development of 60 GHz front-end circuits for a high-data-rate communication system," *IEEE J. Solid-State Circuits*, vol. 39, no. 10, pp. 1640–1649, Oct. 2004.

[31] B. A. Floyd, S. K. Reynolds, U. R. Pfeiffer, T. Zwick, T. Beukema, and B. Gaucher, "SiGe bipolar transceiver circuits operating at 60 GHz," *IEEE J. Solid-State Circuits*, vol. 40, no. 1, pp. 156–167, Jan. 2005.

[32] S. E. Gunnarsson, C. Kärnfelt, H. Zirath, R. Kozhuharov, D. Kuylenstierna, A. Alping and C. Fager, "Highly integrated 60 GHz transmitter and receiver MMICs in a GaAs pHEMT technology," *IEEE J. Solid-State Circuits*, vol. 40, no. 11, pp. 2174–2186, Nov. 2005.

[33] J. Mizoe, S. Amano, T. Kuwabara, T. Kaneko, K. Wada, A. Kato, K. Sato and M. Fujise, "Minature 60 GHz transmitter/receiver modules on AlN multi-layer high temperature co-fired ceramic," *IEEE MTT-S Int. Microw. Symp. Dig.*, Anaheim, CA, Jun. 13–19, 1999, vol. 2, pp. 475–478.

[34] J.M. Gilbert, C.H. Doan, S. Emami and C.B. Shung, "A 4-Gbps Uncompressed Wireless HD A/V Transceiver Chipset," *Micro, IEEE*, vol. 28, no. 2, 2008, pp. 56-64.

[35] S.K. Reynolds, B.A. Floyd, U.R. Pfeiffer, T. Beukema, J. Grzyb, C. Haymes, B. Gaucher and M. Soyuer, "A Silicon 60-GHz Receiver and Transmitter Chipset for Broadband Communications," *Solid-State Circuits, IEEE Journal,* vol. 41, no. 12, 2006, pp. 2820-2831.

[36] S. Pinel, S. Sarkar, P. Sen, B. Perumana, D. Yeh, D. Dawn and J. Laskar, "A 90nm CMOS 60GHz Radio," *Solid-State Circuits Conference, 2008. ISSCC 2008. Digest of Technical Papers. IEEE International*, pp. 130-601.

[37] C. H. Doan, S. Emami, D. A. Sobel, A. M. Niknejad and R. W. Brodersen, "Design considerations for 60 GHz CMOS radios," *IEEE Commun. Mag.*, pp. 132–140, Dec. 2004.

[38] B. Razavi, "A 60-GHz CMOS receiver front-end," *Solid-State Circuits, IEEE Journal*, vol. 41, no. 1, 2006, pp. 17-22.

[39] C. Marcu, D. Chowdhury, C. Thakkar, K. Ling-Kai, M. Tabesh, P. Jung-Dong, W. Yanjie, B. Afshar, A. Gupta, A. Arbabian, S. Gambini, R. Zamani, A.M. Niknejad and E. Alon, "A 90nm CMOS low-power 60GHz transceiver with integrated baseband circuitry," *Solid-State Circuits Conference - Digest of Technical Papers, 2009. ISSCC 2009. IEEE International*, pp. 314-315.

[40] M. Tanomura, Y. Hamada, S. Kishimoto, M. Ito, N. Orihashi, K. Maruhashi and H. Shimawaki, "TX and RX Front-Ends for 60GHz Band in 90nm Standard Bulk CMOS," *Solid-State Circuits Conference, 2008. ISSCC 2008. Digest of Technical Papers. IEEE International*, pp. 558-635.

[41] C. Karnfelt, P. Hallbjorner, H. Zirath and A. Alping, "High gain active microstrip antenna for 60-GHz WLAN/WPAN applications," *Microwave Theory and Techniques, IEEE Transactions*, vol. 54, no. 6, 2006, pp. 2593-2603.

[42] Y.P. Zhang and D. Liu, "Antenna-on-chip and antenna-in-package solutions to highly integrated millimeter-wave devices for wireless communications," *Antennas and Propagation, IEEE Transactions*, vol. 57, no. 10, 2009, pp. 2830-2841.

[43] T. Seki, K. Nishikawa, I. Toyoda, and S. Kubota, "Microstrip Array Antenna with Parasitic Elements Alternately Arranged Over Two Layers of LTCC Substrate for Millimeter Wave

Applications," *Radio and Wireless Symposium, 2007 IEEE*, pp. 149-152.
[44] M. Barakat, C. Delaveaud and F. Ndagijimana, "Performance of a 0.13µm SOI integrated 60 GHz dipole antenna," IEEE Antennas and Propagation Society International Symposium, Honolulu, HI, 2007.
[45] M. Barakat, C. Delaveaud, F. Ndagijimana, "Circularly Polarized Antenna on SOI for the 60 GHz Band," Antennas and Propagation, EuCAP 2007, Edinburgh, 2007.
[46] L. Dussopt et al., "Silicon Interposer with Integrated Antenna Array for Millimeter-Wave Short-Range Communications," submitted to IEEE MTT-S Int. Microwave Symp., 17-22 jun. 2012, Montreal, Canada.
[47] T. Zwick, C. Baks, U. Pfeiffer, D. Liu, and B. Gaucher, "Probe based MMW antenna measurement setup," IEEE Antennas and Propagation Society International Symposium, Montery CA, 2004.
[48] K. Van Caekenberghe, K. Brakora, W. Hong, K. Jumani, D. Liao, M. Rangwala, Y. Wee, X. Zhu and K. Sarabandi, "A 2–40 GHz Probe Station Based Setup for On-Wafer Antenna Measurements," Antennas and Propagation, IEEE Transactions, 56 (2008), 3241-3247.
[49] S. Ranvier, M. Kyrö, C. Icheln, C. Luxey, R. Staraj and P. Vainikainen, "Compact 3-D on-wafer radiation pattern measurement system for 60 GHz antennas," Microwave and Optical Technology Letters, 51 (2009), 319-324.
[50] R. Simons, N.G.R. Center "Novel on-wafer radiation pattern measurement technique for MEMS actuator based reconfigurable patch antennas," National Aeronautics and Space Administration, Glenn Research Center, 2003.
[51] S. Beer, G.. Adamiuk and T. Zwick, "Design and probe based measurement of 77 GHz antennas for antenna in package applications," Microwave Conference, EuMC 2009, Rome, 2009.
[52] N. Segura, S. Montusclat, C. Person, S. Tedjini and D. Gloria, "On-wafer radiation pattern measurements of integrated antennas on standard BiCMOS and glass processes for 40-80GHz applications," Microelectronic Test Structures, ICMTS 2005, Leuven, 2005.
[53] D. Titz, M. Kyro, F.B. Abdeljelil, C. Luxey, G. Jacquemod and P. Vainikainen, "Design and measurement of a dipole-antenna on a 130nm CMOS substrate for 60GHz communications," ICECom 2010, Dubrovnik, 2010.
[54] P. Bo, L. Yuan, G.E. Ponchak, J. Papapolymerou and M.M. Tentzeris, "A 60-GHz CPW-Fed High-Gain and Broadband Integrated Horn Antenna," Antennas and Propagation, IEEE Transactions, 57 (2009), 1050-1056.
[55] R. Pilard, S. Montusclat, D. Gloria, F. Le Pennec and C. Person, "Dedicated measurement setup for millimetre-wave silicon integrated antennas: BiCMOS and CMOS high resistivity SOI process characterization," Antennas and Propagation, EuCAP 2009, Berlin, 2009.
[56] J. Lanteri, L. Dussopt, R. Pilard, D. Gloria, S.D. Yamamoto, A. Cathelin and H. Hezzeddine, "60 GHz antennas in HTCC and glass technology," EuCAP2010, Barcelona, 2010.
[57] K. Mohammadpour-Aghdam, S. Brebels, A. Enayati, R. Faraji-Dana, G.A.E. Vandenbosch and W. DeRaedt, "RF probe influence study in millimeter-wave antenna pattern measurements," International Journal of RF and Microwave Computer-Aided Engineering, 21 (2011).
[58] M. Barakat, "Dispositif radiofrequence millimetrique pour objets communicants de type smart dust," Ph.D thesis, Grenoble university, Grenoble, 2008.
[59] E. Marzolf and M.h.Drissi, "Waveguide-fed planar antennas for millimeter waveband," Microwave and Optical Technology Letters, 35, (2002), 71-73.
[60] J. Hirokawa, M. Ando and N. Goto, "Waveguide-fed parallel plate slot array antenna," Antennas

and Propagation, IEEE Transactions, 40 (1992), 218-223.

[61] M. Kanda, D.C. Chang and D.H. Greenlee, "The Characteristics of Iris-Fed Millimeter-Wave Rectangular Microstrip Patch Antennas," *Electromagnetic Compatibility, IEEE Transactions*, vol. EMC-27, no. 4, 1985, pp. 212-220.

[62] K. Sudo, A. Akiyama, J. Hirokawa and M. Ando, "A millimeter-wave radial line slot antenna fed by a rectangular waveguide through a ring slot," *Antennas and Propagation Society International Symposium, 2001. IEEE*, pp. 254-257 vol.252.

[63] A. Artemenko, A. Maltsev, R. Maslennikov, A. Sevastyanov and V. Ssorin, "Design of wideband waveguide to microstrip transition for 60 GHz frequency band," *Microwave Conference (EuMC), 2011 41st European*, pp. 838-841.

[64] T.H. Yang, C.F. Chen, T.Y. Huang, C.L. Wang and R.B. Wu, "A 60GHz LTCC transition between microstrip line and substrate integrated waveguide," APMC 2005, Suchou, 2005.

[65] F. Wollenschlager, L. Alhouri, L. Xia, S. Rentsch, J. Muller, R. Stephan, and M.A. Hein, "Measurement of a 60 GHz antenna array fed by a planar waveguide-to-microstrip transition integrated in low-temperature co-fired ceramics," *Antennas and Propagation, 2009. EuCAP 2009. 3rd European Conference*, pp. 1001-1005.

[66] N. Imai, S. Banba, E. Suematsu and H. Sawada, "Millimeter-wave fiber optic technologies for subcarrier transmission systems," *Microwave Conference, 1994. 24th European*, pp. 1465-1470.

[67] T. Shao, F. Paresys, Y. Le Guennec, G. Maury, N. Corrao and B. Cabon, "Photonic generation and radio transmission of ECMA 387 signal at 60 GHz using WDM demultiplexer," *Microwave and Optical Technology Letters*, vol. 54, no. 2, 2012, pp. 275-277.

[68] D. Wake, N.G. Walker and I.C. Smith, "A fibre-fed millimetre-wave radio transmitter with zero electrical power requirement," *Microwave Conference, 1993. 23rd European*, pp. 116-118.

[69] G.A. Chakam and W. Freude, "Coplanar phased array antenna with optical feeder and photonic bandgap structure," *Microwave Photonics, 1999. MWP '99. International Topical Meeting*, pp. 1-4 suppl.

[70] M. Khodier and C. Christodoulou, "Optically driven CPW-fed slot antenna for wireless communications," *Antennas and Propagation for Wireless Communications, 2000 IEEE-APS Conference*, pp. 121-124.

[71] N. Sahri and T. Nagatsuma, "Packaged photonic probes for an on-wafer broad-band millimeter-wave network analyzer," *Photonics Technology Letters, IEEE*, vol. 12, no. 9, 2000, pp. 1225-1227.

[72] A. Hirata, N. Sahri, H. Ishii, K. Machida, S. Yagi and T. Nagatsuma, "Design and characterization of millimeter-wave antenna for integrated photonic transmitter," *Microwave Conference, 2000 Asia-Pacific*, pp. 70-73.

[73] G. Ducournau, A. Beck, D. Ducatteau, E. Peytavit, T. Akalin and J. Lampin, "Radiation pattern measurements of an integrated TEM horn antenna," *Infrared Millimeter and Terahertz Waves (IRMMW-THz), 2010 35th International Conference*, pp. 1-2.

[74] T. Ishibashi et al., "High Power Uni-Traveling-Carrier Photodiodes," MWP'99, pp 75-78, 1999.

[75] T. Nagatsuma et al., "All Optoelectronic Generation and Detection of Millimeter-Wave Signals," MWP'98, pp 5-8, 1998.

[76] K. Li, J.X. Ge, T. Matsui and M. Izutsu, "High output photodetector and CPW-fed slot antenna array for millimeter-wave fiber-radio system," *Computational Electromagnetics and Its Applications, 1999. Proceedings. (ICCEA '99) 1999 International Conference*, pp. 337-340.

[77] A. Siligaris, N. Deparis, R. Pilard, D. Gloria, C. Loyez, N. Rolland, L. Dussopt, J. Lantéri, R. Beck, P. Vincent, "A 60 GHz UWB impulse radio transmitter with integrated antenna in CMOS 65 nm SOI technology," 11th IEEE Topical Meeting on Silicon Monolithic Integrated Circuits in RF Systems, Phoenix, 17-19 January 2011.

[78] C.C. Hu, C.F. Jou, and J.J. Wu, "Two-dimensional beam-scanning linear active leaky-wave antenna array using coupled VCOs," *Microwaves, Antennas and Propagation, IEE Proceedings*, vol. 147, no. 1, 2000, pp. 68-72.

[79] K. Nien-An, H. Cheng-Chi, W. Jin-Jei and C.F. Jou, "Active aperture-coupled leaky-wave antenna," *Electronics Letters*, vol. 34, no. 23, 1998, pp. 2183-2184.

[80] F. Touati and M. Pons, "On-chip integration of dipole antenna and VCO using standard BiCMOS technology for 10 GHz applications," *Solid-State Circuits Conference, 2003. ESSCIRC '03. Proceedings of the 29th European*, pp. 493-496.

[81] M. Pons, F. Touati, and P. Senn, "Study of on-chip integrated antennas using standard silicon technology for short distance communications," *Wireless Technology, 2005. The European Conference*, pp. 253-256.

[82] C. Changhua, D. Yanping, Y. Xiuge, L. Jau-Jr, W. Hsin-Ta, A.K. Verma, L. Jenshan, F. Martin, and K.K. O, "A 24-GHz Transmitter With On-Chip Dipole Antenna in 0.13µm CMOS," *Solid-State Circuits, IEEE Journal of*, vol. 43, no. 6, 2008, pp. 1394-1402.

[83] P.K. Talukder, M. Neuner, C. Meliani, F.J. Schmuckle and W. Heinrich, "A 24 GHz Active Antenna in Flip-Chip Technology with Integrated Frontend," *Microwave Symposium Digest, 2006. IEEE MTT-S International*, pp. 1776-1779.

[84] L. Jae Jin, J. Dong Yun, E. Ki Chan, O. Inn Yeal, and P. Chul Soon, "A low power CMOS single-chip receiver and system-on-package for 60GHz mobile applications," *Radio-Frequency Integration Technology, 2009. RFIT 2009. IEEE International Symposium on*, pp. 24-27.

[85] G. Passiopoulos, S. Nam, A. Georgiou, A. Baree, I.D. Robertson and E.A. Grindrod, "V-Band MMIC Chip-Set, Design and Performance," *Microwave Conference, 1998. 28th European*, pp. 157-162.

[86] H.K. Chiou, I.S. Chen and W.C. Chen, "High gain V-band active-integrated antenna transmitter using Darlington pair VCO in 0.13µm CMOS process," *Electronics Letters*, vol. 46, no. 5, 2010, pp. 321-322.

[87] K.O. Kenneth, "Sub-millimeter wave CMOS integrated circuits and systems," *Radio-Frequency Integration Technology (RFIT), 2011 IEEE International Symposium on*, pp. 1-8.

[88] S. Eunyoung, C. Changhua, S. Dongha, D.J. Arenas, D.B. Tanner, H. Chin-Ming, and K.K. O, "A 410GHz CMOS Push-Push Oscillator with an On-Chip Patch Antenna," *Solid-State Circuits Conference, 2008. ISSCC 2008. Digest of Technical Papers. IEEE International*, pp. 472-629.

[89] A. Barghouthi, A. Krause, C. Carta, F. Ellinger, and C. Scheytt, "Design and Characterization of a V-Band Quadrature VCO Based on a Common-Collector SiGe Colpitts VCO," *Compound Semiconductor Integrated Circuit Symposium (CSICS), 2010 IEEE*, pp. 1-3.

Chapter II
Antenna under test (AUT)

I Introduction

In this chapter, we are going to present some antenna characteristics and three millimeter-wave antennas under test we used for the radiation pattern characterization: an integrated spiral antenna on CMOS SOI and an integrated folded dipole on high-resistivity silicon.

II Antenna characteristics

Several antennas' parameters definitions will be reminded in this section, these definitions will help to describe the performance of an antenna. These parameters are following items: the radiation gain, the polarization, the radiation pattern, the input impedance, the radiation efficiency, the bandwidth, the axial ratio, far field and near field regions and the Friis transmission equation [1,2].

II.I Radiation gain

Radiation gain is one of the factors describing an antenna performances. Absolute gain of an antenna in a given direction is defined as the ratio of the radiation intensity flowing in that direction to the radiation intensity that would be obtained if the power accepted by the antenna were radiated isotropically. If the direction is not specified, the direction of maximum radiation intensity is usually implied. Antenna gain is expressed in dBi.

$$G = \frac{4\pi \cdot U(\theta,\varphi)}{P_{Acc}} \tag{3.1}$$

$$U(\theta,\varphi) = \frac{1}{2}\frac{|E|^2}{\eta_0} r^2 \tag{3.2}$$

Where

$U(\theta,\varphi)$ is the radiation intensity in watts per steradian,

|*E*| is the magnitude of the E-field,

η_0 is the intrinsic impedance of free space, 377 ohms.

The total gain can be expressed in two orthogonal component θ and φ, θ is rotates away from the z-axis and φ is rotates away from the x-axis. The spherical coordinate system is shown in Figure 2. 1

$$G = G_\theta + G_\varphi \tag{3.3}$$

The partial gains G_θ and G_φ are expressed as following:

$$G_\theta = \frac{4\pi U_\theta}{P_{in}} \tag{3.4}$$

$$G_\varphi = \frac{4\pi U_\varphi}{P_{in}} \tag{3.5}$$

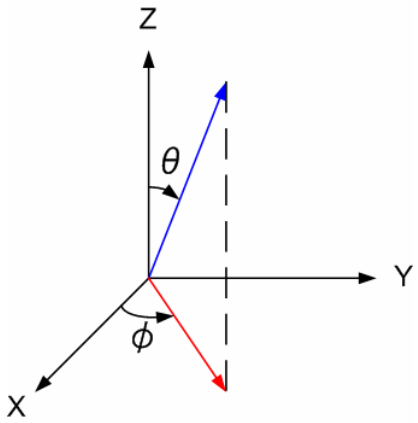

Figure 2. 1 Spherical coordinate system for antenna characterisation.

II.II Polarization

Polarization of an antenna in a given direction is defined as “the polarization of the wave transmitted by the antenna” which means “that the property of an electromagnetic wave describing the time varying direction and relative magnitude of the electric-field vector, specially, the figure traced as a function of time by the extremity of the vector at a fixed location in space, and the sense in which it is traced, as observed along the direction of the propagation” [1]. The polarization can be classified into different categories.

II.II.I Co-polarization and cross-polarization

At each point of the radiation sphere the polarization is usually resolved in two components: a co-polarization and a cross-polarization component. The co-polarization is a reference polarization, which can be linear or circular and usually corresponds to the desired antenna polarization. The cross-polarization is orthogonal to the co-polarization.

II.II.II Linear, circular and elliptical polarizations:

Here we suppose that the electromagnetic wave propagate along z direction and the three components E_x, E_y and E_z along XYZ directions of the electrical field $\vec{E}$ are given by equation 3.6.

$$\vec{E} = \begin{pmatrix} E_X \\ E_Y \\ E_Z \end{pmatrix} = \begin{pmatrix} E_{X0}Cos(wt - kt + \phi_X) \\ E_{Y0}Cos(wt - kt + \phi_Y) \\ 0 \end{pmatrix} \quad (3.6)$$

E_{x0}, E_{y0} and E_{z0} are the maximum magnitude of the electrical field in their respective direction.

According to the different situation, the polarization can be classified into three forms as following:

- **Linear polarization**

The electric field is linearly polarized when

$$, \Delta\phi = \phi_Y - \phi_X = n\pi \text{ , } n \text{ is an integer} \quad (3.7)$$

The vector which describes the electric field at a point in space as a function of time is always directed along a line (Figure 2. 2).

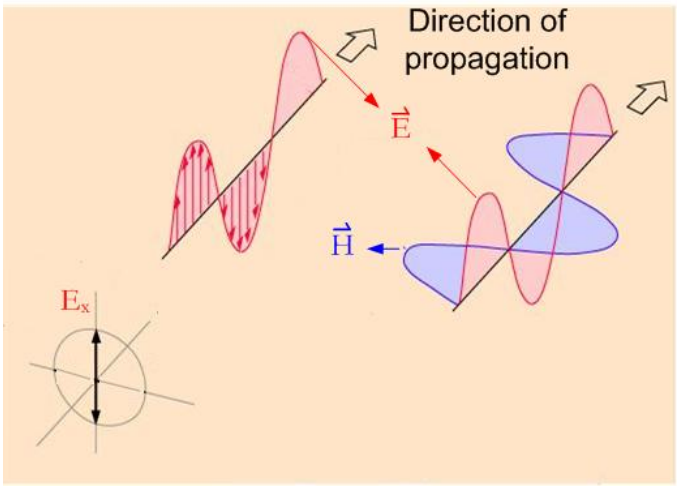

Figure 2. 2 Linear polarization.

The pyramidal horn antenna radiates a linear polarization, the E plane is shown in the Figure 2. 3:

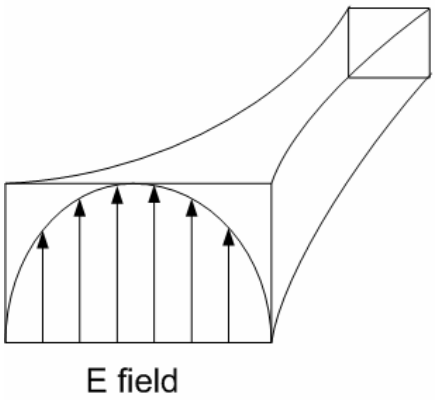

Figure 2. 3 E-plane for a pyramidal horn antenna.

- **Circular polarization**

The field is circularly polarized when equations 3.9 and 3.10 are satisfied (Figure 2. 4):

$$E_{X0} = E_{Y0} \tag{3.8}$$

$$\Delta\phi = \phi_Y - \phi_X = \frac{1}{2}\pi + 2n\pi. \text{, } n \text{ is an integer.} \tag{3.9}$$

The electric field has two orthogonal linear components and these two components have the same magnitude and the time-phase difference of odd multiple of 90°.

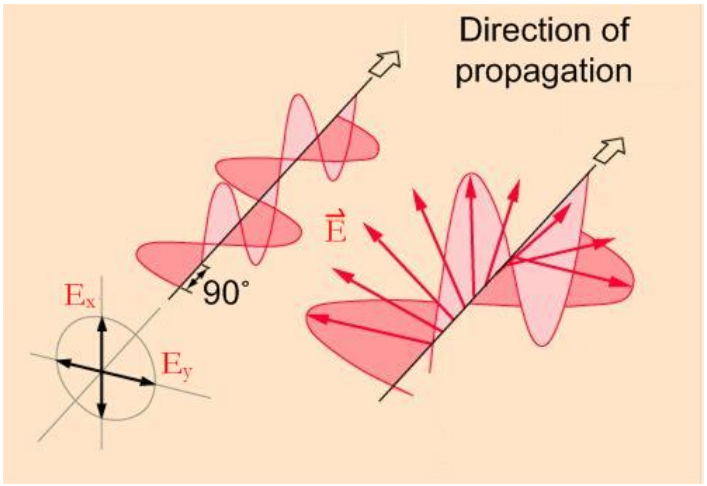

Figure 2. 4 Circular polarization.

According to the sense of the rotation is viewed as the wave travels from the observer, the circular polarization can be defined as clockwise polarization and counterclockwise polarization. If the rotation is clockwise, the wave is right-hand circularly polarized, if the rotation is counterclockwise, the wave is left-handed circularly polarized.

$$\Delta\phi = \begin{cases} -\left(\frac{1}{2}+2n\right)\pi, n = 0,1,2,3... & \text{for clockwise} \\ +\left(\frac{1}{2}+2n\right)\pi, n = 0,1,2,3... & \text{for counterclockwise} \end{cases} \quad (3.10)$$

- **Elliptical polarization**

Elliptical polarization is more general than linear or circular polarization. Linear and circular polarizations are special cases of elliptical polarization.

The field is elliptical polarized when

$$E_{X0} \neq E_{Y0} \quad (3.11)$$

and/or

$$\Delta\phi = \phi_Y - \phi_X \neq \pm\frac{n}{2}\pi \text{ , } n \text{ is integer} \quad (3.12)$$

The elliptical polarization (Figure 2. 5) corresponds to the general case where the two field components are of different magnitude and/or not in phase quadrature

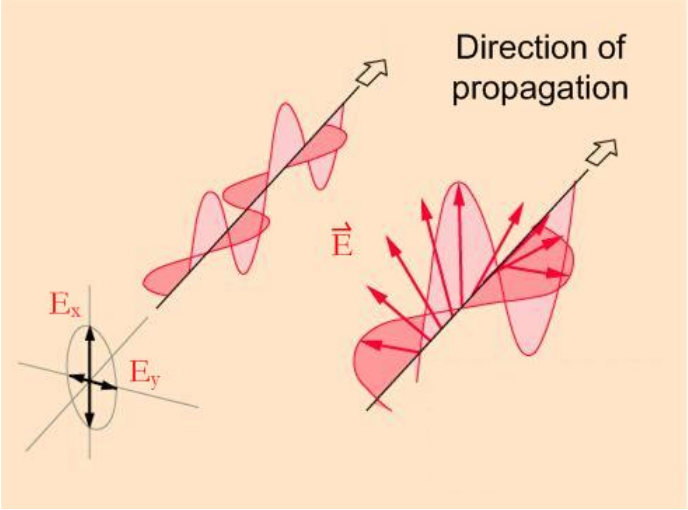

Figure 2. 5 Elliptical polarization.

II.III Radiation pattern

An antenna radiation pattern or antenna pattern is defined as "a mathematical function or graphical representation of the radiation properties of the antenna as a function of space coordinates. In most cases, the radiation pattern is determined in the far-field region and is represented as a function of the directional coordinates." [1]. the radiation property of most concern is the two- or three-dimensional spatial distribution of radiated energy as a function of an observer's position along a path or

surface of constant distance from the antenna. When the amplitude or relative amplitude of the specified component of the electric field vector is plotted graphically, it is called an amplitude pattern, field pattern or voltage pattern. When the square of the amplitude or relative amplitude is plotted, it is called a power pattern.

II.IV Input impedance

This item is defined as “the impedance presented by the antenna and its terminals or the ratio of the voltage to the current at a pair of terminals or the ratio of the appropriate components of the electric to magnetic field at a point”. It can be presented as the sum of the resistance part and the reactance part as following:

$$Z_A = R_A + jX_A \tag{3.13}$$

Z_A: antenna impedance at terminals

R_A: antenna resistance at terminals.

X_A: antenna reactance at terminals.

Antenna resistance can be resolved into two parts, radiation resistance R_r and loss resistance R_L.

$$R_A = R_r + R_L \tag{3.14}$$

Maximum power transfer when the impedance of an antenna matches to the complex conjugate of a receiver or a transmitter’s impedance.

II.V Antenna radiation efficiency

This item is defined as the ratio of the power delivered to the radiation resistance R_r to the power delivered to R_r and R_L.

$$e = \frac{R_r}{R_L + R_r} \tag{3.15}$$

II.VI Bandwidth

The bandwidth of an antenna is defined as “a range of frequencies within which the performance of the antenna, with respect to some characteristic, conforms to a specified standard”. The -3 dB gain bandwidth is commonly used and defined as the frequency band where the radiated energy is above half of the maximum value.

II.VII Axial ratio (AR)

The axial ratio is defined as the ratio of the major axis to the minor axis of the polarization ellipse.

$$AR = \frac{major\_axis}{\min or\_axis} = \frac{OA}{OB} \qquad 1 \le AR \le \infty \tag{3.16}$$

II.VIII Far field and near field regions

The antenna's surrounding space can be subdivided into three regions as a function of the distance away from the AUT.

- Reactive near-field:

$$0 \prec d \prec 0.62\sqrt{\frac{D^3}{\lambda}} \tag{3.17}$$

- Radiating near-field (Fresnel region):

$$0.62\sqrt{\frac{D^3}{\lambda}} \prec d \prec \frac{2D^2}{\lambda} \tag{3.18}$$

- Radiating far-field:

$$d \succ \frac{2D^2}{\lambda} \tag{3.19}$$

Where *D* is the largest dimension of the antenna and D should be larger than the wavelength (D>λ).

The radiation pattern is measured in the far field region.

II.IX Friis transmission equation

The Friis transmission equation can be applied in the far-filed range, which means that the angular field distribution essentially is independent of the distance. The equation calculates the ratio of the power received by the receiving antenna to the power transmitted by the emitting antenna [3, 4].

$$\frac{\mathrm{Pr}}{Pt} = e_t e_r \left(1 - |\Gamma_t|^2\right)\left(1 - |\Gamma_r|^2\right)\left(\frac{\lambda}{4\pi R}\right)^2 D_t(\theta_t, \phi_t) D_r(\theta_r, \phi_r) \tag{3.22}$$

If two polarization-matched antennas are aligned for the maximum directional radiation, and the emitting and receiving antennas are matched to their transmission lines or loads. The equation can be simplified to:

$$\frac{\mathrm{Pr}}{Pt} = \left(\frac{\lambda}{4\pi R}\right)^2 G_{0t} G_{0r} \tag{3.23}$$

In the measurement, the ratio is expressed in decibel (dB), so the equation can be written:

$$\frac{\mathrm{Pr}}{Pt}_{dB} = 20\log\left(\frac{\lambda}{4\pi R}\right) + G_{0t\_dB} + G_{0r\_dB} \tag{3.21}$$

III Integrated spiral antenna on CMOS SOI technology

III.I CMOS SOI technology

CMOS stands for Complementary Metal-Oxide-Semiconductor, it is a technology used for constructing integrated active and passive circuits. [5,6],

Compared with the conventional silicon substrate, SOI (Silicon On Insulator) technology inserts one more insulating layer under the active substrate zone where the active devices and circuits are fabricated and the main substrate is a high-resistivity silicon. Due to this Buried OXide (BOX) layer, a robust insulation from the substrate is provided. Hence it resists to ionization by radiation, decreases the parasitic device capacitance and current leakage in the substrate.

As it has good immunity to the solar wind radiation in space, the first application of the SOI technology was for military and space applications in 1960s. Then it succeeded in the commercial applications in the 1990s, like microprocessors and memory cards [7].

The advantages of the SOI technology over conventional bulk CMOS designs [8-10]:

- High speed

The primary reason of using the SOI technology is lower power consumption than using the bulk CMOS technology. As the SOI technology reduces significantly the junction capacitance and has a higher speed operation. In [7] IBM engineer announced the SOI chips improve performances by 35%, that means a microprocessor which is designed to operate at 400 MHz can achieve speeds of over

500 MHz by using SOI.

- Low power

The presence of the thin dielectric film reduce the inter-device leakage, the SOI chips require as little as one-third the power of today's micro chips at equivalent speed.

- High device density (Miniaturization)

The implementation of SOI technology allows tights layer out design rules, the high integration satisfies the industry's strategies of miniaturization of microelectronics devices.

The Figure 2. 6 shows the topology of the 130 nm CMOS SOI technology (130 nm SOI STMicroelectronic Technology [14]) with different layers [11-13].

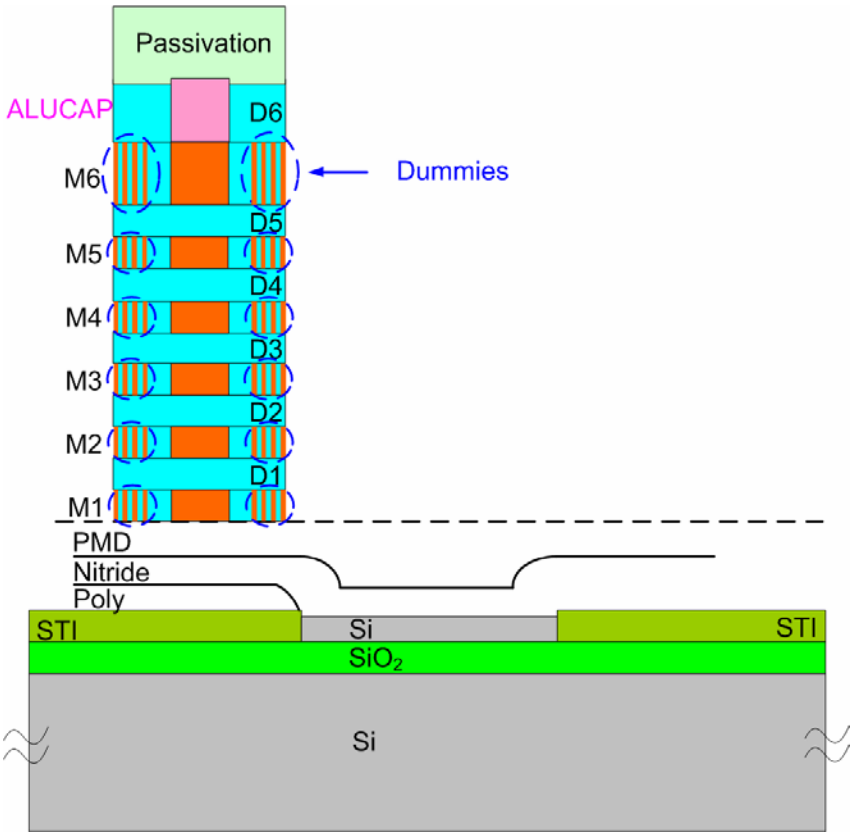

Figure 2. 6 Description of CMOS SOI technology.

There are six (M1- M6) metal layers and six dielectric layers built successively one after another on the high resistivity silicon substrate (KΩ.cm). A buried silicon oxide (SiO_2) layer extends across the entire wafer. The active area where the active elements such as transistor are fabricated is defined above the SiO_2 layer. STI

(Shallow trench isolation) and PMD (Pre Metal dielectric) are the standard dielectric layers which provide lateral isolation from the adjacent devices.

The M1- M6 layers are made of copper and the ALUCAP layer uses aluminum. The D1-D6 layers are composed by the silicide (SiO_2) and nitride (Si_3N_4). The passive elements such as transmission line are fabricated using the metal layers and the ALUCAP layer interconnected together with metal vias as shown in Figure 2. 7.

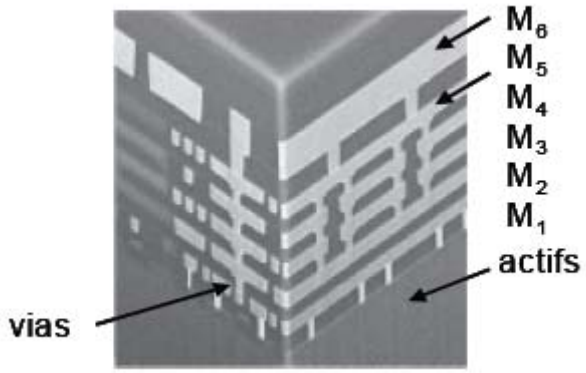

Figure 2. 7 Interconnections among different metal layers.

The CMOS SOI process has several constraints, as design rules require that the metallic density should be between 20% and 80% of an certain micro square meters' surface. In order to meet these design rules, some small dummy metallic squares are present in every metal layer. These dummies should be much smaller than the guided wavelength at 60GHz band.

III.II Integrated spiral antenna

The first AUT is a dual-arm Archimedean spiral integrated antenna realized on 130-nm CMOS SOI technology [15]. Figure 2. 8 shows the top view of the chip. The chip is composed of a dual-arm spiral, a CoPlanar Stripline (CPS) as a feeding line, a balun as CPS-GSG (Ground-Signal-Ground) transition and the GSG feeding pads. In figure b, the antenna is surrounded by small dummy metallic squares in order to meet the metallic density requirements of the CMOS process.

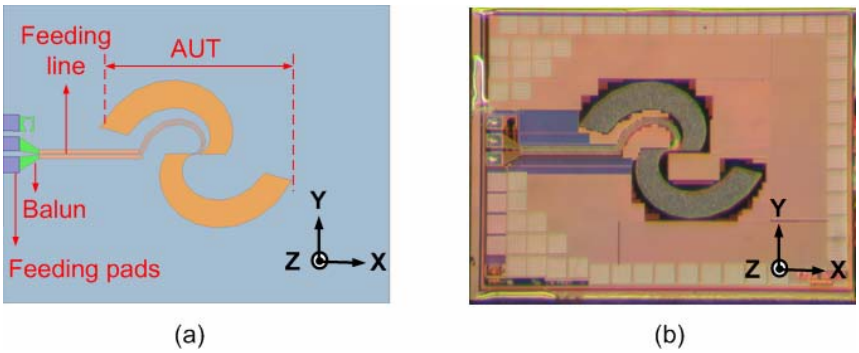

Figure 2. 8 (a) Design of the AUT; (b) photograph of the AUT. (size 2×1.5×0.33 mm^3).

III.II.I Characteristics of the spiral dual-arms antenna

Spiral design is one of the large-band design technique, its bandwidth depends on the as the distances r_1 and r_2 which determine the highest and lowest cutoff frequencies f_{high} *and* f_{low} of the antenna (Figure 2. 9). Over a wide range of frequencies, the spiral antenna is a frequency independent antenna with a nearly constant matching impedance.

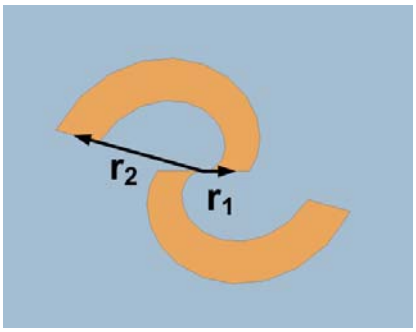

Figure 2. 9 Spiral antenna element.

r_1 and r_2 represent the inner and outer radius of the arms. r_1 measures from the centre of the spiral (0,0.0) to the centre of the first turn while the r_2 measures from the centre of the spiral to the centre of the most outer turn.

The lowest and highest operating frequencies are f_{low} and respectively.

$$f_{low} = \frac{c}{2\pi r_2 \sqrt{\varepsilon_{reff}}} \tag{3.22}$$

$$f_{high} = \frac{c}{2\pi r_1 \sqrt{\varepsilon_{reff}}} \tag{3.23}$$

Where

c represents the speed of light.

ε_{reff} represents the relative effective dielectric constant due to the presence of the CMOS substrate.

The total length of the two spiral arms of the antenna is 2 mm and the arms are fabricated \using the six (M1 to M6) metal layers and the ALUCAP layer with a total thickness of 5.75 µm (Figure 2. 6). The simulation model is created using the software Ansys-HFSS [16]. The figures 3.10-3.12 represent the simulation of the dual-arms antenna. It is a wideband antenna, operating in the 50-65 GHz range with a theoretical reflection coefficient below -8 dB for theoretical responses (Figure 2. 10). Figure 2. 11 shows the two simulated gain components G_X and G_Y as a function of frequency in the broadside direction. The maximum total gain is 0.36 dBi at 62 GHz (Figure 2. 12). This AUT is elliptically polarized with an axial ratio higher than 5 dB across the bandwidth and a polarization direction rotating with frequency, i.e. the main polarization component is along X below 61 GHz and along Y above 61 GHz (Fig. 5). The simulated radiation efficiency is 81% at 62 GHz.

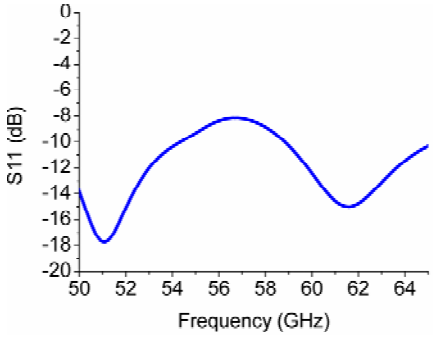

Figure 2. 10 Simulated reflection coefficient of the integrated spiral antenna.

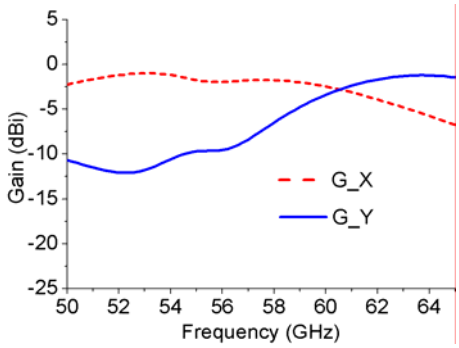

Figure 2. 11 Simulated gain in the broadside direction (θ = 0°) as a function of frequency.

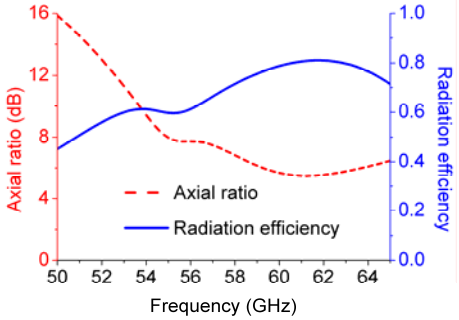

Figure 2. 12 Simulated axial ratio and radiation efficiency in the broadside direction (θ = 0°) as a function of frequency.

III.II.II Influence of feeding elements

The simulation results in section a) only considered the spiral elements. However, the other elements which are the parts of the final chip can have some influences. In this section, we are going to discuss the feeding lines' influence on the radiation pattern.

In Figure 2. 13, we compare the radiation patterns in the ZX- and YZ- plane with two polarizations of three simulation models at 59 GHz:

- ✓ Model 1 represents the spiral antenna.
- ✓ Model 2 represents the spiral antenna plus the CPS line.
- ✓ Model 3 represents the spiral antenna plus the CPS line plus the balun plus the GSG pads (complete chip).

Model 1 has been already presented in detail in the previous section, model 2 adds a 960 μm CPS line which uses only the top (M6) metal layer and the ALUCAP layer. Its total thickness is of 1.84 μm. The two top layers have been chosen for the sake of a good control of the CPS line characteristic impedance. Model 3 adds a balun and GSG pads. The balun makes a balanced-unbalanced transition. The GSG pads are at the edge of the chip, they are standard GSG pads with a pitch of 100 μm , the dimensions of the each pad are 70×86 μm^2.

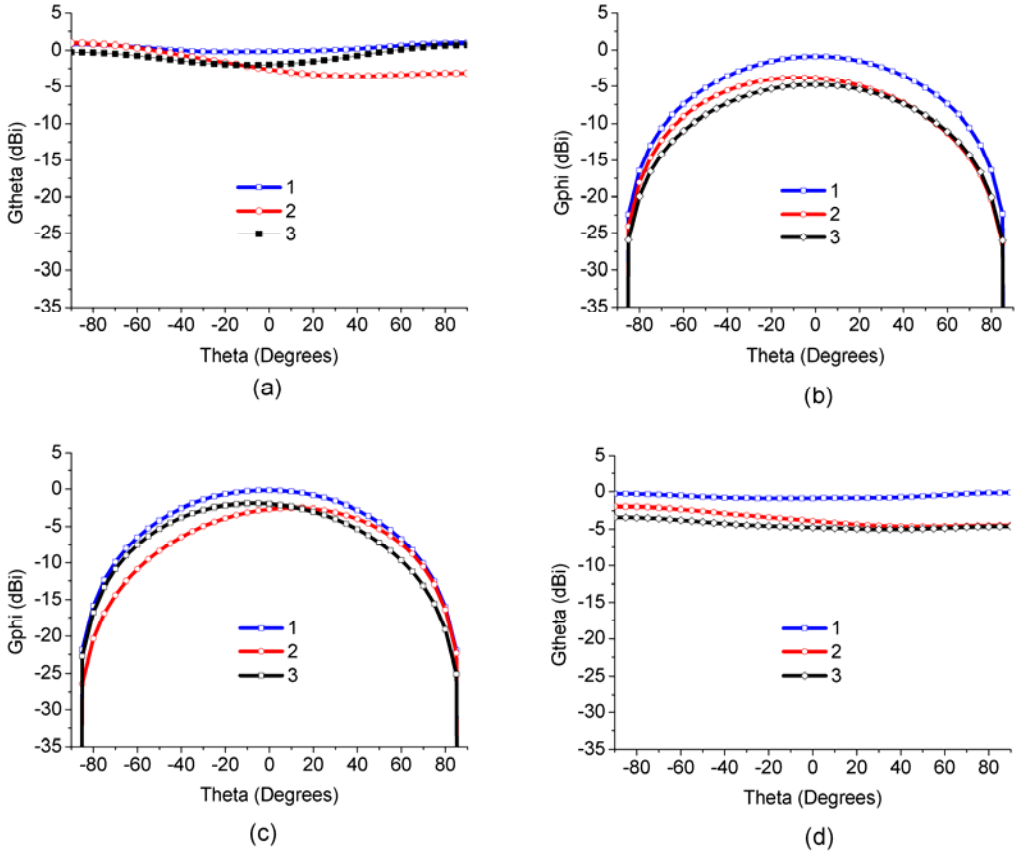

Figure 2. 13 Simulation results of three models: (a) ZX plane co- polarization; (b) ZX plane cross-polarization; (c) YZ plane co-polarization; (d) YZ plane cross-polarization.

As we can see, the presence of the feeding lines changes slightly the shapes of the radiation patterns of 2-3 dB as the feeding elements act as a part of the radiating elements with the spiral antenna. The influence of the feeding elements is asymmetric, it is because the presence of different feeding elements are asymmetric as well, thus the patterns are no longer symmetric to the centre θ=0 (centre of the spiral arms). The gains are decreased as the elements loss adds to the spiral antenna.

Figure 2. 14 also shows the simulated radiation pattern of simulation model with the feeding elements only, its end is loaded with adapted impedance. Its maximum gain is around -17dBi, that means the feeding elements do not radiate themselves.

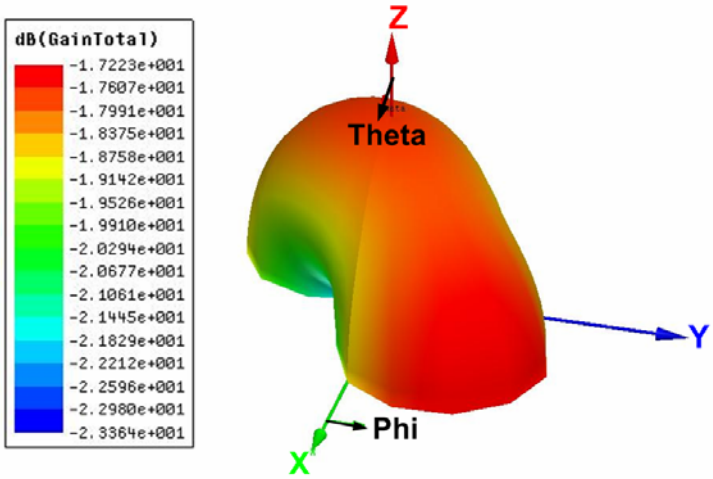

Figure 2. 14 Simulation of the 3D radiation pattern of the CPS plus GSG pads.

III.II.III Simplified simulation model

The simulation models are created using HFSS simulator. As there are very large differences in scale between small metallic or dielectric structures and the whole chip, which can make a direct simulation of the chip impractical, several simplifications have been done to meet the current computing resources. The following elements are simplified compared to the CMOS topology (Figure 2. 15):

- The dummies: these metal squares are not present in the simulation model.
- Merged dielectric layers: some dielectric layers are merged into one equivalent layer. (Table 2.1)
- Merged metal layers: we used a single conductivity for the layer copper and aluminum. (Table 2.2)

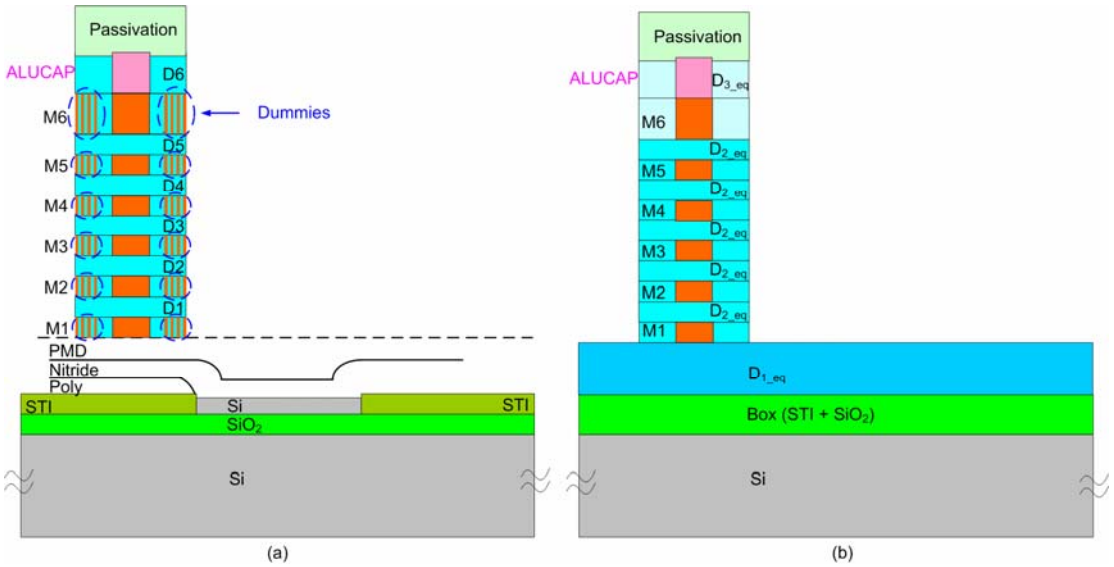

Figure 2. 15 (a) Description of the CMOS technology; (b) simulation model.

Table 2.1 lists relative permittivity of the different dielectric layers of the SOI technology and the simplified simulation model with equivalent values. The layers among the STI and PMD are merged into one equivalent dielectric layer D_{1_eq}. The D1-D5 are merged as layer D_{2_eq}, the D6 and the dielectric around the ALUCAP are merged into layer D_{3_eq}.

To calculate the relative permittivity, Krasweski's equivalent substrate model is used [17]. Figure 2. 16 represents the Krasweski's model with two layers, the heights of the host and inclusion layers are h_i and h_h respectively.

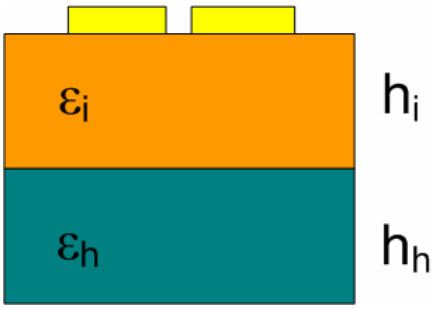

Figure 2. 16 Krasweski's equivalent substrate.

$$h_{eq} = h_i + h_h \tag{3.24}$$

$$\varepsilon_{r\_eqi} = \left[\sqrt{\varepsilon_h} + v_i\left(\sqrt{\varepsilon_i} - \sqrt{\varepsilon_h}\right)\right]^2 \tag{3.25}$$

Where as v_i is the ratio of the volume of the layer i to the total volume. The volume equals the surface S times corresponding height. As S is equal to host layer and inclusion layer: [18]

$$v_i = \frac{Sh_i}{Sh_i + Sh_r} = \frac{h_i}{h_i + h_r} \tag{3.26}$$

Table 2.1 Simplified simulation model with equivalent dielectric layers.

Dielectrical layer		ε_r		ε_{r_eq}	tgδ
Passivation	Nitride	8.1	Passivation	5.77	0.004
	Oxide	4.2			
Diel 6	Oxide	4.2	D_{3_eq}	4.19	0.004
	Nitride	8.1			
Diel 5	Oxide	4.2	D_{2_eq}	3.96	0.004
	Nitride	8.1			
Diel 4	Oxide	3.7			
	Nitride	8.1			
Diel 3	Oxide	3.7			
	Nitride	8.1			
Diel 2	Oxide	3.7			
	Nitride	8.1			
Diel 1	Oxide	3.7			
	Nitride	8.1			
PMD on poly	Oxide	4.2	D_{1_eq}	4.22	0.004
	Nitride	7.0			
Poly	Poly	303			
STI	Oxide	3.4	Box	4	0.004
SiO_2		0.0018			
Silicom High resistivity	Silicon	11.7	Si	11.7	σ = 0.1

Table 2.2 Simplified simulation model with equivalent metal layer.

Metallic layer		Conductivity σ [S/m]
Alucap	Aluminum	2×10^7
Metal 6	Copper	
Metal 5		
Metal 4		
Metal 3		
Metal 2		
Metal 1		

Table 2.2 presents the conductivity of the different metallic layers used in the simulation.

IV Integrated antenna on silicon interposer

IV.I Fabrication process of CMOS interposer

The antenna is fabricated on two wafers: the top part is composed of two thick damascene copper layers on a High Resistivity (HR) silcon (KΩ.m) with a thickness of 120 µm, the bottom part is composed of a copper layer on a standard silicon with a thickness of 725 µm (Figure 2. 17a).

The antenna is a folded dipole fabricated on top wafer. Two copper layers are connected through the copper via in the Inter Metal Dielectric (IMD) layer [19]. To decrease the effective permittivity in order to increase the antenna's bandwidth [18,19], a cavity is etched on the bottom silicon substrate (Figure 2. 17 b), the top and bottom metal layers are connected by several Through-Silicon-Vias (TSV).

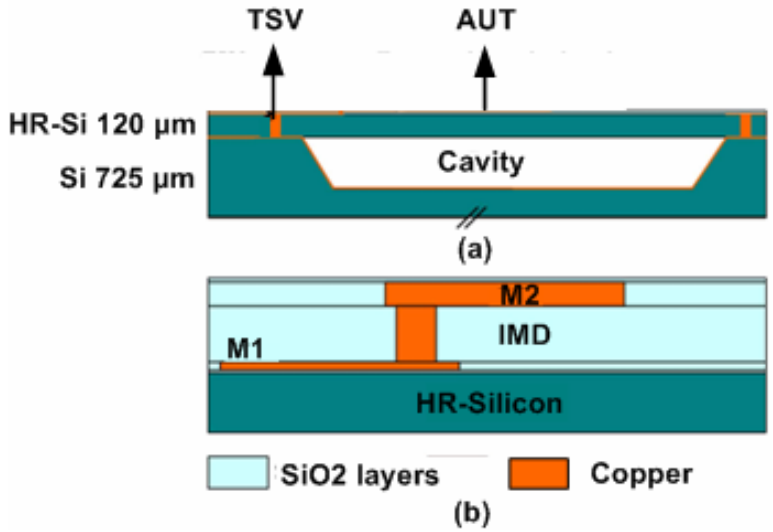

Figure 2. 17 (a) Cross section of the silicon interposer technology; (b) details of the tow metal back-end on the top substrate.

IV.II Integrated folded dipole

The antenna is composed of a folded dipole and its associated t-line on the top silicon layer. The folded dipole has an input impedance of 100 Ω, and is fabricated on the metal layer M2. It is associated with a CoPlanar Stripline (CPS) quarter-wavelength transformer which is also fabricated on M2. A CPS-microstrip balun is used to provide a 50 Ω microstrip input port. A 0.7 mm microstrip line link to the balun to the GSG pads on the side of the folded dipole. The balun and the microstrip line are fabricated on the metal layers M1 M2 with a SiO2 Inter Metal Dielectric (IMD). An empty place of 1.9×2.8 mm^2 on the left of the chip is reserved for a transceiver in the future. Figure 2. 18 shows the top view of the simulation model of the chip and Figure 2. 22 presents the photograph of the cavity-backed dipole with a zoom on the balun and the GSG probe pads.

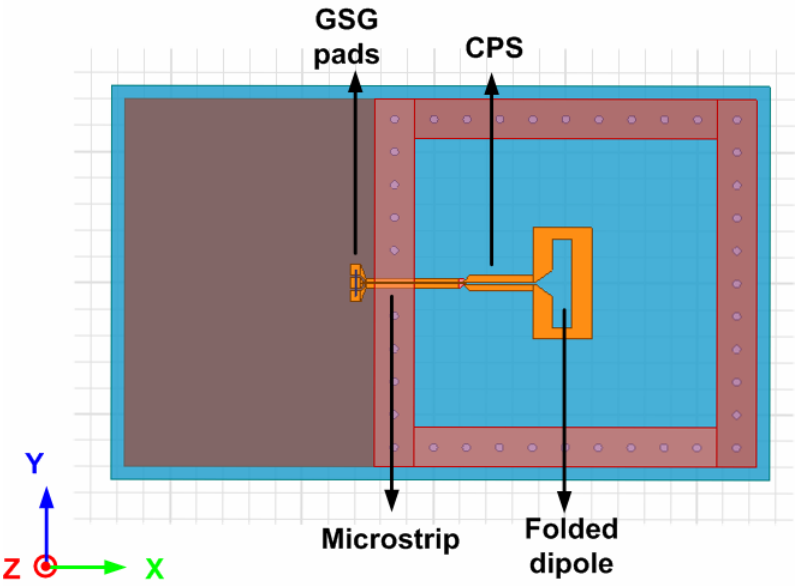

Figure 2. 18 Simulation model of the folded dipole antenna (5×3×0.88 mm3).

IV.II.I Characteristics of the folded dipole

It covers the 57-66 GHz standard band with a S11 under -8dB (Figure 2. 19). Figure 2. 20 shows the two simulated gain components as a function of frequency in the broadside direction. The main polarization component is along Y, it equals to polarization along X at 53 GHz. The maximum gain is 8.4 dBi at 67.5 GHz.

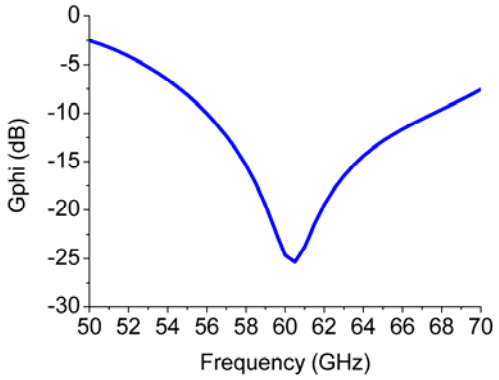

Figure 2. 19 reflection coefficient of simulated folded dipole.

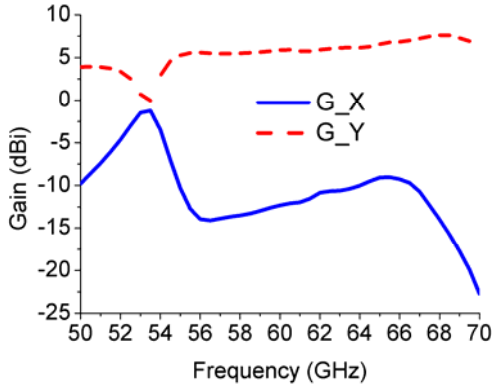

Figure 2. 20 Simulated gain in the broadside direction (θ = 0°) as a function of frequency.

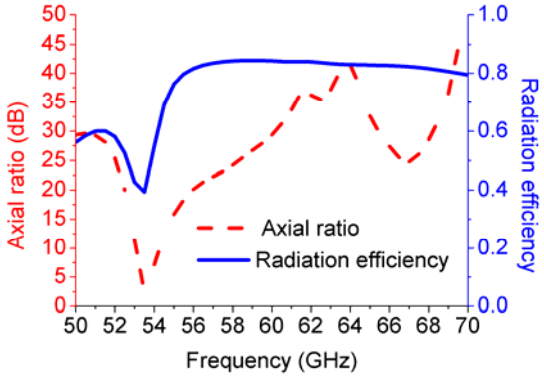

Figure 2. 21 Simulated axial ratio and radiation efficiency in the broadside direction (θ = 0°) as a function of frequency.

IV.II.II Influence of feeding elements

To further understanding the influence of the feeding elements on the radiation patterns, Figure 2. 23 shows three simulation mode:

- ✓ Model 1: cavity backed folded dipole
- ✓ Model 2: cavity backed folded dipole with a CPS line of 0.522 mm and a microstrip-CPS balun.
- ✓ Model 3: cavity backed folded dipole with a CPS line, a microstrip-CPS balun, a 0.7 mm microstrip line and a GSG probe pads.

There is minus influence of the feeding elements on the co-polarized gain compoment,patterns in the ZX- and YZ- planes, but the cross-polarization suffered more from their parasitic radiation.

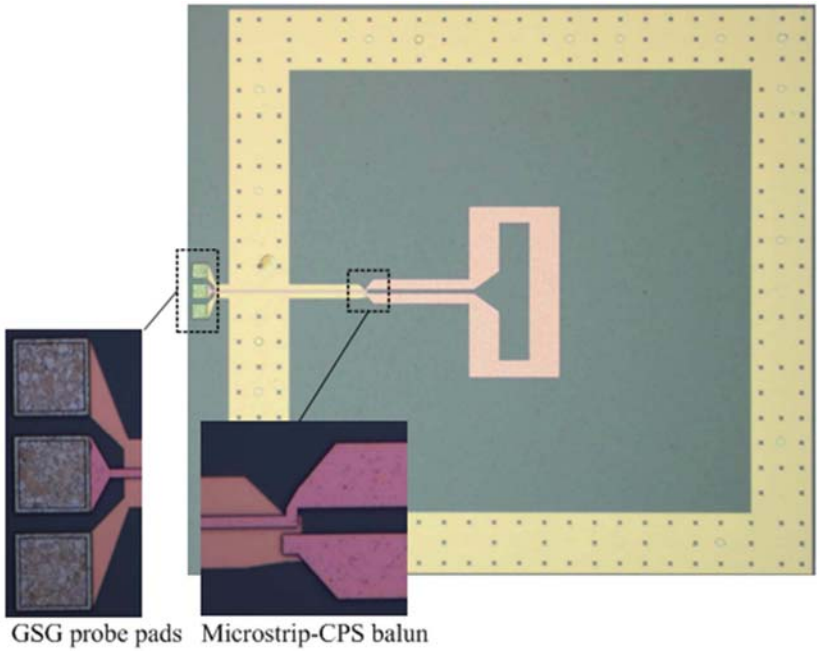

Figure 2. 22 Photographs of the cavity-backed folded dipole antenna.

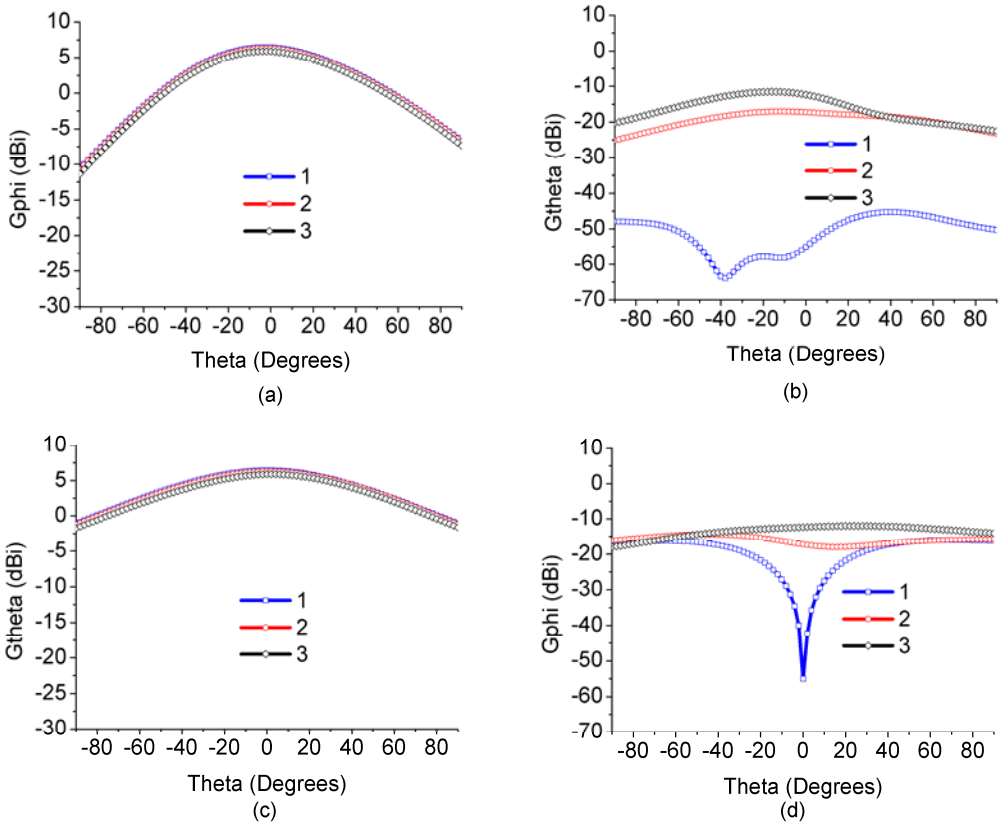

Figure 2. 23 Folded dipole: (a) ZX plane co-polarization; (b) ZX plane cross-polarization; (c) YZ plane co-polarization; (d) YZ plane cross-polarization.

V Dipole antenna

In this section we describe how we included the influence of the probe system on the AUT in the simulation, given the big difference in scale between the integrated spiral (1.5×2 mm^2) and the probe system (several cm^2). We can not simultaneously simulate the AUT plus the probe system as the simulation is too slow. Instead, we introduce a λ/2-dipole antenna as a reference antenna at 60 GHz.

We created three models using Ansys-HFSS as shown in Figure 2. 24.

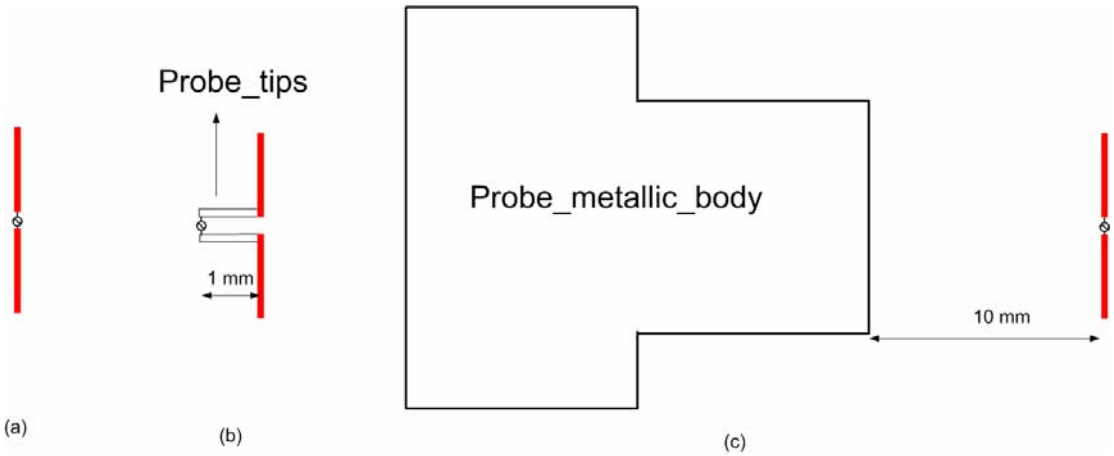

Figure 2. 24 Simulation models: (a) Dipole; (b) Dipole fed by probe tips; (c) Dipole with probe metallic body.

- Model (a) is a λ/2-dipole fed by a lumped port. The radius, length and distance between the two λ/4 dipole elements of the dipole are 3 μm, 1.18 mm and 3 μm respectively. With these characteristics, the dipole is adapted to 50 Ω.
- Model (b) is a λ/2-dipole fed by a lumped port via probe tips, with the probe tips modeled as a coplanar stripline of length 1 mm.
- Model (c) is a λ/2-dipole next to a metallic block of width and height equaling 2 cm. This block mimics the presence of the probe's metallic body.

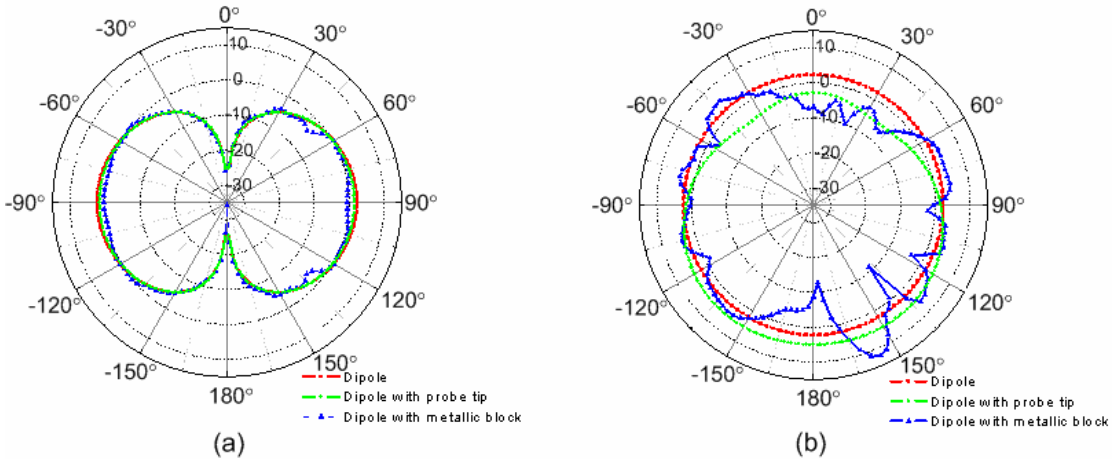

Figure 3. 25 (a) Gain E_θ in E- and (b) E_φ in H-plane.

As we can see in the simulation (Figure 3. 25), the presence of the probe tips (model (b)) has less influence than the presence of a metallic block (model (c)) on the radiation pattern, relative to the dipole-only model (model (a)). Thus in Chapter III we focus on keeping the metallic body as far away as possible from the AUT to reduce such effects.

VI Conclusion

In this chapter, we presented several AUTs and their simulated performances. The integrated spiral antenna on the CMOS SOI technique is the AUT for the under probe characterization (chapter III) and flexible line characterization (chapter IV), the AUT2 is tested by the under probe characterization (chapter III). As the probe's body has big influence on the radiation patterns, we focus on reducing this influence in Chapter III.

References:

[1] C.A. Balanis, *Antenna theory: analysis and design*, Harper & Row New York, 1982.

[2] G.E. Evans, "Antenna measurement techniques," *Norwood, MA, Artech House, Inc., 1990, 238 p.*, vol. 1, 1990.

[3] H.T. Friis, "A note on a simple transmission formula," Proc. Of the IRE, vol. 34, No. 5, pp. 254-256, May 1946.

[4] IEEE Standard test procedures for antennas, IEEE Std 149-1979(R2008).

[5] B. Razavi, *Design of analog CMOS integrated circuits*, McGraw-Hill Singapore, 2001.

[6] C.H. Doan, S. Emami, A.M. Niknejad, and R.W. Brodersen, "Millimeter-wave CMOS design," *IEEE Journal of Solid-State Circuits*, vol. 40, no. 1, 2005, pp. 144-155.

[7] IBM "SOI Technology: IBM's Next Advance in Chip Design," [online]. Available: http://eesun.free.fr/DOWNLOAD/FREEDOC/soipaper.pdf

[8] S.I. Yasuhiro FUKUDA, Masahiro ITO, “SOI-CMOS Device Technology,” OKI Technical review, vol. 68, no. Number 4, 2001.
[9] R. Simonton, “SPECIAL REPORT SOI Wafer Technology for CMOS ICs,” Simonton Associates, 2002.
[10] J.M. Stern, P.A. Ivey, S. Davidson, and S.N. Walker, “Silicon-on-insulator (SOI): A High Performance ASIC Technology,” Custom Integrated Circuits Conference, 1992., Proceedings of the IEEE 1992, pp. 9.2.1-9.2.4.
[11] M. Barakat, “Dispositifs radiofréquences millimetriques pour objets communicants de type smart dust,” Ph.D thesis, Joseph Fourier University, Grenoble, 2008.
[12] C. Pavageau, “Utilisation des technologies CMOS SOI 130 nm pour des applications en gamme de fréquences millimétriques,” Ph.D thesis, Lille 1 University, Lille, 2005.
[13] A. Triantafyllou, “Etude réalisation et caractérisation d’interconnexions radiofréquences pour les circuits intégrés silicium des générations a venir,” Ph.D thesis, Joseph Fourier University, Grenoble, 2006.
[142] STMicroelctronics [online]. Available: http://www.st.com/internet/com/home/home.jsp
[15] M. Barakat, C. Delaveaud, F. Ndagijimana, “Circularly Polarized Antenna on SOI for the 60 GHz Band. Antennas and Propagation,” EuCAP 2007, Edinburgh, 2007.
[16] Ansys-HFSS [online]. Available: http://www.ansoft.com/products/hf/hfss/
[17] Kraszewski, "Prediction of the dielectric properties of two phases mixtures," Journal of Microwave Power, vol. 12, pp. 215, 1977.
[18] A. Enayati, S. Brebels, W. Raedt, G. Vandenbosch, and A. Raisanen, “Antenna-in-package solution for 3D integration of millimeter-wave systems using a thin-film mcm technology,” 2011 IEEE MTT-S Int. Microwave Symp. Dig., June 2011.
[19] L. Dussopt et al., “Silicon Interposer with Integrated Antenna Array for Millimeter-Wave Short-Range Communications,” submitted to IEEE MTT-S Int. Microwave Symp., 17-22 jun. 2012, Montreal, Canada.

Chapter III
Characterization of probe-fed millimeter-wave integrated antennas

I Introduction

In this chapter, we are going to present the characterization of millimeter-wave antennas under probe. For this purpose, we designed and fabricated a new 3D test bench for probe-fed AUTs above 26 GHz [1] with a test antenna rotating above the AUT in a single plane over a 180° angular sector. The test bench is designed specifically for low directivity integrated antennas because of the specific features for feeding the AUT. This test bench will be presented in detail in section II. In section III, we will present the three different millimeter wave RF probes that we used for characterization. Among these three, one is standard and the other two are customized probes with extended coaxial lines. In section IV, we compare the performances of these three probes. In this section, we also present a second test bench which is an improved version of the first one. We compare the performances of these two test benches using the probe with the best performance.

II Design of the characterization set-up

In this section we present the design of the first test bench.

II.I Hardware configuration

At millimeter wavelengths, an AUT is normally of millimeter scale and the measuring antenna is often a horn antenna, which is chosen for its high gain and high directivity. The horn antenna's size is usually around 20x30x60 mm which is large compared with the AUT. The AUT is also supplied by a probe which is much heavier than the AUT and the horn antenna. Due to these significant size differences, some special design requirements apply:

- Relative position of the two antennas: when measuring a small antenna, we

should rotate the measuring antenna about the AUT because it is impractical to rotate the whole feeding system, which would involve rotating the probe, while ensuring a good connection between the probe and the AUT.

- Precise position of AUTs. Two laser diodes [2] are installed in the setup to ensure the accurate positioning of the AUTs. One laser diode is placed along the motor axis to ensure the altitude and the centre in the left/right direction as viewed from the motor. The other laser diode is placed at the end of the motorized arm along the test antenna's axis to ensure the centre in the forward/backwards direction as viewed from the motor.
- Probe system: our test bench is designed for the probe feeding technique due to its higher precision.

In accordance with these requirements, we now present a simplified schematic of our setup, which has three parts: a base (A), a rotating system (B) and a probe system (C), as shown in Figure 3. 1:

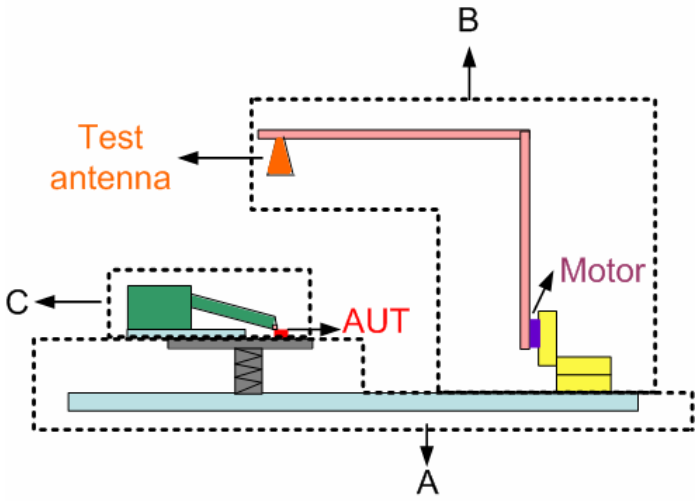

Figure 3. 1. Simplified schematic of the setup.

(A) The base: the whole setup is fixed on a honeycomb board, which has a hexagonally-structured core and one up- and one down- sheet which help to avoid and isolate unexpected shocks or vibrations. On the honeycomb, there is a manually-adjustable chuck which can vary the altitude of the probe system from 7 cm to 24 cm. The AUTs are fixed horizontally on top of this chuck.

(B) The rotating system: the motorized arm is connected to a stepping motor controlled by a motor controller [3]. This motor is fixed on a XYZ positioner, with a precision of ±1 μm in each direction [4]. The arm is made of Plexiglass with a

relative permittivity ε_r of 2.5 [5]. The test antenna is placed at the end of the motorized arm.

(C) The probe system: this system is composed of three parts: a RF probe, a probe translation stage and a metallic fixture. The RF probe is fixed on the probe translation stage which moves the test head on a 5 μm scale along the X-, Y- and Z-directions [6]. Additionally, the test head can twist through an angle of 10° to ensure the planarity of the probe tips in order to increase the contact quality between the AUT and the tips.

Apart from these main three elements, the whole setup is covered with absorbers to minimize electromagnetic scattering and reflections. Two kinds of absorber are used here: some absorber sheets are used around the AUT to minimize unwanted reflection from the metallic ground, and some pyramid-shaped absorbers are used all around the setup to trap electromagnetic waves. The attenuation coefficient of these absorbers is -45 dB in the 60 GHz frequency band [7].

Figure 3. 2 shows the photograph of the this test bench with correspondent parts, The dimensions of the set-up are 90×60×65 cm^3. The distance between the AUT and test antenna can vary between 5 cm to 35 cm as the rotating arm can be fixed on the motor in different positions.

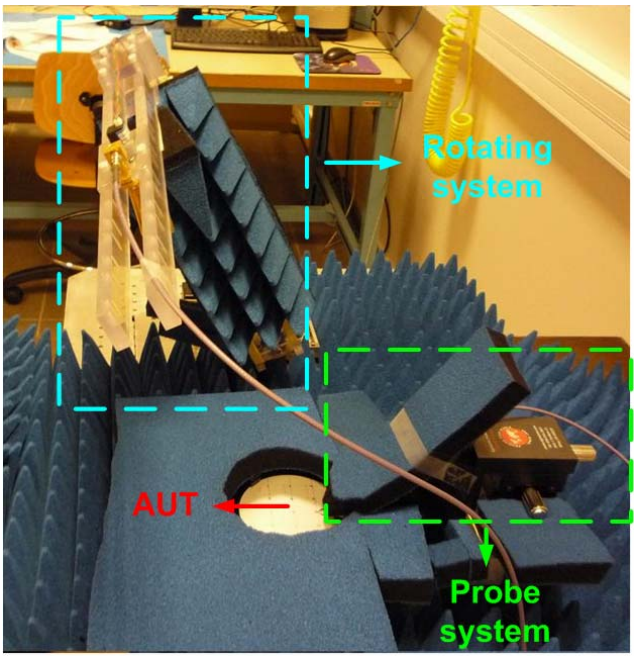

Figure 3. 2 Photograph of the set-up.

II.II Instruments and program

Apart from the hardware we presented in the previous section, to characterize the radiation pattern, some apparatus are used during the experiments (Figure 3. 3):

- Measurement: a Vector Network Analyzer (VNA) (Anritsu 37397C) [8] is used to measure the transmission coefficient between the antennas.
- Amplifier (HLNAV-218 S/N 2K702139) [9]: the gain of the amplifier is around 30 dBi in the 60 GHz frequency band.
- Coaxial cable: We used two semi-flexible coaxial cables of 90 cm length and with the characteristic impedance of 50 Ω. Its flexibility enables the smooth rotations.

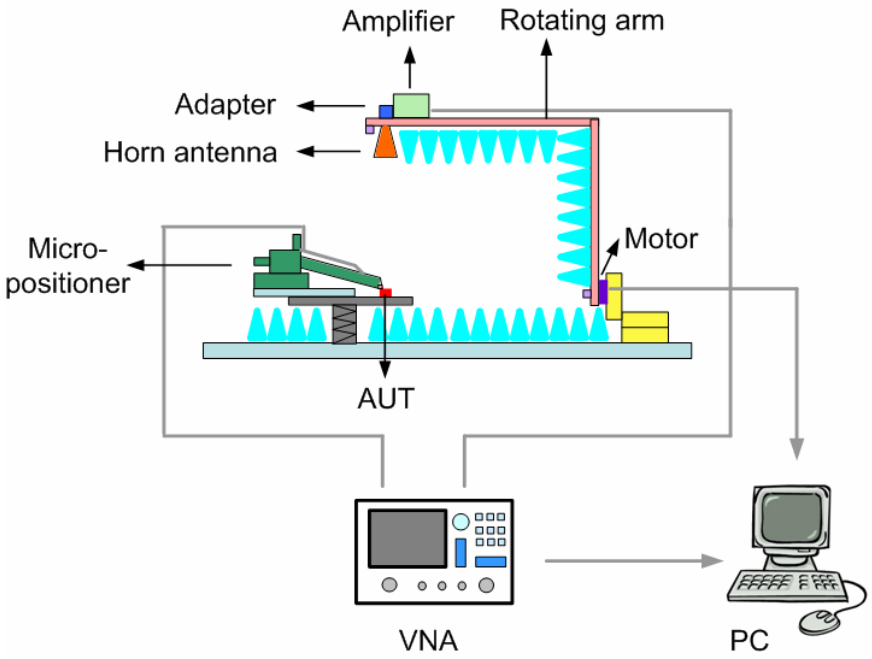

Figure 3. 3 Schematic diagram of the setup with apparatus.

The set-up is automated, that means the movement of the rotating arm, the measurement and recording of the data are controlled by a Labview program [10]. Figure 3. 4 shows the diagram of the program.

- Initialization: initialization of the VNA and the motor. In this step, the following initial values are set.

  For the VNA, we set the start frequency, stop frequency, the size of frequency increment steps, the IF bandwidth and the average factor.

  For the motor, we set the initial and maximum rotating speed, the start position, the number of rotations and the size of the angular increments. The number of rotations times the size of the angular increment defines the scanning zone of the rotating arm. For our integrated AUTs, the

scanning zone of interest is the upper half space.

- Rotate the arm: we command the motor to rotate the arm by the given number of degrees with the given angular increments.
- Record data: this step communicates with the VNA and records the data in a matrix.
- Half space: in this step, the program checks if the full angular sector has been covered, if yes, the program writes out the file, otherwise it continues the loop. The arm keeps on rotating and measurement continues.

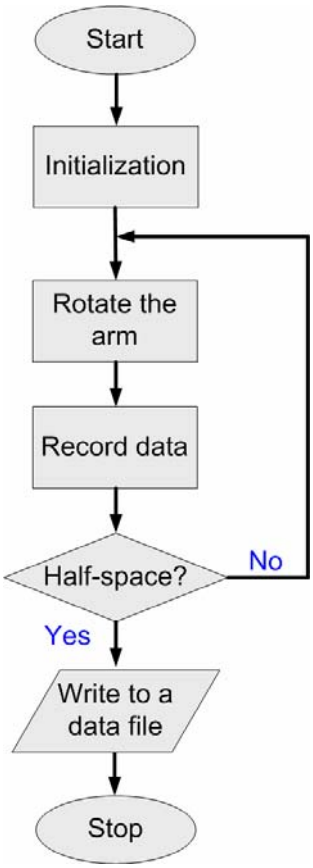

Figure 3. 4 Labview program flow chart.

The test bench is designed for characterization under probe, but with minor modifications, it can also be used to characterize antennas fed through flexible transmission lines (chapter V) or to perform radar cross sections measurement (chapter VI).

III RF probes

III.I Introduction

Probe systems play an important role in test and measurements. Indeed, RF probe systems give much more reliable and precise measurements of integrated circuits (IC) in comparison with the previous state-of-the-art characterization technique which used connectorized boards. Before RF probes were available, wafers were characterized by the following method: the wafer was cut into several individual dies, each die was mounted on a test fixture and bond pads were connected with bond wires. It was very difficult to quantify the RF behavior of a single die due to the difficulty of discriminating between effects due to the die and the effects due to its fixture. Additionally, using and calibrating probes is straightforward, so probe systems are today's method of choice for on-wafer Device-Under-Test (DUT) characterization [11-15].

Microwave on-wafer probes launch RF signals on and off a wafer and transmit the RF signal from the test cable to the probe tips. The probe cable and connector types determine the upper frequency limit of the probe. In today's market, there exist RF probes which operate from the range of direct current (DC) up to 325 GHz, or even 500 GHz [16-17]. For instance, Samoska *et al*. describe the design, simulation, and on-wafer measurements of Submillimeter-wave Monolithic Integrated Circuit (S-MMIC) amplifiers having gain in the 400-500 GHz range [18].

In our characterizations, we used three RF probes: a standard one (Infinity 67-A-GSG-100 supplied by CASCADE Microtech) and two customized probes (Picoprobe 67A-GSG-100 supplied by GGB). They operate from DC to 67 GHz which covers our frequency band of interest.

III.II The structure of a standard RF on-wafer probe

Different types of probes exist in order to meet different measurement needs. These needs are reflected by the design of the probe's connector and tips. For instance, the connector might be designed for a coaxial cable or for a waveguide depending on the frequency. Meanwhile, the configuration of the tips depends on the design of the device, on the type of transmission lines and on the geometry of a wafer's pads. The

commonest geometry in the 60 GHz band is Ground-Signal-Ground (GSG). Compared with Ground-Signal (GS) and Signal-Ground (SG) geometries, the main advantage of the GSG is a better control of the fields around the signal probe.

During our on-wafer characterization, we used an Infinity probe with a pitch of 100μm, its connector is designed for a coaxial cable and its geometry configuration is GSG (Infinity 67-A-GSG-100 supplied by CASCADE Microtech). The pitch is defined as the distance between the center of two adjacent tips. Above 50 GHz, the best performance is achieved with a pitch from 100 μm to 150 μm [18]. As with almost all microwave test equipments, it has a characteristic impedance of 50 ohms.
Figure 3. 5 shows a photograph of the Infinity probe (a), and its three tips (b) as well as its reflection in the DUT substrate (contact view, frontal view) [18].

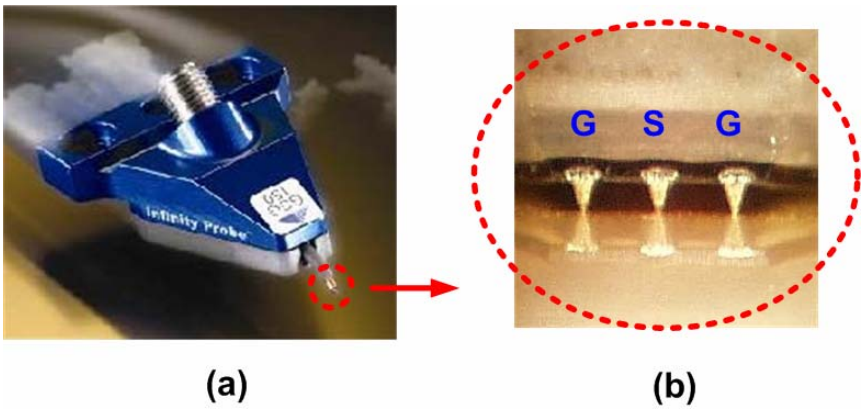

Figure 3. 5. Infinity probe.

To have a better idea of the structure of a standard probe, Figure 3. 6 shows a cross section of it. As we can see in the figure, the standard probe is composed of three parts: the GSG coplanar tips, a coaxial line and a 1.85 mm coaxial connector [13,18,19]. The signal enters at the coaxial connector, passes through the coaxial line and exits through the tips. These tips connect onto the wafer pads to feed AUTs. The part of the coaxial line which is close to the tips is exposed in the air and coated with a thin absorbing material. Its diameter is 1 mm and its length is usually 5-10 mm. The rest of the coaxial line is enclosed in the probe's metallic body of 2-3 cm, and connects to the test equipment through a connector.

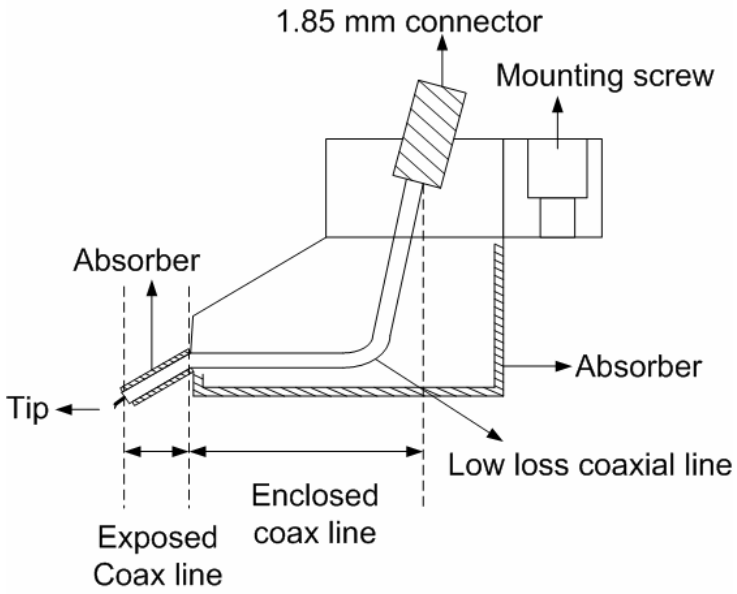

Figure 3. 6. Cross-section of a standard probe.

During characterization, a standard probe is fixed to the probe translation stage as shown in Figure 3. 7. The probe's main body is 4 x 2 x1 cm^3 and the micro-positioner is 100 x 30 x 50 cm^3. These are in close proximity to the AUT which is of millimeter size. This has two consequences: firstly, the probe body causes a masking effect on a significant angular sector of the radiation pattern; secondly, the body of the probe and positioner reflects and scatters the waves radiated by the antenna.

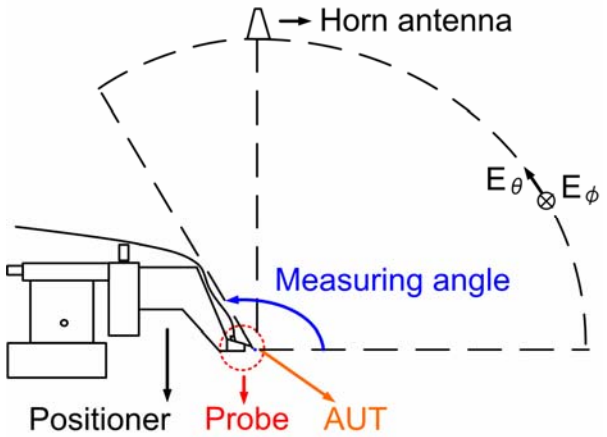

Figure 3. 7. Measurement setup with a standard probe.

III.III The structure of two extended RF on-wafer probes

As just described, there are unwanted masking, reflection and scattering effects

associated with the use of standard probes. Therefore, we propose two customized probes, which we now describe. These two probes are air coplanar probes having a 50 mm coaxial extension between the probe tip and the body (Picoprobe 67A-GSG-100 supplied by GGB). The first probe has a regular connector which connects in the upward direction (Figure 3. 8) and the second probe has a reversed connector which connects in the downward direction (Figure 3. 10).

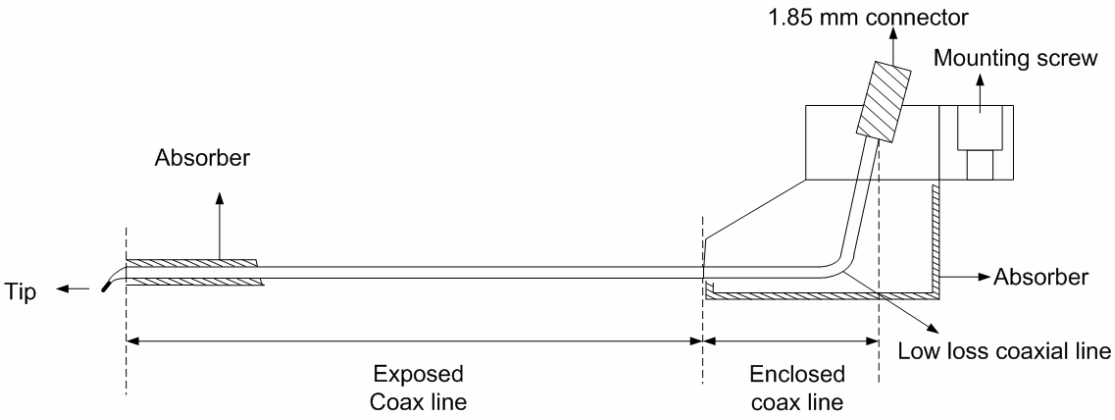

Figure 3. 8. Cross section of the customized probe with 50-mm coaxial extension.

The reason we designed a probe with a 50-mm coaxial extension and a regular connector is obvious: this design keeps the metallic probe body away from the AUT as well as increasing the range of measuring angles (see Figure 3. 9).

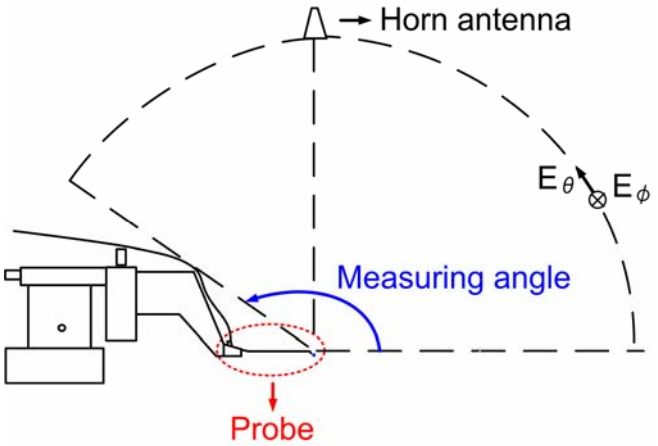

Figure 3. 9. Measurement setup for a customized probe with a 50-mm coaxial extension.

With a different assembly of the probe translation stage and a reversed connector, our second customized probe can achieve an even larger measuring angle as shown in Figure 3. 11.

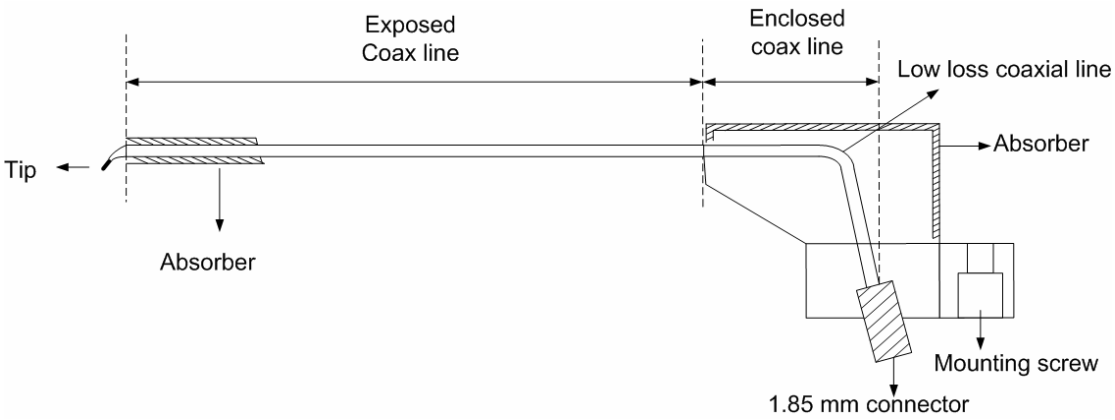

Figure 3. 10. Cross section of the customized probe with 50-mm coaxial line and reversed connector.

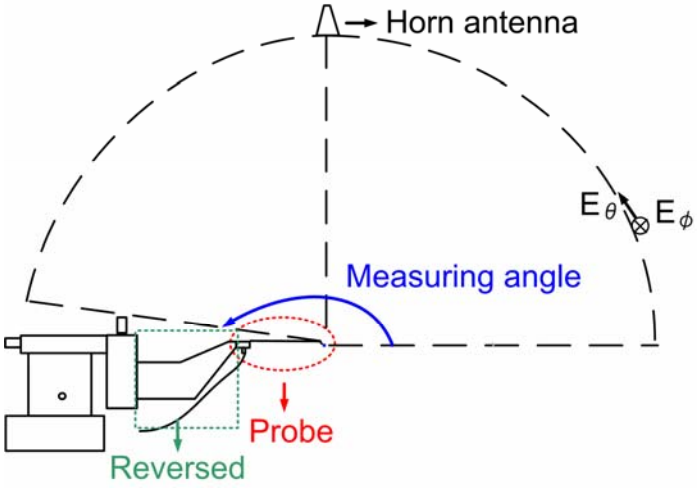

Figure 3. 11. Measurement setup with a customized probe with a 50-mm coaxial line and reversed connector.

III.IV Calibration and gain extraction

We used a VNA to measure the transmission coefficient between the test antenna and the AUT. The port 1 of the VNA is connected to the AUT and the port 2 of the VNA is connected to the test antenna via an amplifier, therefore the AUT is an emitting antenna and the test antenna is a receiving antenna. A full two ports coaxial calibration was performed at the end of the each coaxial cable (Figure 3. 12). We do not include the amplifier in the calibration due to its high isolation in the reverse direction. Assuming a 0 dBi gain AUT, the transmission coefficient would be in the range of -13 to -10 dB. The average noise floor of the VNA was -85 dB. Thus, an excellent dynamic range of 73-76 dB is expected and this is considered appropriate for radiation pattern characterization. The following parts list the characteristic sets in

the calibration.

- Short-Open-Load-Through (SOLT) coaxial calibration.
- IF bandwidth: IF refers to Intermediate Frequency. The VNA allows the user to set the IF filter bandwidth. With a narrow IF bandwidth, the measurement noise floor is reduced, leading to a higher signal-to-noise ratio but longer calibration/measurement time. From the available choices 10 kHz, 1 kHz, 100 Hz, 10 Hz, we selected IF=100 Hz, the transmission noise level is under -80 dBm. This value is good enough to guarantee a good signal-to-noise ratio and not make the measurement last too long.
- The average is set to 64 during calibration. Then the VNA takes 64 sets of the measurement and average the results.
- The start frequency is 50 GHz and we make steps of 25 MHz till 65 GHz, thus covering the range of frequencies envisaged for our applications.

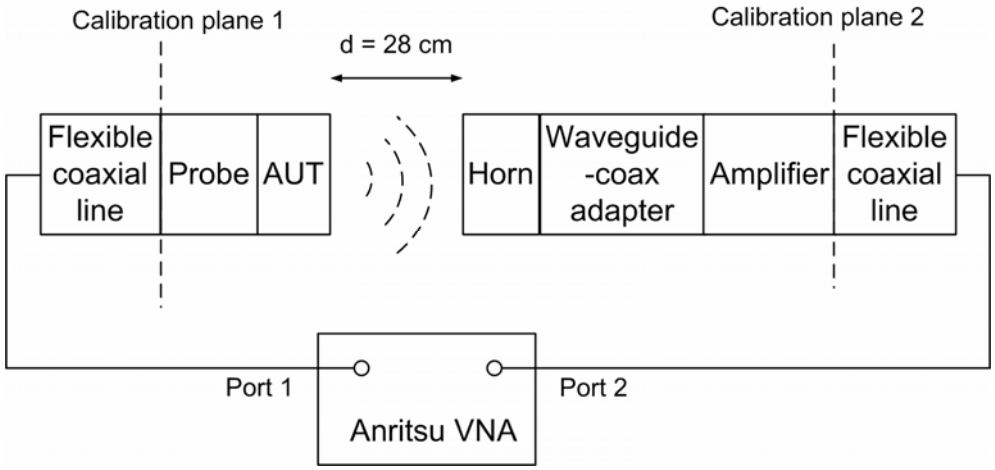

Figure 3. 12 Schematic of the measurement chain.

With the two customized probes just described, we expect larger measuring angles and less masking effects than with a standard probe. Therefore, in this section, we measured the radiation gain with these three different probes. After comparison with the theoretical values, we found that the customized probes meet our expectations. During these characterizations, two AUTs are used: the first one is the integrated spiral antenna on CMOS SOI and the second one is the integrated folded dipole antenna on high-resistivity silicon.

The AUT gain has to be extracted from the measured transmission coefficient by taking into account the transmission gain/loss of each component (horn, amplifier, RF probe, adapter) and the free space attenuation.

The radiation gain of the AUT was calculated by

$$G_{AUT} = S_{21} - G_{Horn} - G_{Amplifier} + L_{Probe} + L_{Adapter} - \left(\frac{\lambda^2}{(4\pi d)^2} \right)_{dB} \quad (4.1)$$

where S_{21} is the transmission coefficient measured by the VNA, G_{Horn}=19.5 dBi is the gain of the horn antenna, $G_{Amplifier}$=27.5 dB is the gain of the amplifier, L_{Probe}=0.77 and 2.41 dB are the standard and customized probes losses, $L_{Adapter}$=0.2 dB is the waveguide-to-coax adapter loss, λ=5.08 mm is the wavelength and d=28 cm is the distance between the AUT and the horn, all these numeric values are given at 59 GHz.

IV. Example 1: Measurement of the integrated spiral antenna

The emitting antenna is the AUT (Figure 3. 13), an integrated spiral antenna with low directivity. The test antenna is a 20 dBi horn antenna [20]. Figure 3. 14 shows a photograph of the measurement setup with probe feeding. As we can see in the photo, the horn antenna rotates behind the micro-positioner. This limits the measuring angle, and is known as the masking effect. A zoom-in view of the three probes feeding the integrated spiral antenna is presented in Figure 3. 15.

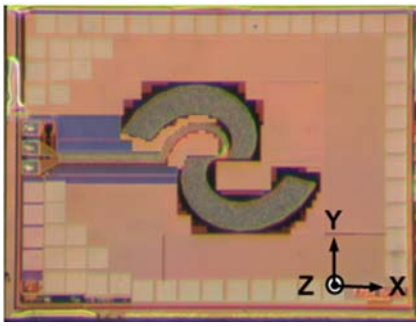

Figure 3. 13. Photograph of the AUT1.

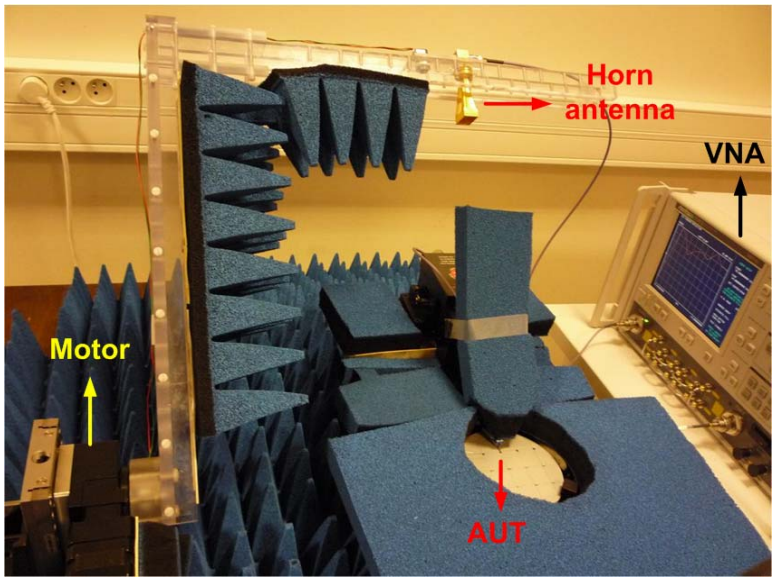

Figure 3. 14. Photograph of measurement setup.

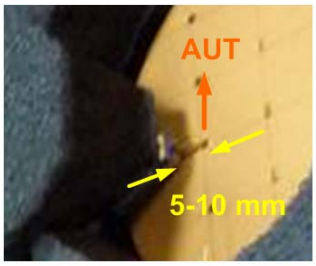

(a)

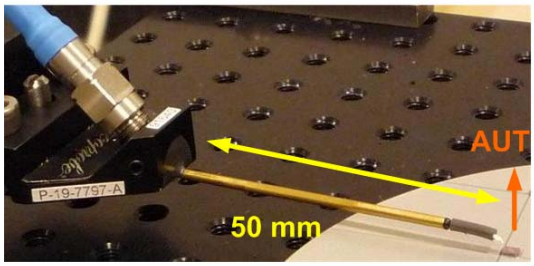

(b)

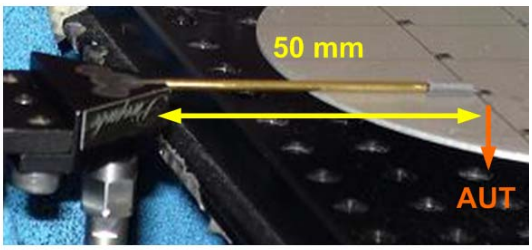

(c)

Figure 3. 15. Photograph of AUT fed by (a) standard probe; (b) probe with extension; (c) probe with extension and reversed connector.

Before presenting results with the three probe systems, we first discuss our method for setting up the system. In particular, it is important to ensure a good contact quality between the AUT and the probe, since a bad contact would cause an input impedance mismatch. For instance, a GSG probe operates with balanced ground currents, that is, the current flowing in the signal path is exactly double the current flowing in each of the ground paths. If one tip of G (ground) does not touch the pad, the probe will have an impedance of 100 ohms rather than 50 ohms.

To ensure a good contact, we use a microscope with a cold light while posing the probe tips on the chip's pads, the microscope is removed during the measurement. First we find a focused image of the pads and lower down the probe until the tips are very close to the attitude of the pads. Then we lower down the tips gently and pose them carefully on the pads, and we skate the tips forward/backward slightly to ensure a good "footprint" on the pads. The skating step is particularly important if the probe tips are not planar but rather are tilted or mounted at a certain angle, in which case the trace of the three tips (GSG tips for example) will not be symmetrical and they will not have the same scratch depth. The skating step is also important if the chip is inclined. In practice chips are frequently inclined because they are glued with conductive glue onto a metallic plate which serves as the ground plane, and because, in our setup, we do not have a wafer substrate to check the planarity of a chip. After an initial manual alignment the contact might not be sufficient. Therefore, we check the variation of the S parameters on the VNA, looking for sudden magnitude and phase variations of the return loss parameter. If there are no such variations, the skating step is repeated. Every time, when we posed the probe on the pads, this step should be checked before radiation pattern measurement.

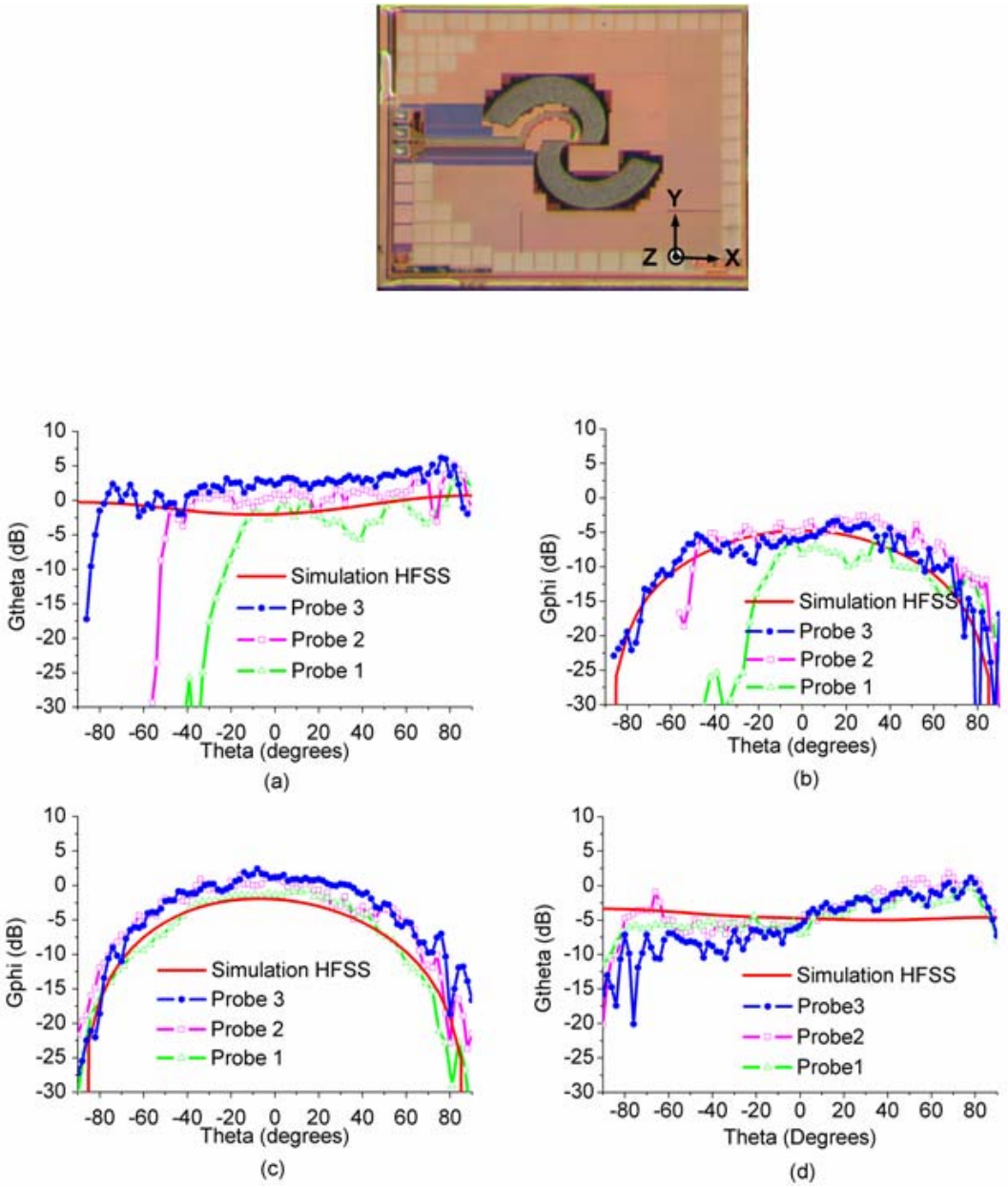

Figure 3. 16. Top figure: reminder of the AUT 1 with coordinate system, Bottom figures: gain radiation patterns simulated and measured with the three RF probes: (a) ZX plane co-polarization; (b) ZX plane cross-polarization; (c) YZ plane co-polarization; (d) YZ plane cross-polarization.

Figure 3. 16 shows the theoretical gain radiation pattern of the AUT in the ZX and YZ planes at 59 GHz measured with the three probes. Probe 1 is the standard infinity probe. Probe 2 is the customized probe with 50-mm coaxial extension and probe 3 is the customized probe with 50-mm coaxial extension and reversed connector.

We performed each measurement several times and no significant measurement dispersion was observed. Figure 9(a) and (b) in the ZX plane containing the RF probe clearly show the extension of the scanning zone, i.e. angular sector with valid measurements, obtained with the customized probes, and thereby the reduction of

the masked zone. Hence, the scanning zone extends approximately to [-10º, 90º], [-50º, 90º], and [-76º, 90º] with probe1, probe2, and probe3, respectively. Furthermore, smaller ripples and better agreement with the simulation results are obtained in the scanning zone with the customized probes. In the YZ plane, there is no masked zone, but the customized probes still managed to provide better measurement results in terms of ripple and gain level closer to the simulation.

In order to analyze quantitatively the differences between the simulation and the measurements obtained with each probe in terms of gain and ripples, we defined two figures of merit, namely the average gain error $\Delta\overline{G}$ and the root-mean-square ripple R_{rms}.

$\Delta\overline{G}$ is defined as the difference between the mean values of the measured gain $\mu(m) = \frac{1}{n}\sum_{i=1}^{n} m_i$ and the simulated gain $\mu(s) = \frac{1}{n}\sum_{i=1}^{n} s_i$, where m_i (resp. s_i) are the measured (resp. simulated) gain values in the scanning zone where valid measurements are expected:

$$\Delta\overline{G} = \mu(m) - \mu(s) \tag{4.2}$$

R_{rms} is defined as the root-mean-square difference between the measured and simulated gain after removing the average gain error:

$$R_{rms} = \sqrt{\frac{1}{n}\sum_{i=1}^{n}(m_i - s_i - \Delta\overline{G})^2} \tag{4.3}$$

Table 3.1 compares the performances of the three probes for the co- and cross-polarization in the two principal planes. The coaxial extension of probe 2 and 3 significantly reduces the masked zone in the ZX plane, and probe 3 provides a minimum masked zone smaller than 15° thanks to the reversed connector position. The average gain error $\Delta\overline{G}$ is higher with probe 2 and 3 than with probe 1; we believe that this error is likely due to the calibration procedure rather than the probe themselves and further investigations are required to clarify this discrepancy. The ripples R_{rms} are significantly reduced in the ZX plane thanks to the extension of probe 2 and 3, both for the co- and cross-polarization components, as expected. In the YZ plane, no significant difference is observed in the ripples obtained with the three probes as there is no obstacle in this measurement plane to trigger any masking effect, reflection or diffraction.

Table 3.1 Analysis of the measurement results of the AUT1 with the three probes.

	ZX plane (co-polarization)			**YZ plane** (co-polarization)			**ZX plane** (cross-polarization)			**YZ plane** (cross-polarization)		
Probe	1	2	3	1	2	3	1	2	3	1	2	3
Masked zone	~80°	~40°	<15°	NA	NA	NA	~80°	~40°	<15°	NA	NA	NA
$\Delta\overline{G}$ (dB)	−1.04	1.75	3.25	−0.13	2.69	3.33	-0.63	2.39	0.43	0.16	3.22	4.48
R_{rms} (dB)	1.9	1.44	1.59	1.88	1.48	1.87	3.11	2.57	1.76	2.37	3.07	4.4

V. Example 2: measurement of the integrated folded dipole antenna

The second AUT (Figure 3. 17) is an integrated folded dipole with a dimension of 5×3×0.88 mm^3.

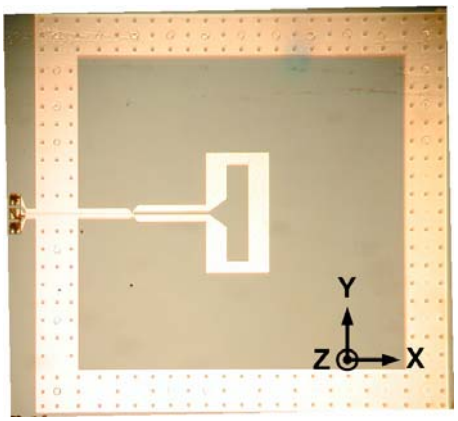

Figure 3. 17. Photograph of the AUT2.

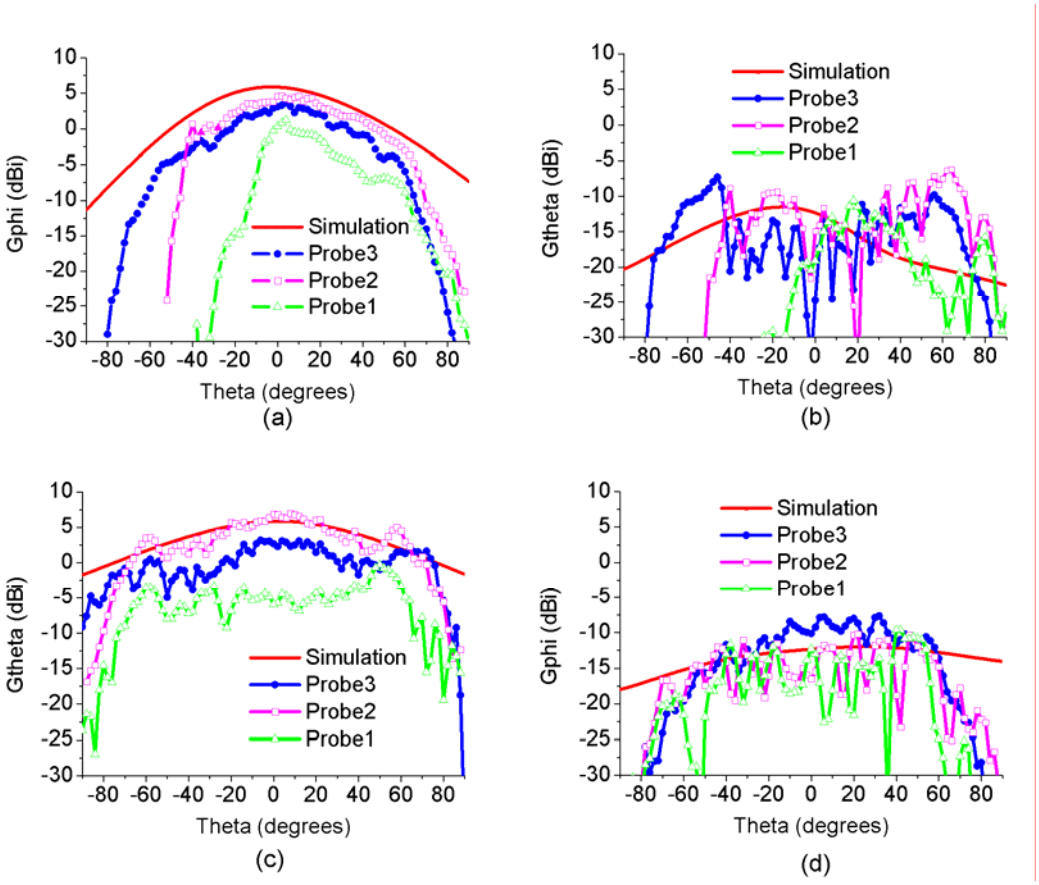

Figure 3. 18.Gain radiation patterns simulated and measured with the three RF probes: (a) ZX plane co- polarization; (b) ZX plane cross-polarization; (c) YZ plane co-polarization; (d) YZ plane cross-polarization.

Figure 3. 18 shows the theoretical gain radiation pattern of the AUT in the ZX and YZ planes at 60 GHz measured with the three probes. Probe 1 is the standard infinity probe. Probe 2 is the customized probe with 50-mm coaxial extension and probe 3 is the customized probe with 50-mm coaxial extension and reversed connector.

Figure 3. 18 (a) and (b) in the ZX plane containing the RF probe clearly show scanning zone of the three probes. i.e. angular sector with valid measurements, obtained with the customized probes, the extension of the measuring angles and thereby the reduction of the masked zone. Hence, the scanning zone extends approximately to [-5º, 70º], [-50º, 70º], and [-70º, 70º] with probe1, probe2, and probe3, respectively. In the figure, we can also observe that the gain decreases fast when the rotating arm is near the edge, it is due to the height of the absorbers, which is higher than the AUT and shield the radiation at certain angles. However in the scanning zone, smaller ripples and better agreement with the simulation results are obtained with the customized probes. In the YZ plane, there is no masked zone, but we can still observe the shielding effect of the absorbers near ±90° particularly for the cross-polarization.

The reason the shielding effect from the absorbers differs as we go from co- to cross-polarization is that the absorbers are not perfectly flat. But the customized probes still managed to provide better measurement results in terms of ripple and gain level closer to the simulation.

Table 3.2 Analysis of the measurement results of the AUT2 with the three probes.

	ZX plane (co-polarization)			**YZ plane** (co-polarization)			**ZX plane** (cross-polarization)			**YZ plane** (cross-polarization)		
Probe	1	2	3	1	2	3	1	2	3	1	2	3
Masked zone	~100°	~60°	<40°	~15°	~15°	~15°	~100°	~60°	<40°	~30°	~30°	~30°
$\Delta\overline{G}$ (dB)	−8.09	-2.48	-4.95	−8.97	-0.36	-3,44	-0.58	2.548	0.33	-6.29	-2.78	-0.05
R_{rms} (dB)	2.45	1.85	2.68	3.01	1.36	1.99	4.04	6.80	6.39	7.19	3.65	3.65

V.I Second test bench

In this chapter, we present the second test bench which is considered as an advanced version of the previous test bench. The integrated folded dipole antenna is characterized using both test benches, and we compare the performance of these two setups.

The bench is shown in the Figure 3. 19. The whole set up is located inside a full anechoic chamber of dimensions of 2.2×2.2×3 m^3. The absorbers cover every possible orientation around the AUTs to minimize reflections.

As in the first setup, this setup is fixed on a honeycomb board. It has two motors: one ensures the horizontal rotation of the AUTs and the other moves the rotating arm where the test antenna is fixed. To minimize interconnection losses in the whole transmission chain, two independent millimeter-wave modules of the VNA are positioned as close as possible to the two antennas. One millimeter-wave module (VNA 1) is connected to the AUTs through a semi-flexible coaxial cable of 20 cm. The AUTs plus the semi-rigid coaxial cable plus the probe system plus the VNA 1 are enclosed in a horizontal rotating box (Figure 3. 20). As we can see in the photo and the schematic of the second test bench, the horizontal rotating box is fully covered with absorbers. The other millimeter module (VNA 2) is connected to the test horn antenna through a waveguide bend. These items are fixed on the rotating arm which is shielded with the absorbers. The distance between the two antennas is around 50 cm.

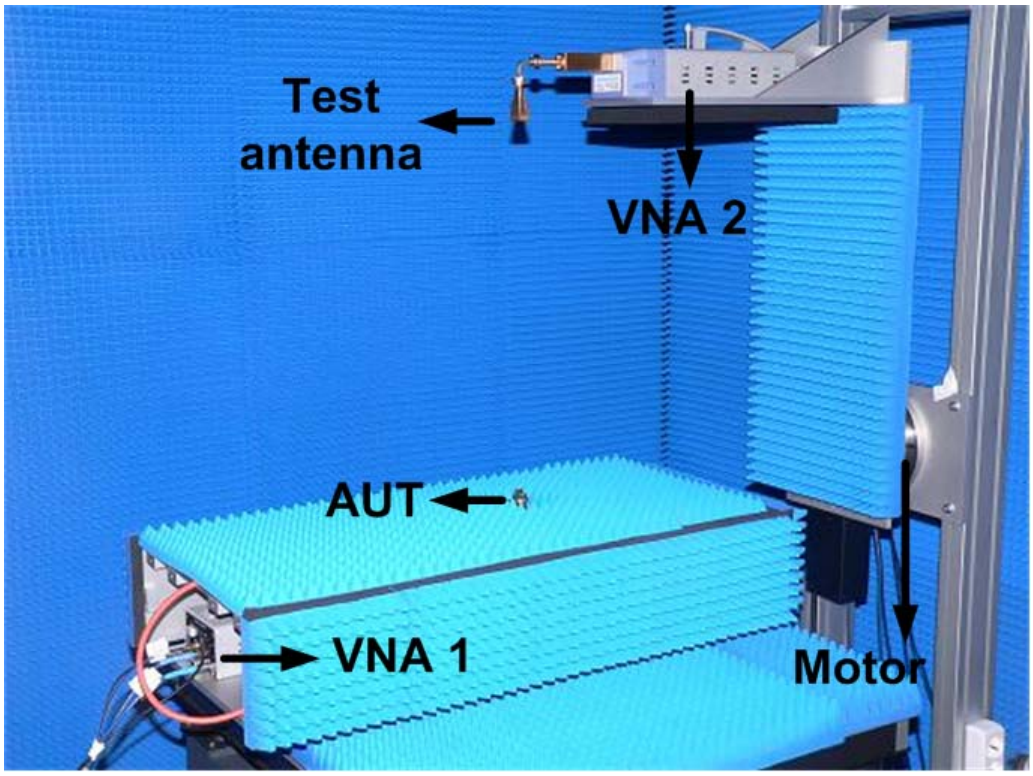

Figure 3. 19 Second test bench.

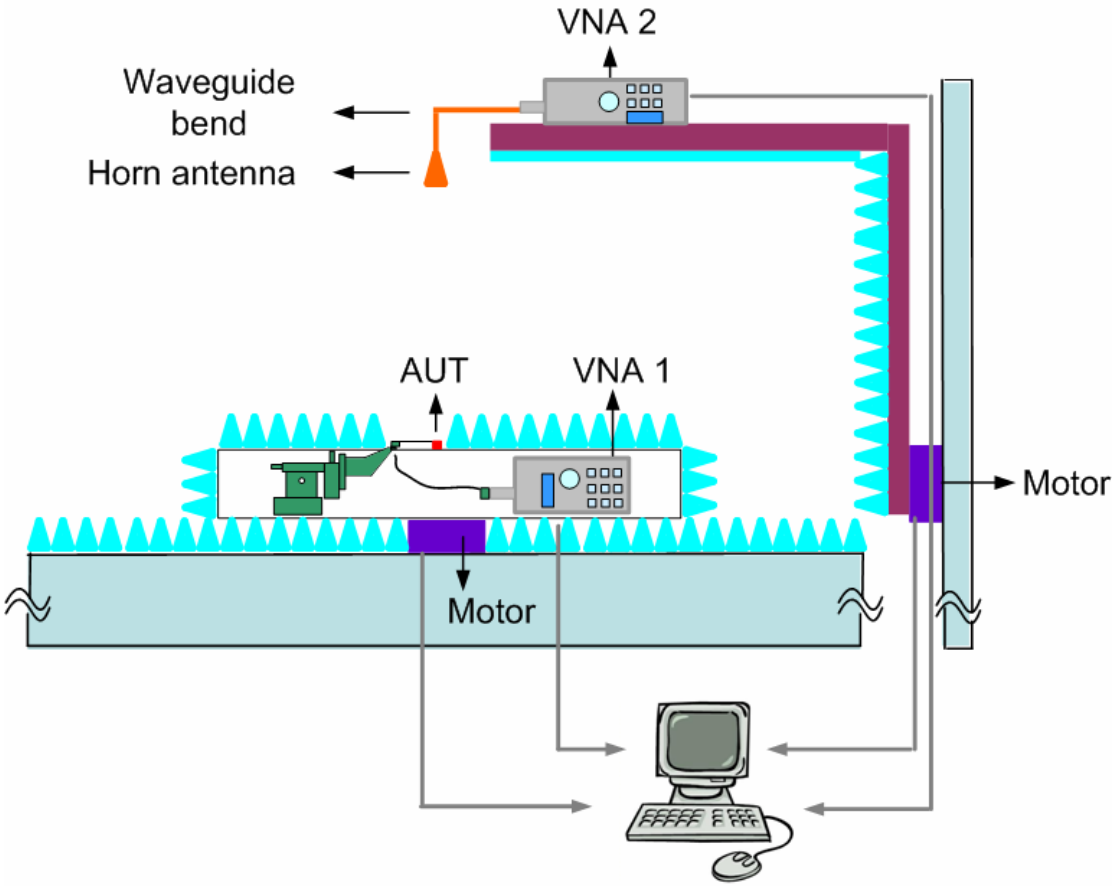

Figure 3. 20. Schematic of the second test bench.

- Calibration:
  - The two millimeter-wave modules are connected directly through V waveguides to get the reference of S21, which sets S21= 0 dB. Thus the calibration planes are set as shown in Figure 3. 21.
  - Then we use the formula (4.4) to extract the gain.

$$G_{AUT} = S_{21} - G_{Horn} + L_{Wg\_bend} + L_{Probe} + L_{Cable} + L_{Adapter} - \left(\frac{\lambda^2}{(4\pi d)^2} \right)_{dB} \quad (4.4)$$

In the formula 4.4, S_{21} represents the transmission coefficient measured by the VNA, G_{Horn} = 19.7 dBi is the gain of the horn antenna, L_{Wg_bend}, L_{Probe} L_{Cable} and $L_{Adapter}$ are the losses of the waveguide bend, the long reversed probe, the coaxial cable of the length is around 20 cm and waveguide-to-coax adapter respectively. L_{Wg_bend}=0.3 dB, L_{Probe} =2.41 dB, L_{Cable} =1 dB and $L_{Adapter}$ =0.2 dB. λ=5 mm is the wavelength and d=50 cm is the distance between the AUT and the horn, all these numeric values are given at 60GHz.

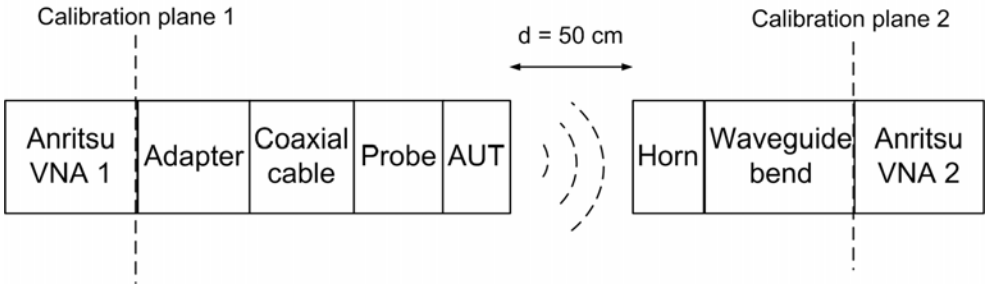

Figure 3. 21. Schematic of the measurement of second test bench.

- IF bandwidth: IF value is set to 1 kHz.
- The Average value is not set.

We compared the differences between these two test benches:

- Influence of the anechoic chamber: the first test bench is placed in the open air in a laboratory while the second test bench is enclosed in a full anechoic chamber. The anechoic room absorbers minimize the reflections from the ceiling and the walls.

- Influence of coaxial cables: the first test bench uses two semi-flexible coaxial cable of 90 cm. During the measurement, one coaxial cable moves with the rotating arm and the other remains still. The movement of the coaxial cable involves the difficulty of maintaining the same state of the cable. Movements of the cable cause substantial changes in the phase of the microwave signal [1, 21]. However, the amplitude of the signal does not vary substantially with the position of the cable, as long as there is not

a serious bend in the cable. The use of the rotating cable proves the limitation of the first test bench. In the second test bench, only low frequency (<12 GHz) coaxial cables are rotating (cables between the millimetre-wave modules and the VNA) and the phase stability of these cables are by far higher than the V-band cables of the first test bench.

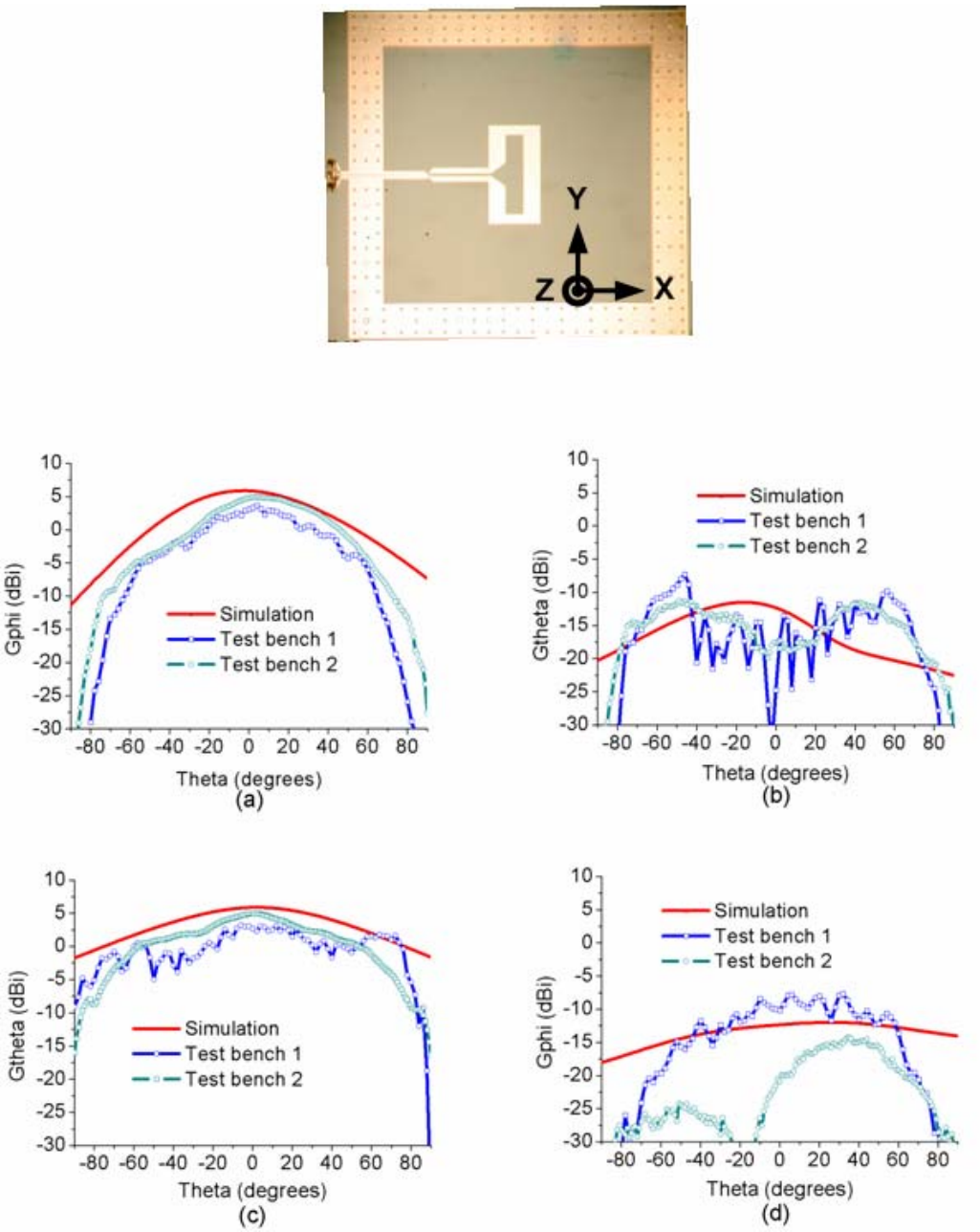

Figure 3. 22. Gain radiation patterns simulated and measured with the three RF probes: (a) ZX plane co- polarization; (b) ZX plane cross-polarization; (c) YZ plane co-polarization; (d) YZ plane cross-polarization.

Figure 3. 22 shows the theoretical gain radiation pattern of integrated dipole antenna in the ZX and YZ planes at 60 GHz measured with the long reversed probe using two

test benches. Test bench 1 refers to first test bench in the open air in the testing room. Test bench 2 refers to second test bench in the anechoic chamber.

As we can see for the co-polarizations (a) and (c), smaller ripples and better agreement with the simulation results are obtained with the second test bench. For the cross-polarization in the ZX plane (figure b), there are some differences between the theoretical and measured values, however the two measurements shape curves overlap quite well. With the second test bench, the strong ripples have been improved. In the (d), the second test bench has an unwanted negative peak of unknown origin.
In Table 3, we analyse the performance of these two test benches in three terms. The effects of performing the measurements in the anechoic chamber and the absence of the rotating coaxial cable at 60 GHz improve the accuracy of the characterization.

Table 3.3 Analysis of the measurement results of the AUT2 with the two test benches.

	ZX plane (co-polarization)		**YZ plane** (co-polarization)		**ZX plane** (cross-polarization)		**YZ plane** (cross-polarization)	
Probe	Bench 1	Bench 2	Bench 1	Bench 2	Bench 1	Bench 2	Bench 1	Bench 2
Masked zone	<40°	<20°	NA	NA	<40°	<20°	NA	NA
$\Delta\overline{G}$ (dB)	-4.95	-2.72	-3,44	-2.45	0.33	0.99	-0.05	-9.22
R_{rms} (dB)	2.68	1.83	1.99	1.12	6.39	4.76	3.65	5.26

VI Conclusion

In this chapter, we first present a new 3D characterization bench which was designed for the probe feed technique. This test bench is designed for low-directivity integrated antennas. Secondly, we present the standard probe's structure and its custom use for calibrating the gain of AUTs. As the main metal body of the probe is close to its tips, it triggers substantial masking effect. The probe body also causes substantial reflections. To overcome these limitations, we introduced two customized probes. These two customized probes are both air coplanar probes having a 50 mm coaxial extension between the probe tip and the main metal body. One has a regular connector which connects in the upward direction the other one has a reversed connector which connects in the downward direction. An integrated spiral antenna and an integrated folded dipole antenna are characterized by these three probes. We compare the performance of these three probes. The long reversed probe improves a lot the accuracy of the radiation pattern measurement, as the effective scanning zone

of the AUTs radiation pattern, the ripples of the curves as well as the gaps between the simulation and measured values. Then, we present the second test bench which we consider an advanced version of the first one with one additional motor, a more rigid rotating arm, the absence of moving millimeter-wave coax cable and a fully anechoic chamber. The performance of the second test bench improves in terms of ripples with a probe with extension and reversed connector. We concluded that these elements will influence the precision of the measurement.

References:

[1] A. Ungureanu, "Synthèse de sources rayonnantes large-bande par la méthode TLM Inverse," Ph,D thesis, Grenoble university, Grenoble, 2011.

[2] Photonlines corp. [online]. Available: http://www.photonlines.fr/

[3] Newmark systems [online]. Available: http://www.newmarksytems.com/

[4] Newport corp. [online]. Available: http://search.newport.com/i/1/q1/Products/q2/Manual+Positioners/q3/Manual+Linear+Stages/x1/pageType/x2/section/x3/chapter/nav/1

[5] M.D. Deshpande and C.J Reddy, "Application of FEM to estimate complex permittivity of dielectric material at microwave frequency using waveguide measurements," NASA technical report, ID 19960002474, 1995.

[6] Signatone [online]. Available: http://signatone.com

[7] Siepel [online]. Available: http://www.siepel.com/fr/siepel-france/siepel-france

[8] Anritsu [online]. Available: http://www.anritsu.com/en-GB/home.aspx

[9] Hxi [online]. Available: http://www.hxi.com/MMWProducts.asp

[10] Labview software [online]. Available: http://www.ni.com/labview/

[11] E.M. Godshalk, J. Burr, and J. Williams, "An Air Coplanar Wafer Probe," *ARFTG Conference Digest-Spring, 43rd*, pp. 70-75.

[12] S. Wartenberg, "RF Coplanar Probe Basics," *Microwave Journal*, vol. 46, no. 3, 2003.

[13] S.A. Wartenberg, "Selected topics in RF coplanar probing," *Microwave Theory and Techniques, IEEE Transactions on*, vol. 51, no. 4, 2003, pp. 1413-1421.

[14] E.M. Godshalk, "A V-band wafer probe using ridge-trough waveguide," *Microwave Theory and Techniques, IEEE Transactions on*, vol. 39, no. 12, 1991, pp. 2218-2228.

[15] A.M.E. Safwat, "Study of microstrip mode in RF on-wafer probes," *Microwave and Optical Technology Letters*, vol. 45, no. 4, 2005, pp. 324-328.

[16] GGB [online]. Available: http://www.ggb.com

[17] Cascade Microtech [online]. Available: http://www.cmicro.com.

[18] L.F. Samoska, A..Fung, D. Pukala, P. Kangaslahti, R. Lai, S. Sarkozy, X.B. Mei and G. Boll, "On-wafer measurements of S-MMIC amplifiers from 400–500 GHz," Microwave Symposium Digest (MTT), IEEE MTT-S International, 2011 pp. 1 – 4.

[19] K. Mohammadpour-Aghdam, S. Brebels, A. Enayati, R. Faraji-Dana, G.A.E. Vandenbosch, and W. DeRaedt, "RF probe influence study in millimeter-wave antenna pattern measurements," *International Journal of RF and Microwave Computer-Aided Engineering*, 2011.

[20] Q-par Angus Ltd [online]. Available: http://www.q-par.com/

[21] S. A. Wartenberg, “RF Measurements of Die and Packages,” Boston,MA: Artech House, 2002.

Chapter IV
Characterization of integrated antennas at millimeter-wave frequencies with a flexible line

I Introduction

In this chapter, we are going to present another direct method of characterizing the AUT's radiation patterns using the same test bench as in Chapter III. As we learned in Chapter III, with characterization under customized probes, we significantly increased the measuring zone and decreased the ripples on the radiation pattern compared with using standard probes. However the masking effect still persists. As our first aim is to measure AUTs with low directivity, it remains important to achieve a larger scanning zone. Furthermore, the use of the probe-fed technique described in the previous chapter required a large but delicate micro-positioner and a microscope. In this chapter, we shall design a feeding technique that does not require these large items, and thus results in an apparatus that is more portable and is easier to install in an anechoic chamber.

Here we introduce a feeding technique based on a flexible transmission line. The initial idea of having a flexible transmission line was to make all the measuring apparatus lie under the antenna's ground plane. As shown in Figure 4. 1, an AUT is placed on a fixture and a flexible transmission line (t-line) makes the connections between the AUT and the instruments. Only a small part of the t-line is in the air above the ground plane and the rest of it is hidden under the fixture with the connector.

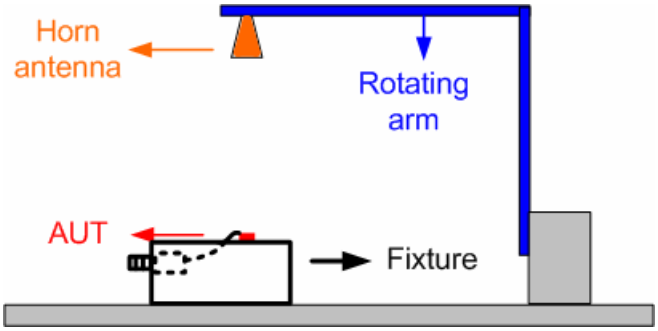

Figure 4. 1 Test bench with the flexible transmission line set-up.

II Choice of the substrate material

To implement this concept, the following criteria are important in the search for flexible electronic materials:

- light weight

  As the connection between the chip and the transmission line is very delicate. The contact surface is less than 86×70 μm^2 for each pad, yet the connection should support the line's weight.

- flexible

  The line must bend in order to connect to the AUT in the upper hemi-sphere (scanning zone) and the V-connector in the lower hemi-sphere. A very flexible material is required in order for the tiny connection surfaces mentioned above to handle the substrate shape restoring force.

- thin

  The end of the transmission line connected to the AUT will be above the AUT's plane. Therefore, to minimize unwanted reflections, the substrate should be thin and low profile.

- electrical and physical properties

  The substrate should be resistant to heat and to chemicals used in the production process. In particular, it should handle the metal deposition and etching processes. At millimeter-wave frequencies, transmission lines are associated with high losses. Therefore, it is important to choose a substrate with low permittivity and low loss tangent to minimize these losses.

In today's electronics world, flexible circuits are widely used. Their applications

include: flat-panel displays, keyboards, radio-frequency identification tags which are becoming as prolific as bar codes, sensors which can simulate the human skin, detectors built into clothes, flexible solar panels which can bend to follow the sun, internal connections and flexible display, such as LG Philips' flexible E-Book in 2006, Samsung's liquid crystal display panel and organic light-emitting diode display with full-color and full-motion presented by Universal Display Corporation and PARC [1-5]. Flexible circuits are often used for the purpose of product miniaturization, or for instance so that the shape may be stuck on an arbitrarily-shaped surface. In the flexible electronics industry, several flexible plastic substrates such as polyimide (PI), polyethylene terephthalate (PET), polyethylene naphthalate (PEN), polycarbonate (PC), polyethersulfone (PES) [2]. Among these substrates, polyimide is widely used as it is light, flexible and resistant to heat and chemicals. Kapton [6], one of the PI developed by DuPont seems to be a good candidate. It is widely used in transmission lines at lower frequencies and has existing mature fabrication and manipulation techniques. However the fabrication of the millimeter-wave circuits on the flexible substrate is very challenging. A microstrip patch antenna was fabricated on Kapton around 18 GHz in [7] and 14 GHz on LCP in [8]. Very recently, in 2009, reference [9] reported a 60 GHz patch antenna fabricated on the polydimethylsiloxane (PDMS). However, as Kapton is very commonly processed in the industry (even in the outsourcing companies), we decided to use this substrate to have a first test. The following table lists several of Kapton's physical and electrical properties.

Table 4. 1. Typical properties of Kapton film for several thicknesses [6].

	Unit	**25 μm**	**50 μm**	**75 μm**	**125 μm**
Physical					
Tensile strength	MPa	234	234	234	234
Elongation	%	80	82	82	82
Density	g/cc	1.42	1.42	1.42	1.42
Tear-propagation strength (Elmendorf), N		0.07	0.21	0.38	0.51
Initial tear strength (Graves), N		7.2	16.3	26.3	46.9
Electrical					
Dielectric strength	kV/mm	303	240	205	154

Dielectric constant	1 kHz	3.4	3.4	3.5	3.5
Dissipation factor at 1 kHz	1 kHz	0.0018	0.0020	0.0020	0.0026

There exist Kapton films with four thicknesses, which meet all of our requirements. We chose a standard substrate with a thickness of 50 μm and a metal deposition thickness of 18 μm to make a transmission line.

As we are working with RF applications, the skin depth should be taken into consideration. Skin effect is the tendency of an alternating electric current (AC) to distribute itself within a conductor. For AC, the current density is largest near the surface of the conductor and decreasing at greater depths, whereas direct current (DC) is distributed evenly across the cross section of the wire. The skin depth is defined as the following (5.1):

$$\delta = \sqrt{\frac{2\rho}{\omega\mu}} \tag{5.1}$$

where

δ is the skin depth in m

ρ is the resistivity of the conductor in Ω·m

ω is the angular frequency of current, $\omega = 2\pi f$

μ is the absolute magnetic permeability of the conductor.

So the higher the conductivity and the higher the frequency, the thinner the skin depth will be. We should choose the thickness of the metal layer larger than the skin depth to ensure low resistive losses. Over 98% of the current will flow within a layer 4 times the skin depth from the surface. So we should make sure that the thickness of the metal is at least 4δ = 4×0.266 μm for copper at the 60 GHz band according to equation 5.1. Therefore we finally chose a 50 μm thickness of Kapton and a 18 μm thickness for the coated copper layer as our substrate to form the t-line.

III Design of the fixture

The fixture should firstly serve as a support for the AUT, the transmission line and the V-connector. Secondly the surface of the fixture should be smooth as it serves as a

ground plane for the AUTs. Thirdly it should have an opening to let the transmission line pass through.

A 5.5×4.5×1.8 cm^3 metal bracket is designed as shown in Figure 4. 2. It is made of aluminum and can be easily screwed or unscrewed on the test chuck. In the middle of the bracket, there is a hole which is designed for the transmission line to pass through. The transmission line makes the connection between the AUT and the V-connector. To minimize unwanted perturbations from the transmission line, the AUT is glued next to the hole, so there will be only 2-3 mm of the line in the upper hemisphere and the rest is hidden in the bracket.

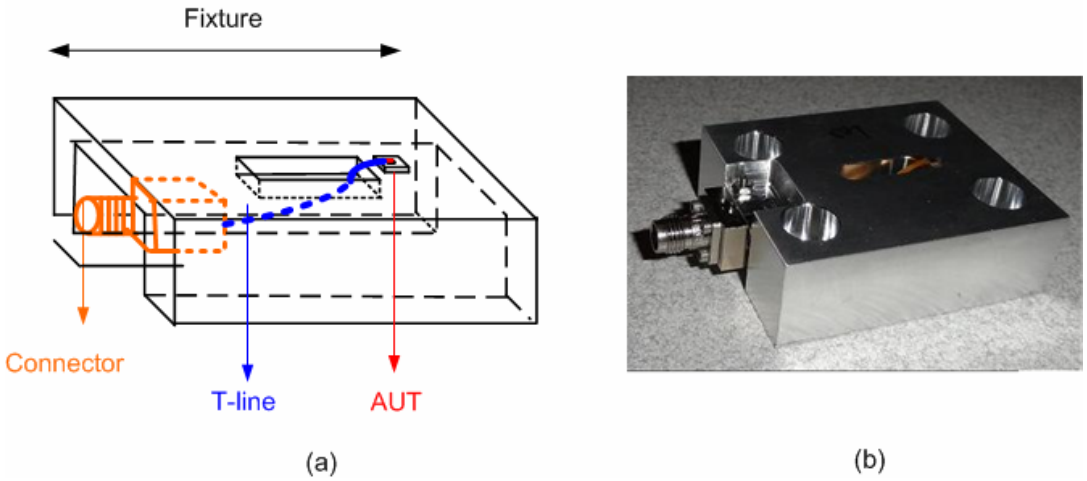

Figure 4. 2 (a) Design (b) and photo of the fixture with the AUT.

IV Design of the transmission line

In this section, we consider two types of transmission line: a CPW (Coplanar waveguide) line, and a microstrip line. We assess the design by simulations using the software Agilent Advanced Design System Momentum [10]. The simulation was divided into three parts: the main transmission line, the transition to the chip and the transition to the connector.

IV.I Main transmission line

We propose two types of transmission line: microstrip and CPW line. As the final t-line will be up to 4 cm long, we simulate sample lines of length 1 cm to save simulation time.

- A microstrip line is shown in Figure 4. 3. l_2 and W_2 are the length and the width of the strip line. In order to match the characteristic impedance of the AUT to 50 Ω, we chose l_2= 1 cm, W_2= 120 µm. Figure 4. 4 shows the corresponding simulated S parameters. The reflection coefficient is under -35 dB for frequencies from 1 to 100 GHz and the transmission coefficient is in the range -0.7 to -0.9 dB for frequencies from 50 to 70 GHz. The guided wavelength is λ_g = 2.95 mm at 60 GHz and the effective permittivity is ε_{r_eff} = 2.874.

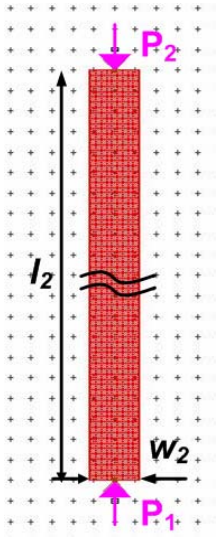

Figure 4. 3 Main line: Microstrip line.

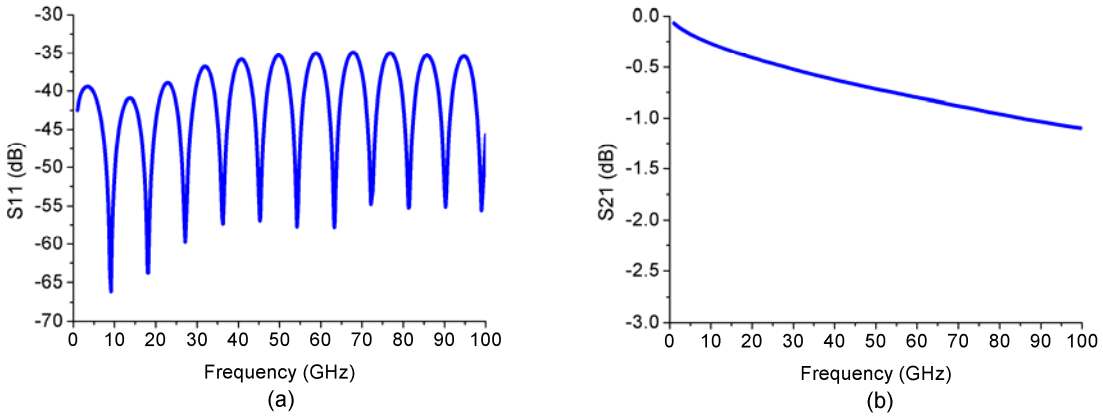

Figure 4. 4 Simulated S parameters of microstrip line.

- The design of a CPW line is shown in Figure 4. 5. l_2', W_2' represent the length and the width of the signal line and S_2' represents the width of the slot. We chose a narrow slot since the substrate has a low permittivity and we wish to

achieve a characteristic impedance of 50 Ω. The following values: l_2=1 cm, W_2= 120 µm , S_2'= 11 µm, lead to a good match to 50 Ω. The simulated S parameters are shown in Figure 4. 6. The effective permittivity is ε_{r_eff} = 1.8.

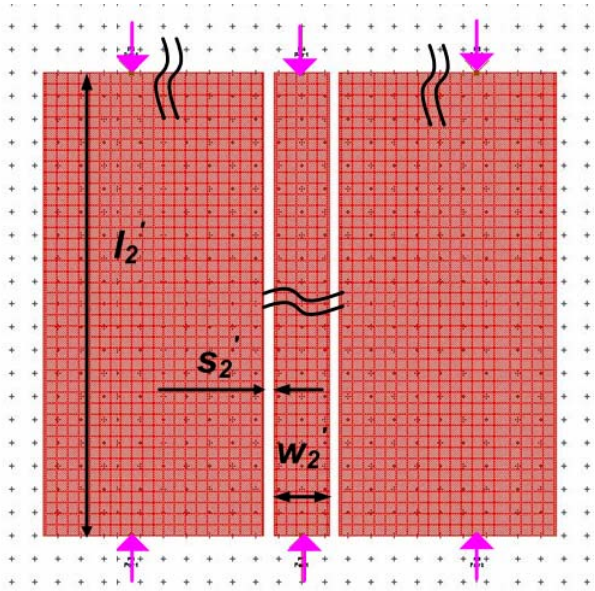

Figure 4. 5 Main line: CPW line.

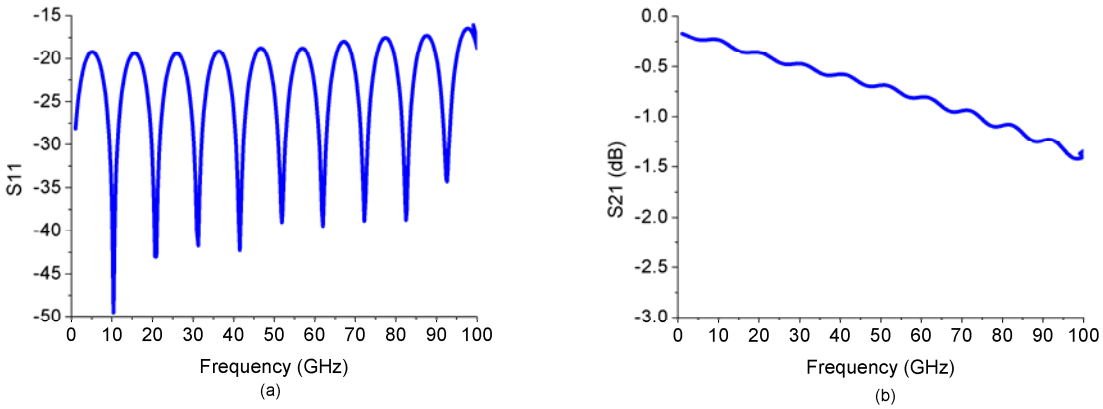

Figure 4. 6 Simulated S parameters of CPW line.

As we can see for the CPW, the width of the slot is inferior to 50 µm, It is quite thin due to the low permittivity of the Kapton substrate. Indeed, it is not possible to fabricate such a slot with common etching techniques on flexible substrates, which have a minimum resolution of 50 µm [11-13]. If the slot width was increased to 50 µm, the central conductor width would need to be increased to several hundreds of microns, resulting in a very wide transmission line compared to the wavelength.

Instead, a microstrip line is easier to fabricate and it has low parasitic radiation compared with a CPW. Therefore, the microstrip line is finally chosen as the main

transmission line.

The following sections will present the transitions to adapt the connection with other apparatus.

IV.II 2.40 mm-connector end design

We used an end launch 2.40 mm coaxial connector [14]. It is a transition between a 2.40 mm-connector and a test fixture designed for printed circuit boards, as shown in Figure 4. 7.

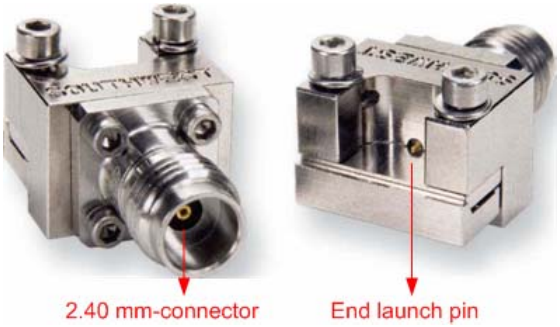

Figure 4. 7 Front view and back view of the 2.40 mm-connector [14].

This connector is suitable for characterizing the S parameters of a single-layer or multi-layer printed circuit board where the microwave layer is on top. By design, it can adapt two types of circuit board: one is grounded coplanar and the other is a microstrip line with a top-grounded launch. As our t-line is a microstrip line, one end of the t-line is designed with its top grounded. Figure 4. 8 shows a zoom on the contact pad.

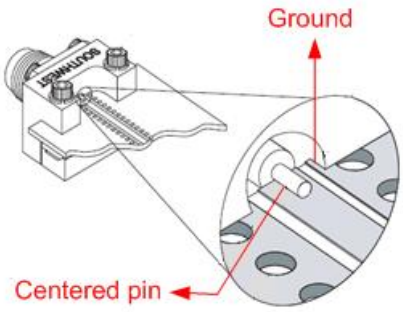

Figure 4. 8 Zoom on the contact pad.

The 2.40 mm-connector is designed to operate up to 50 GHz. However we found that

we were able to use it here as it has been tested with acceptable performances up to 60 GHz: as shown in Figure 4. 9, S parameters of two 2.40 mm-connectors connected to a microstrip line with its top grounded. The t-line is fabricated on a Rogers substrate. As we can see, the reflection coefficient is under -8 dB up to 60 GHz.

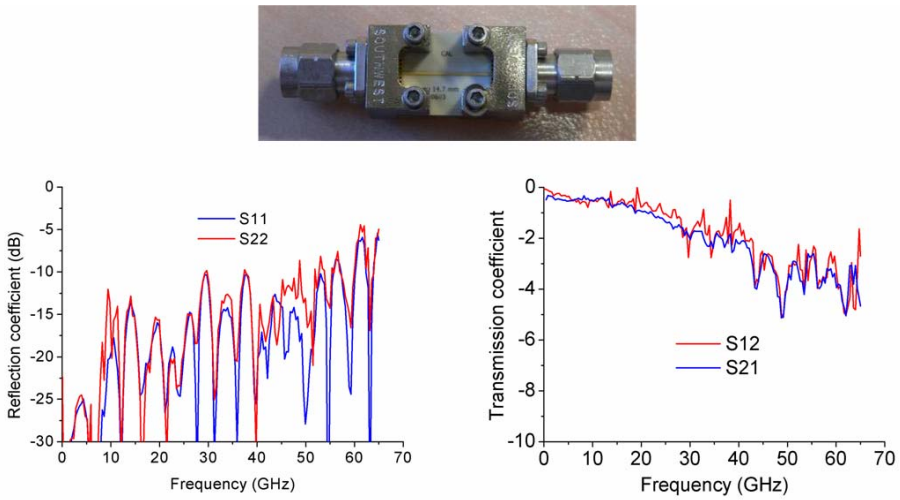

Figure 4. 9 Measured S-parameters of a microstrip transmission line with two 2.40 mm-connectors.

The design of the connector-to-microstrip transition requires a trade-off between impedance matching (the V-connector is designed for 50 Ω impedance up to 50 GHz but we are using it for 60 GHz) and the risk of a short circuit. For example, the line should be larger than the protruding launch pin and the two top grounded planes should be kept a certain distance from the line in order to not get short-circuited. Yet in such a design, the t-line is not impedance matched locally.

In the simulation (Figure 4. 10):

- S_1 = 180 µm is the gap between the centre line and the top-grounded plane
- l_{g1} = 500 µm and w_{g1} = 1000 µm are the length and the width of the top grounded plane respectively,
- l_1 = 1 cm and w_1 = 120 µm are the length and the width of the centre line respectively.

The purple circles represent via holes which directly connect the top ground planes to the bottom ground plane to avoid unwanted resonances. The diameter of the via holes Φ is 100 µm, and the distance d between any two adjacent via holes is 200 µm (from centre to centre) which is the minimum distance required by the fabrication technology [11-13]. The pink arrows represent the simulation ports' positions.

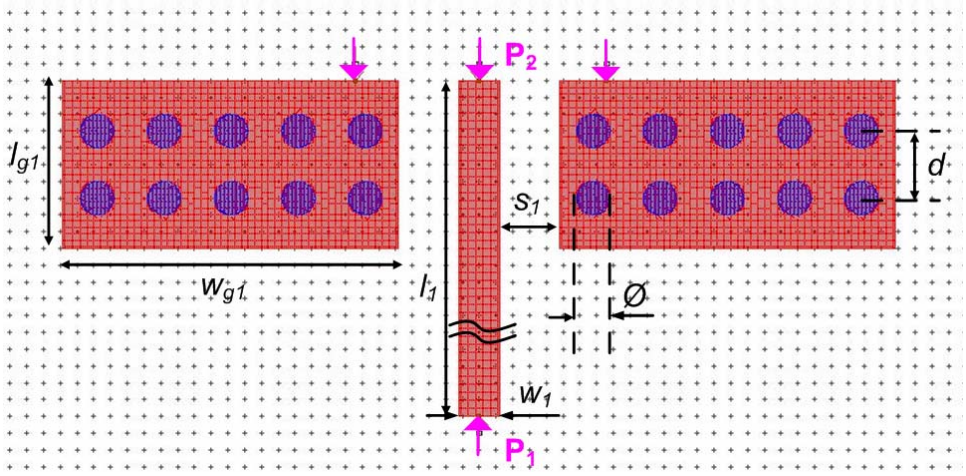

Figure 4. 10 Simulation model of the V-connector.

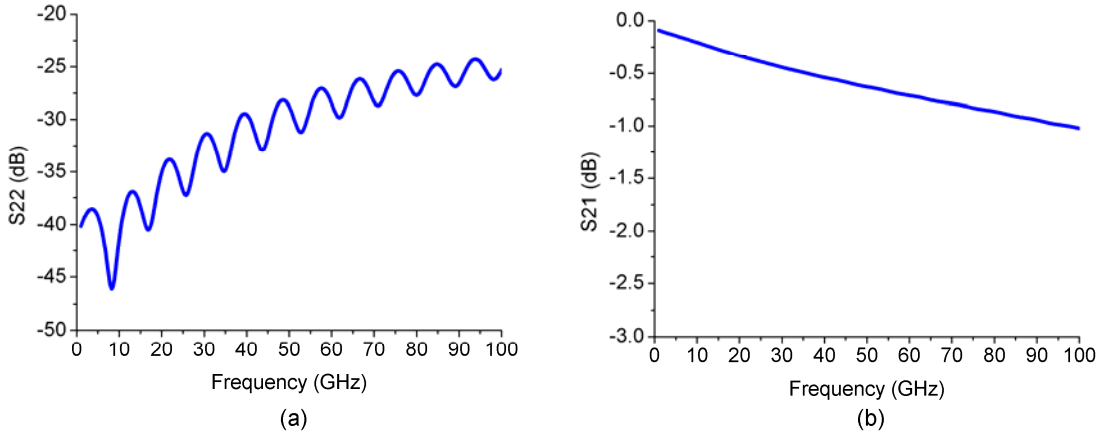

Figure 4. 11 Simulation results of the connector to microstrip transition.

Figure 4. 11 shows the S parameters of the connector to microstrip transition. The reflection coefficient is under -20 dB for the frequencies between 1 to 100 GHz. and the transmission coefficient is between -0.6 to -0.8 dB for frequencies between 50 and 70 GHz.

IV.III GSG pads end

The chip is designed to be tested under probes, therefore it is designed with GSG contact pads with dimensions of 86×70 μm^2 for each pad and a pitch of 100 μm. To make a flip chip connection with GSG contact pads on the chip, this t-line requires a microstrip to coplanar CPW transition (Figure 4. 12). As the integrated spiral antenna is wide band (50-85 GHz for S11 inferior to -10 dB), the transition should also have a

wide bandwidth, at least it should have a bandwidth larger than the antenna's bandwidth. Therefore, radial quarter-wavelength stubs were chosen to obtain a wideband RF ground at each ground pad [15].

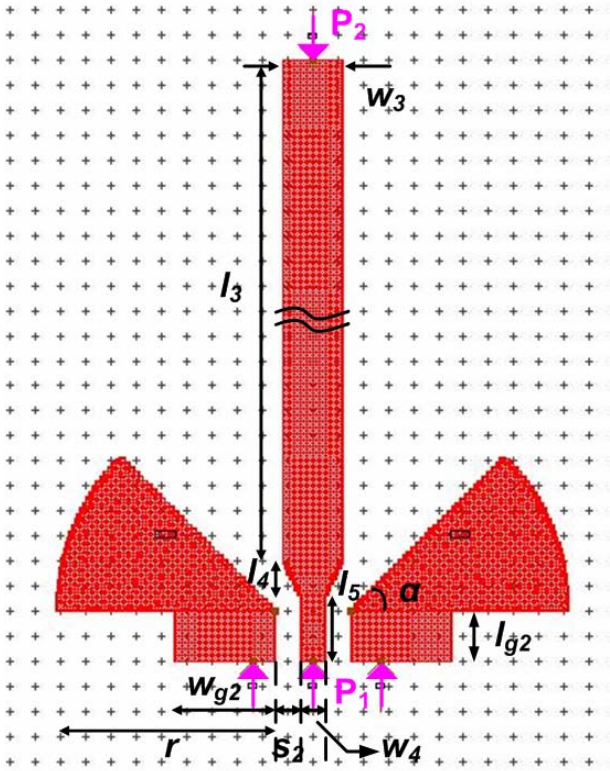

Figure 4. 12 Simulation model of the GSG pads end.

The limitation of the etching technology on the flexible substrate is a minimum line width and slot width of 50 µm [14]. So, we set following values for the model.

- w_3= 120 µm; w_4= 50 µm;
- s_2= 50 µm;
- l_3= 1000 µm; l_4= 70 µm; l_5= 130 µm;
- l_{g2}= 100 µm; w_{g2}= 200 µm;
- α= 45°;
- r = 435 µm.

This end is well matched for frequencies between 50 to 84 GHz and as S11 is under -20 dB in this band, it covers our frequencies of interest. S21 is between -0.6 and -0.9 dB in the range 50–70 GHz (Figure 4. 13).

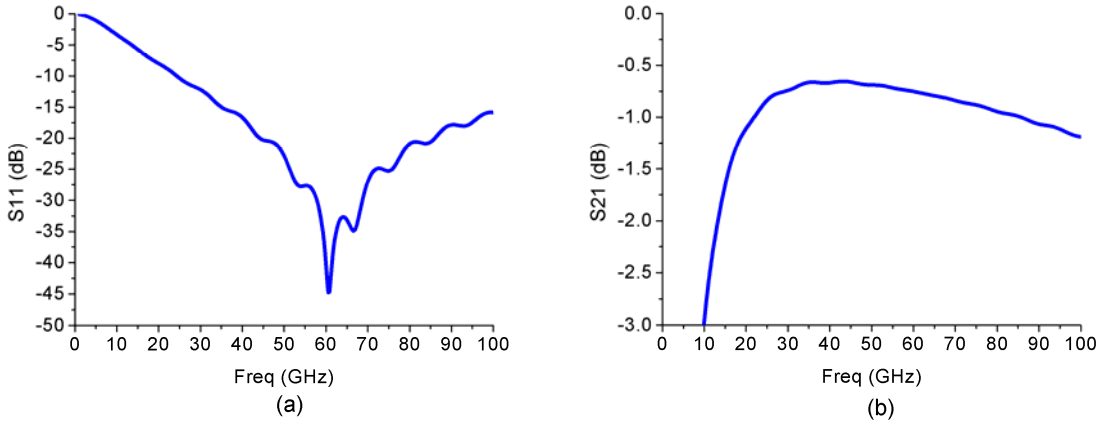

Figure 4. 13 Simulation results for the GSG pads end.

In this section, we presented the design of the t-line in three parts with simulations performed under Agilent-Momentum. The characterization of the t-line will be presented in the next section.

V Characterization of the flexible transmission line

The flexible transmission line has been designed and fabricated (Figure 4. 14). Two extra holes were made for the screws of the end-launch connector. To extract the S parameters of the transmission line, we used the measurement set-up shown in Figure 4. 15.

We placed the flexible t-line on the bracket. One end of the transmission line is connected with a standard RF probe (GSG, 100μm pitch) and the other end is connected to the 2.40 mm-connector. We used a two ports SOLT calibration (Figure 4. 16). The two reference planes are at the input of the RF probe and the output of the 2.40 mm-connector respectively.

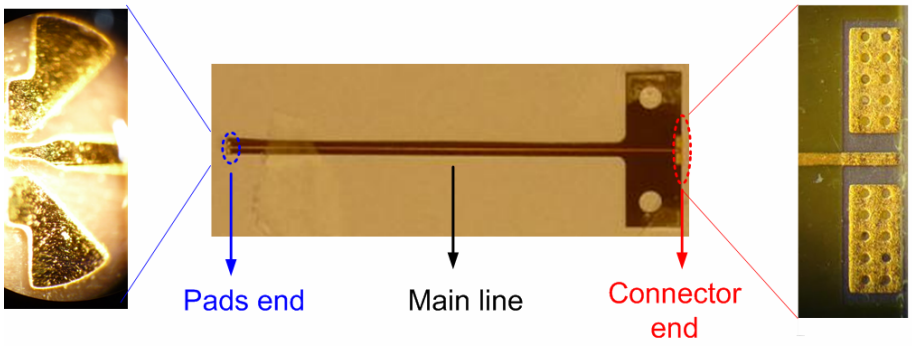

Figure 4. 14 Kapton transmission line with zoom in of the pads end (left) and zoom in of the connector end (right).

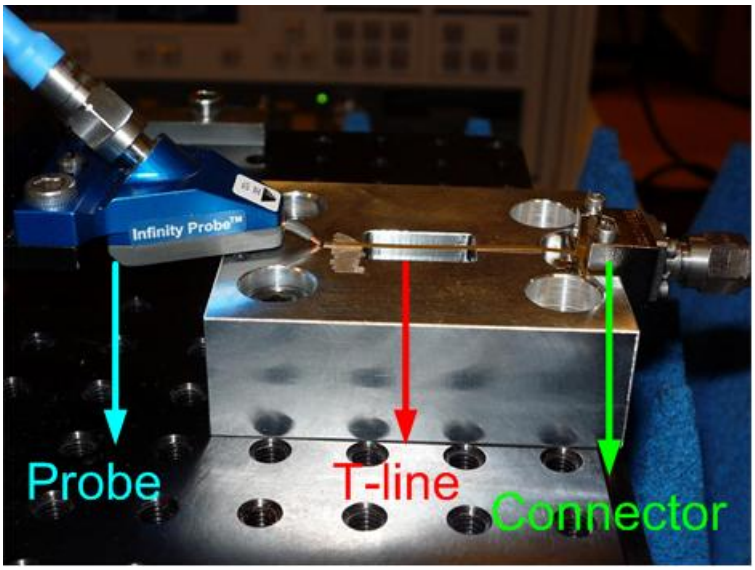

Figure 4. 15 Photo of the test bench.

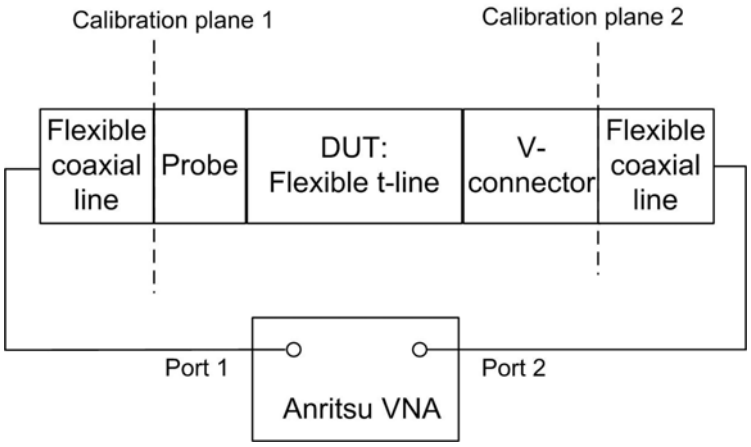

Figure 4. 16 Schematic of the measurement chain.

Figure 4. 17 shows the reflection coefficient of the t-line with 2.40 mm-connector (de-embedding the effect of the probe). The GSG pads end is better adapted than the

connector end. After de-embedding the effects of the probe and the connector, we compared the simulated and the measured transmission coefficients, which are shown in Figure 4. 18. In this simulation, the substrate loss tangent and metal conductivity were set to tan δ = 0.009 and σ = 40×10^6 S/m to better match the measurements. Indeed, a 3 dB difference in transmission losses is observed when using the manufacturer's specified Kapton loss tangent at 1 kHz and default copper conductivity: the manufacturer did not specify these quantities for 60 GHz. This issue is further investigated in the next two paragraphs.

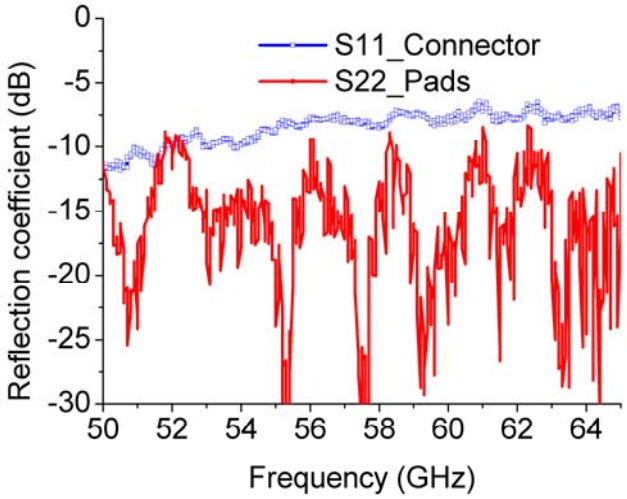

Figure 4. 17 Measured reflection coefficient of t-line with connector.

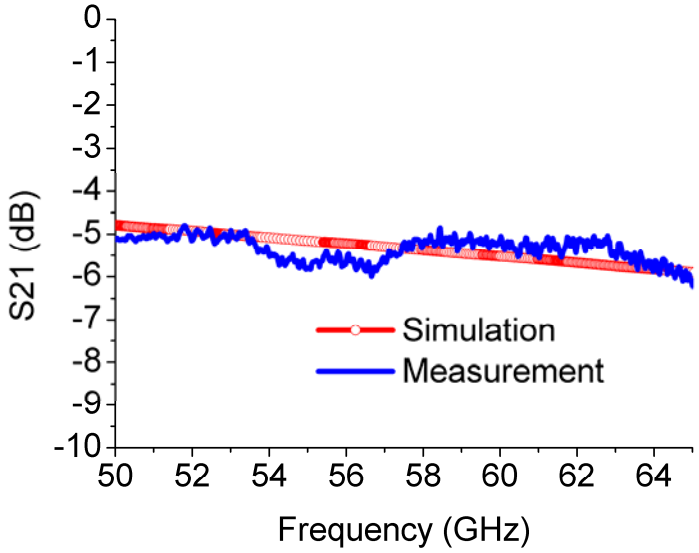

Figure 4. 18 Comparison of the simulated and measured transmission coefficient.

V.I Influence of the substrate's loss tangent on the transmission line performances

Here, we vary the loss tangent of the Kapton around its default value (tan δ = 0.0018) which is given in the datasheet for 1 kHz [6]. In general, the loss tangent of a dielectric substrate increases with the frequency [16, 17]. The transmission coefficient is simulated for these varying loss tangent values (Figure 4. 19). The transmission losses increase significantly with tan δ, whereas the loss tangent variation has no significant impact on the reflection coefficient (Figure 4. 20).

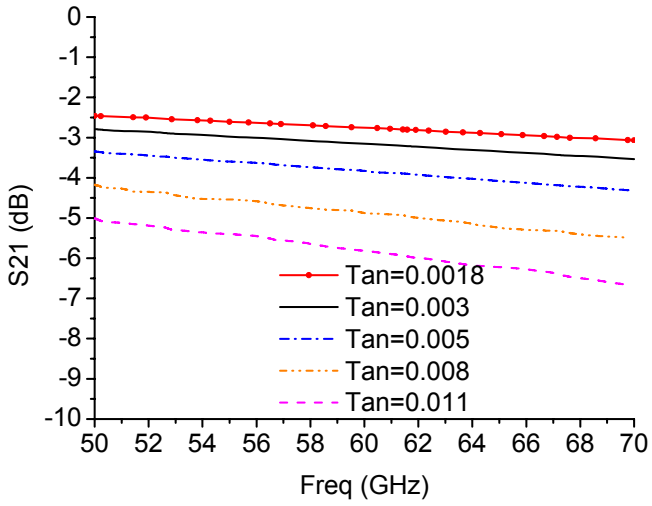

Figure 4. 19 The influence of the loss tangent on the t-line on the transmission coefficient.

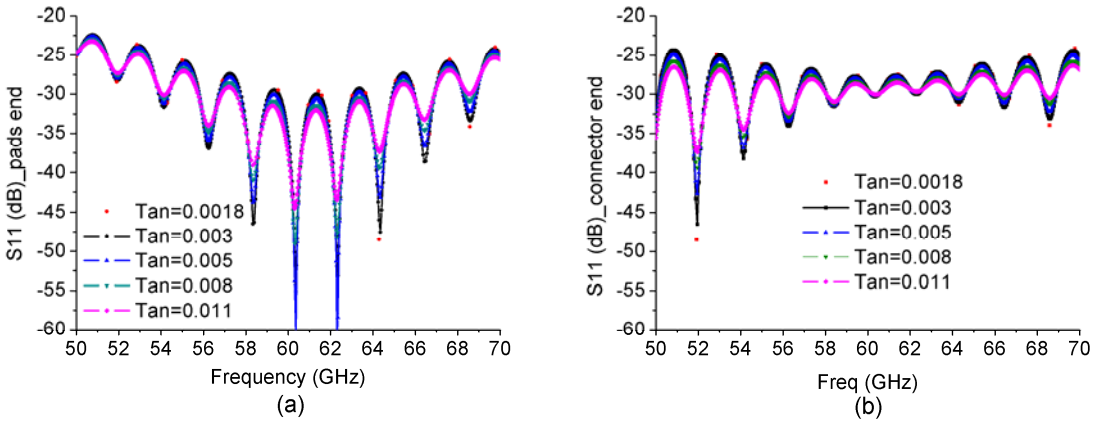

Figure 4. 20 The influence of the loss tangent on the reflection coefficient of the t-line.

V.II Influence of copper's conductivity on the transmission line

In our design, all the metal traces are made of a copper base. As copper is easily eroded by acids and oxidized by the air, the whole t-line should be covered by a protective layer. In our design, the two ends of the t-line are coated with a layer of nickel (1.45×10^7 S/m) and gold (4.1×10^7 S/m) in order to protect the copper and simultaneously maintain good conductive contact. Other parts of the t-line are coated with a layer of varnish to prevent oxidation of the copper. Therefore, the equivalent conductivity of the metal needs to be adjusted to an effective value close to reality for accurate simulations. Figure 4. 21 shows the simulated transmission coefficient for several conductivity values.

Again, the conductivity variation has no significant impact on the reflection coefficient (Figure 4. 22).

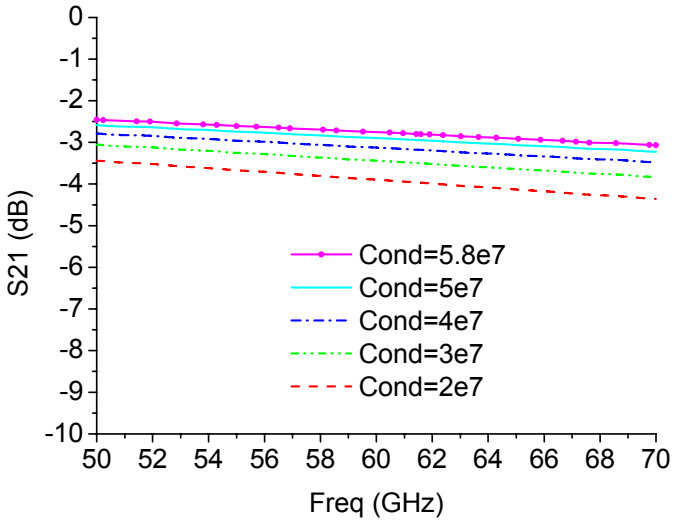

Figure 4. 21 The influence of the conductivity (measured in S/m) on the transmission coefficient of the t-line.

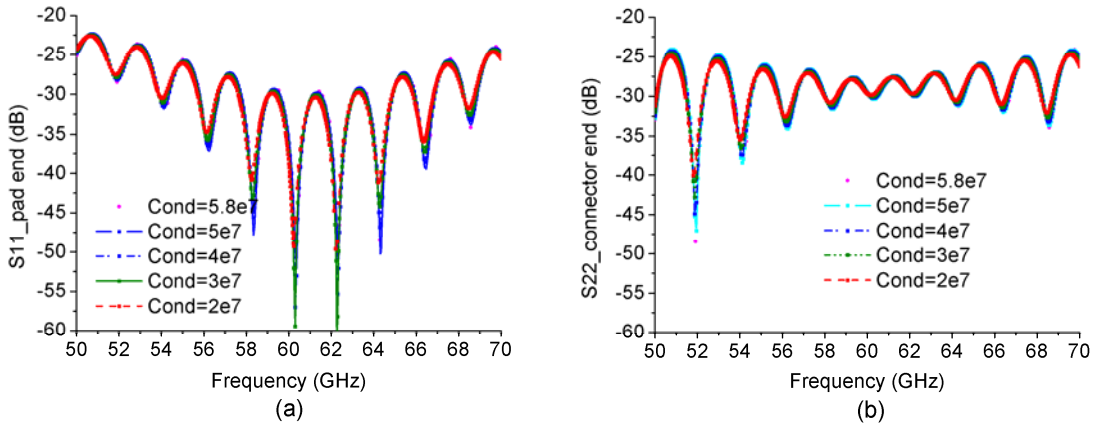

Figure 4. 22 The influence of the conductivity (measured in S/m) on the reflection coefficient of

the t-line.

In this section, we presented the characterization of the flexible t-line and compared the simulated and measured results. After having validated this prototype, this t-line is used in the following to make the connection between the AUT and 2.40 mm-connector.

VI The connection between the t-line and the chip

It is straightforward to connect the t-line to the 2.4 mm connector, but the connection between t-line and the AUT is rather delicate as the size of the chip's pads and the size of the t-line pads are both small and different (Figure 4. 23). In this section, we compare two methods for making this connection. One uses wire-bonding and the other uses a modified flip-chip bonding.

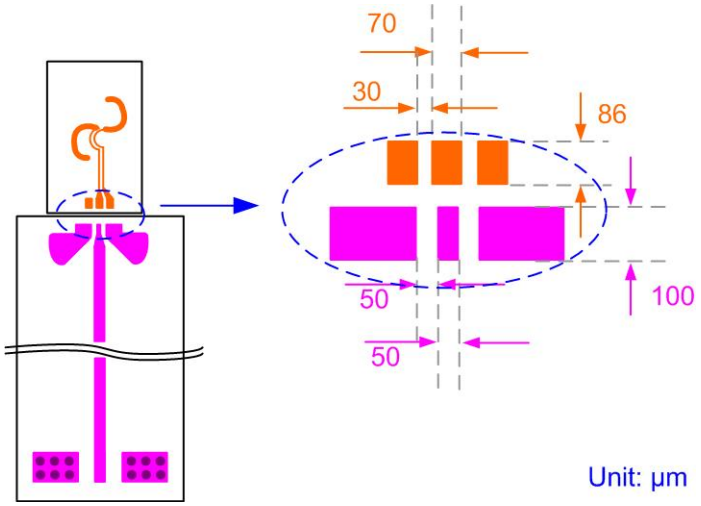

Figure 4. 23 Zoom on the connection zone for the GSG pads with their dimensions.

VI.I Wire bonding

Wire bonding is an electrical interconnection technique using thin metallic wires. It is a welding process which makes the two metallic parts (wire and pad surface) have an intimate contact. It is considered the most cost-effective and flexible interconnect technology and is used to assemble the vast majority of semiconductor packages. Aluminum, copper and gold are the usual choices for the bond wire materials. The

wire diameters can range from several micrometers to several hundred micrometers depending on the application [18].

In current practice, according to the bonding agent, pressure and heat, three major bonding processes can be defined [19]:

- Thermocompression (TC): this process combines a high pressure with high temperature (300°-500°) to melt the metal and form a firm junction.
- Ultrasonic (US): this process uses an ultrasonic energy to weld with a low pressure in the ambient temperature, the heat focus on the joint precisely. This process is suitable for the thermally sensitive materials and fragile components.
- Thermosonic (TS): this process uses an ultrasonic energy (up to 20 W) to weld with a low pressure at a moderate temperature (100°-150°).

These different processes lead to two wirebond forms: the ball bond and the wedge bond as shown in Figure 4. 24 (a) and (b). The following table shows the bond form with corresponding bonding tool and bonding technique.

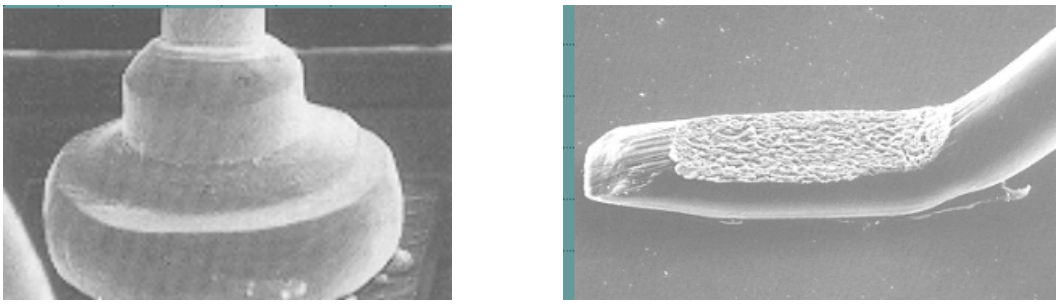

Figure 4. 24 (a) Ball bond; (b) wedge bond.

Table 4.1 Bond formation

Wirebond	**Bonding technique**	**Bonding tool**	**Pad**
Ball bond	TC, TS	Capillary	Al, Au
Wedge bond	TS, US	Wedge	Al, Au

Creating a ball bond requires heat, so it is restricted to gold and copper wire, whereas wedge bonds can use copper, gold or aluminum wire. The advantage of the ball bond is that that the wire can move in any direction without causing stress on the wire.

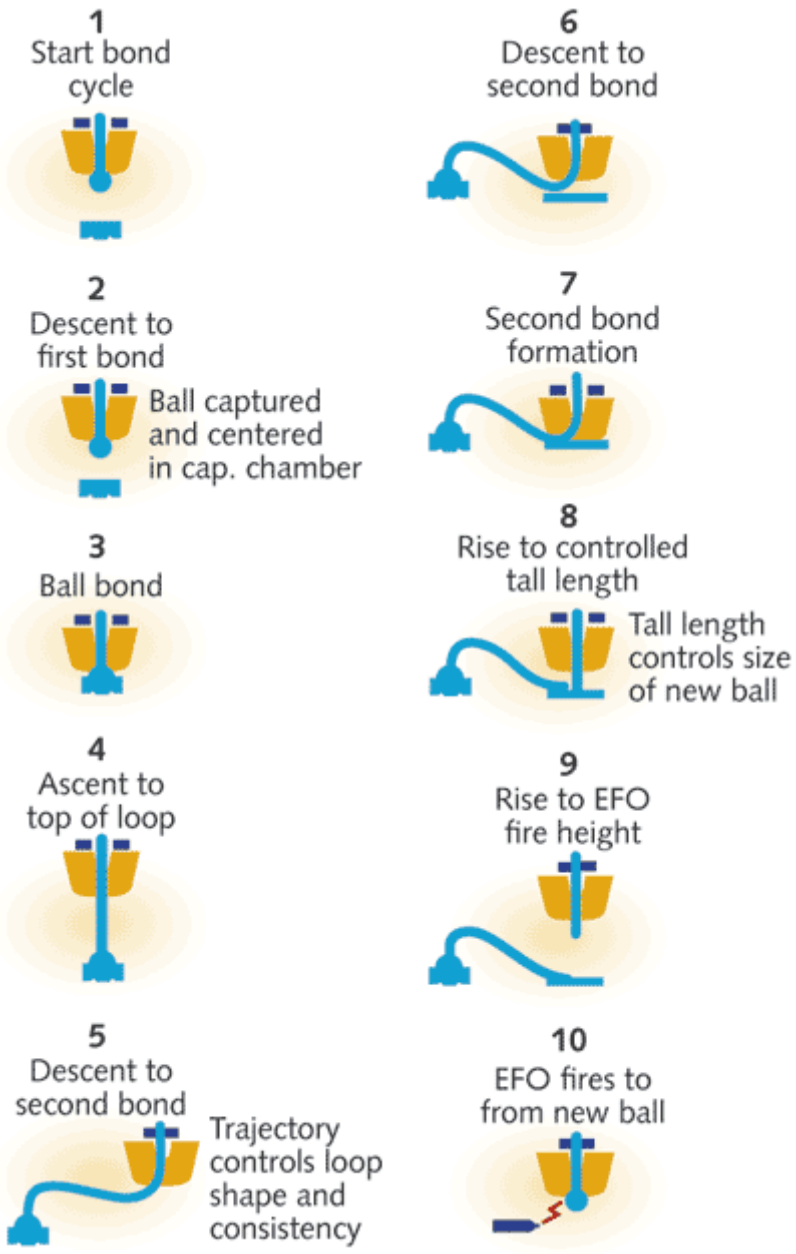

Figure 4. 25 The wire-bonding cycle (from [20])

Figure 4. 25 shows the ball bonding process in detail [20]. There are three main steps:

- First bond: The capillary releases the wire from the wire clamp and a ball is formed at the end of the wire due to the surface tension of the metal. Then the capillary aims at the first bond position and descends to this point, where high temperature or ultrasound are applied, which deform the ball to make a contact (Steps 1-2 in Figure 4. 25).

- Drag the wire: After the first ball is bonded onto the chip, the wire is dragged out through the capillary and reaches the second target position, which is usually called the leadframe [21]. The capillary again descends, this time to the second bond position with a parabolic or elliptical motion. The end of the wire is crushed between the leadframe and the tip of the capillary, producing a wedge shape transition (Steps 3-7).

- Form a new ball: In the final step, a small amount of wire is left hanging from the end of the capillary. An electronic flame-off (EFO) activates and the remaining small amount of wire melts, forming a ball thus ensuring connection at the second target point.

We make a wirebonding connection between the t-line and the chip as shown in Figure 4. 26. The ground plane of the t-line and the ground plane of the chip are on the same plane. The bond wires suspend in the air and connect the GSG pads at a different height. The characterization of this configuration will be presented in the next section.

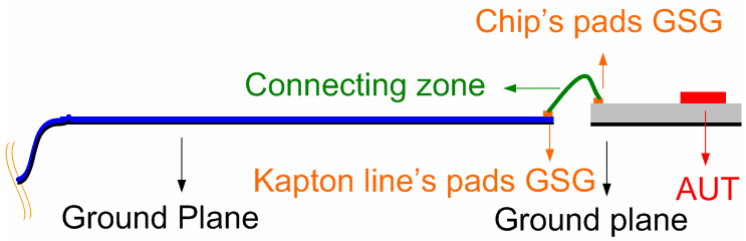

Figure 4. 26 Schematic of the connection between the t-line and the AUT using wirebonding technique.

VI.II Modified flip chip connection

Flip chip is a method of connecting electrical components using bumps rather than bond wires. Instead of having a face-up chip, the chip faces down in order to make the connection shorter.

The process of flip chip connection involves:

- Ball transfer: Align the solder balls with the pads on the chips, then deposit them on the pads.

- Flip the bumped chip so that solder balls are facing the board, then remelt the bumps.
- Underfill the encapsulation using an electrically-insulating adhesive.

We prefer to use a flip chip connection rather than wirebonding as this technique avoids having any bond wires suspended in the air which may produce parasitic radiation and impedance mismatch. However the conventional ball size for a flip chip package is around 0.1 mm to 0.2 mm in diameter, which is too big for our pads connection. Thus we have to find a new way of using this technique. In fact we use a technique that is a hybrid between flip chip and wirebonding. Figure 4. 27 shows the modified chip connection in our application. We used gold bond wires with a diameter of 18 µm to make the ball bonds.

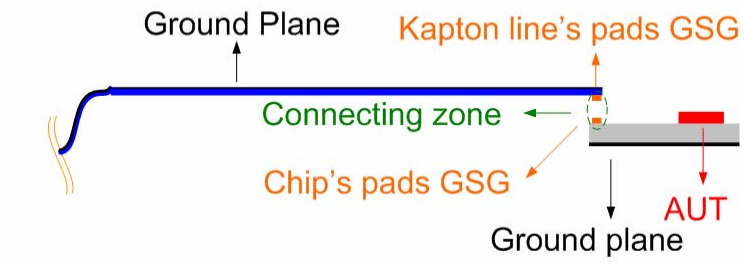

Figure 4. 27 Schematic of the connection between the t-line and the AUT using flip chip connection.

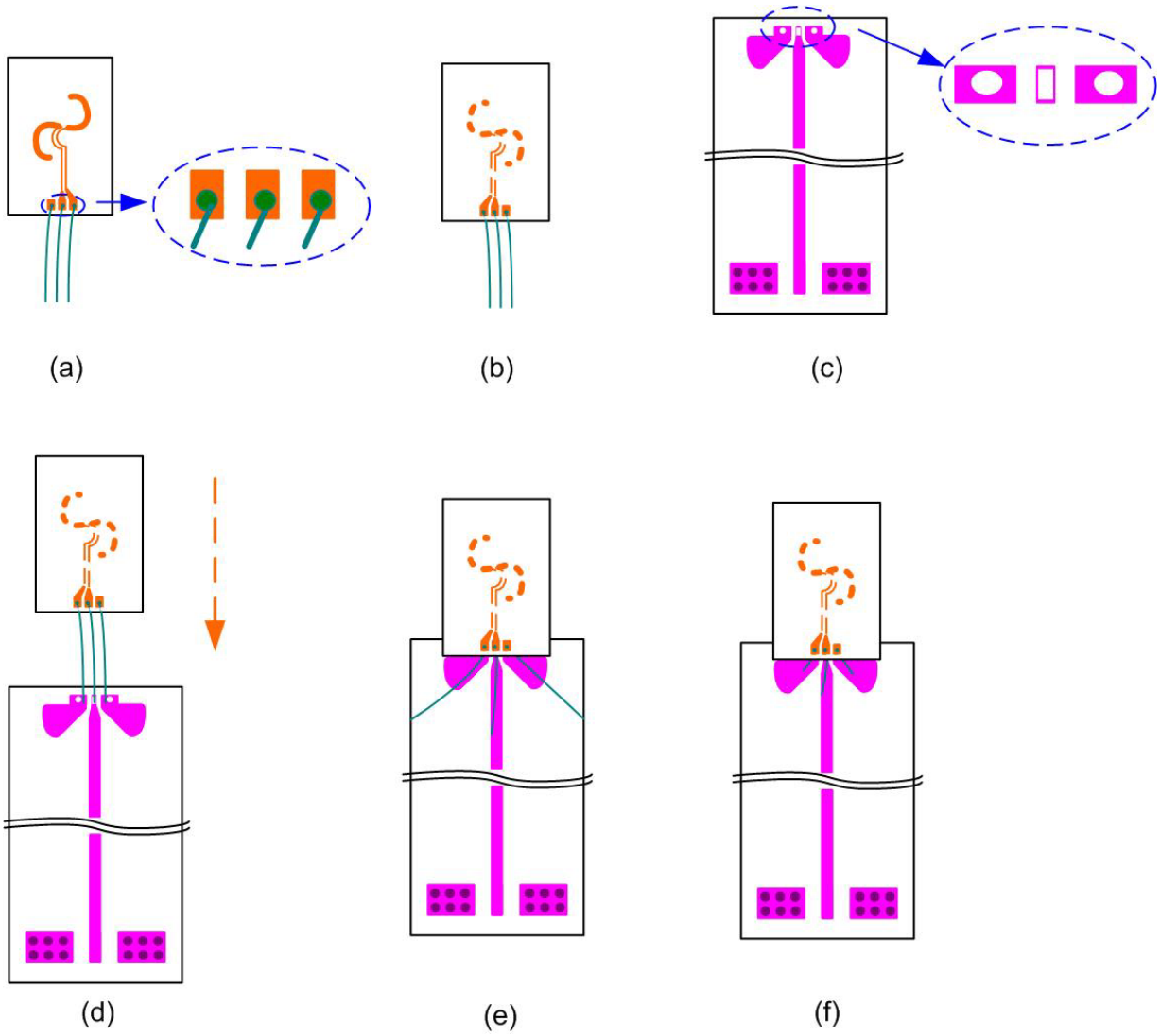

Figure 4. 28 The realization steps in our flip chip connection method.

Our modified flip chip connection method was as follows (see Figure 4. 28):

(a) The AUT is placed on a metallic support and three bond wires are made between the GSG pads of the chip and the support;

(b) The connection is released from the support without breaking the connection on the pads. The three bond wires remain suspended in the air while the chip is turned over;

(c) A silver glue is deposited on the transmission line's pads;

(d) The chip is aligned above the transmission line;

(e) The chip is pressed slightly to ensure a good contact;

(f) The whole object is heated to make the connection solid, and the extra wires suspended in the air are cut.

All the operations are done under a microscope: step (d) is quite delicate as it should meet the following criteria

- The pads should be well aligned and connected as the top component is not transparent.
- The connection should not be short circuited.

VII Characterization of the AUT

In this section, we present experimental characterization results for the two connection methods described in the previous section and we compare them with simulation results.

We use the test bench as shown in Figure 4. 29. Instead of the using a probe system, the AUT is fed through a connector plus a transmission line. A motorized horn antenna rotates about two perpendicular horizontal axes with the AUT at the centre. The data is acquired by a VNA. The schematic of the chain is shown in Figure 4. 30.

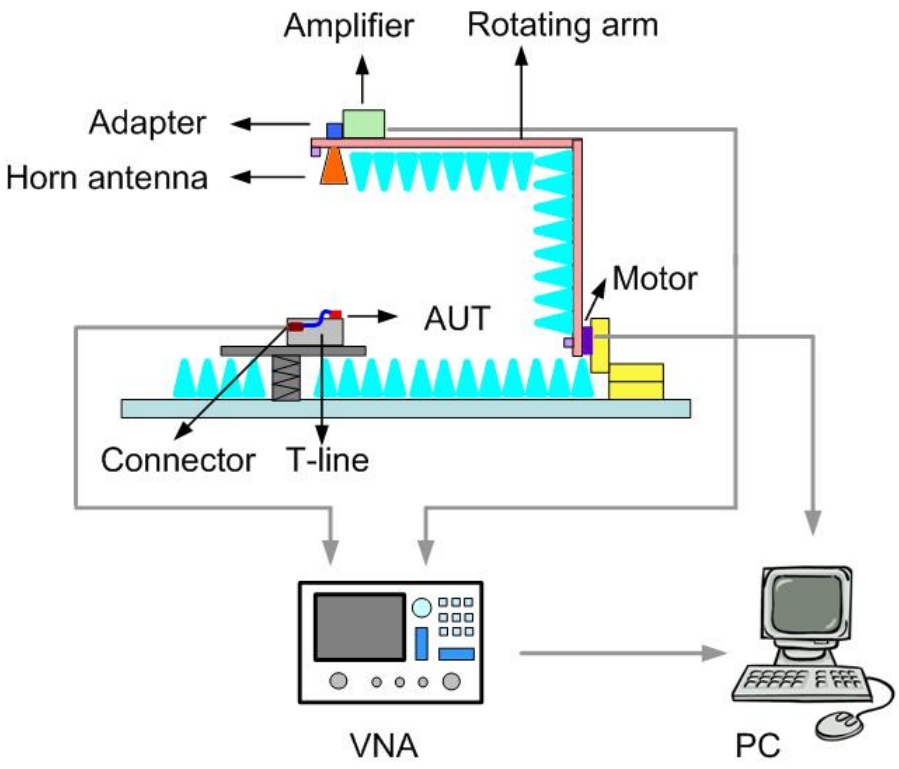

Figure 4. 29 Schematic of the test bench.

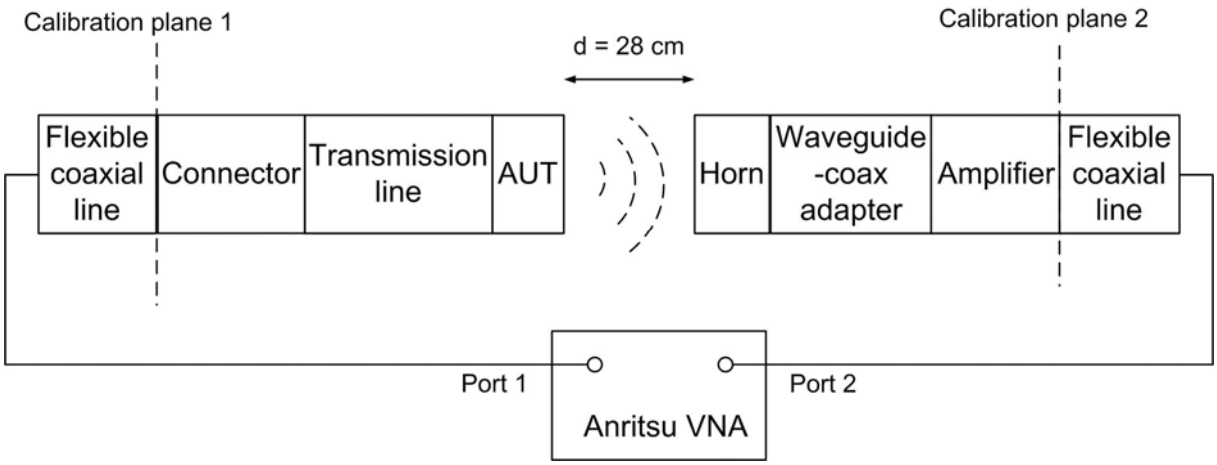

Figure 4. 30 Schematic of the measurement chain.

We used a Short – Open - Load – Thru (SOLT) coaxial calibration for the range 50-65 GHz. The calibration planes were set at the end of the two flexible coaxial cables (Figure 4. 30).

We applied the Friis equation to calculate the gain values, here we took additionally into account the t-line and connector losses:

$$G_{AUT} = S_{21} - G_{Horn} - G_{Amplifier} + L_{Adapter} + L_{Kapton\_line} + L_{Connector} - \left(\frac{\lambda^2}{(4\pi d)^2}\right)_{dB} \qquad (5.2)$$

where $L_{Kapton} \approx 5.3$ dB is the microstrip t-line loss and $L_{Connector} \approx 1.25$ dB is the connector insertion loss at 59 GHz.

VII.I Comparison between simulation and experiment for the wirebonding technique

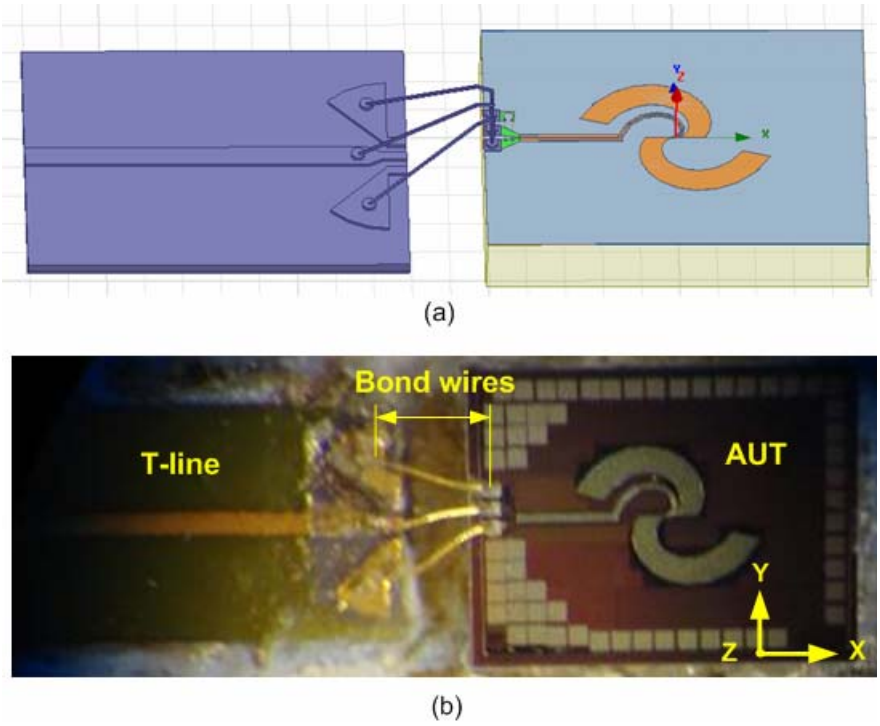

Figure 4. 31 Photo of the connection between the t-line and the AUT using conventional wirebonding.

Our simulation model is shown in Figure 4. 31 (a) and consists of the AUT plus three bond wires plus a small segment of the t-line. The model is excited at the end of the microstrip line. The model of the bond wires is based on the geometry of the real product (Figure 4. 31 (b)) as observed under a microscope, and is subsequently fine-tuned to provide a good match between the measured and simulated results. HFSS provides a bond wire model shown in Figure 4. 32 (a). This model has three main factors that can influence the impedance matching and radiation pattern: H_1, H_2, and D. However in our case, the angle between the centre line and the ground lines α should also be taken into consideration (Figure 4. 32 (b)). The model assumes H1=0.18 mm, H2=0.2 mm, and D=0.68 mm and α=21.2°

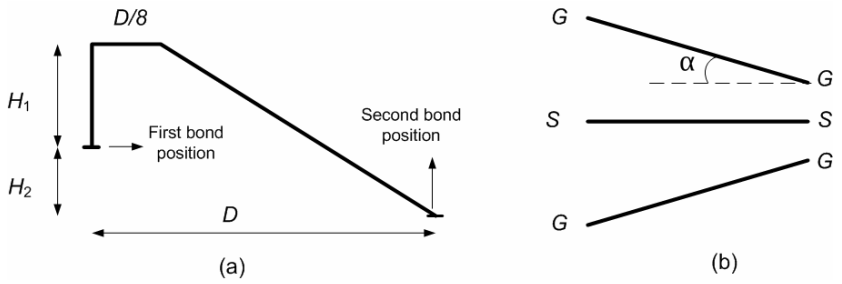

Figure 4. 32 (a) Simulation model of a bond wire; (b) top view of the GSG bond wires.

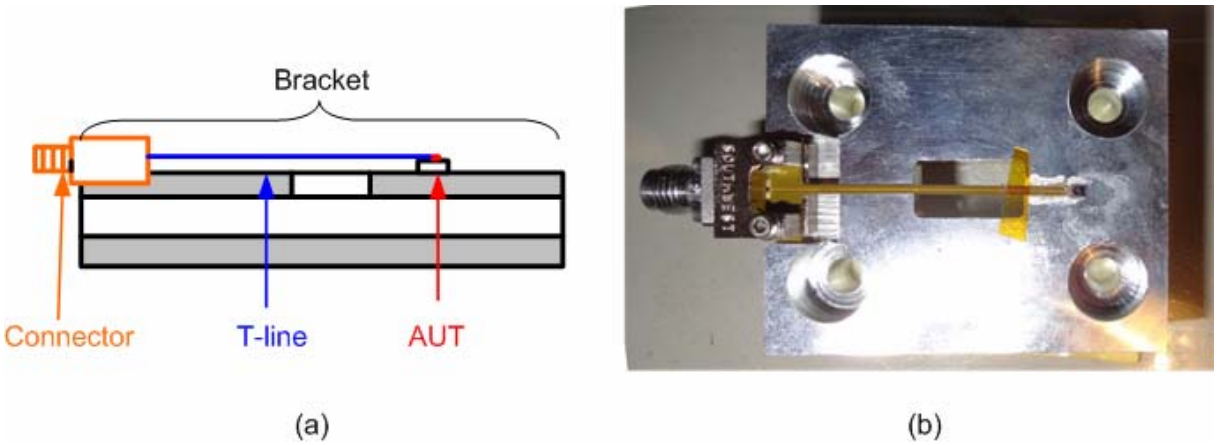

Figure 4. 33 (a) The longitudinal section of the bracket with the AUT, the t-line and the 2.40 mm-connector; (b) a photo of the bracket with the AUT, the t-line and the 2.40 mm-connector (wirebonding technique).

Figure 4. 34 shows the simulated and measured gain of the AUT plus bond wires in the ZX and YZ planes at 59 GHz. Due to the losses from the bond wires, the gain is never more than -10 dB in any plane and the patterns have significant ripples. There are still some differences between the simulated and measured results. One reason is that the simulation assumes that the bondwires are symmetric, whereas it is hard to fabricate each bond wire with the same H_1, H_2 and D and to ensure the exact same value for the angle α. There are more frequent and significant ripples in the ZX-plane than that in the YZ-plane. This is due to reflections and parasitic radiations from the 2.40 mm-connector which are not part of the simulation.

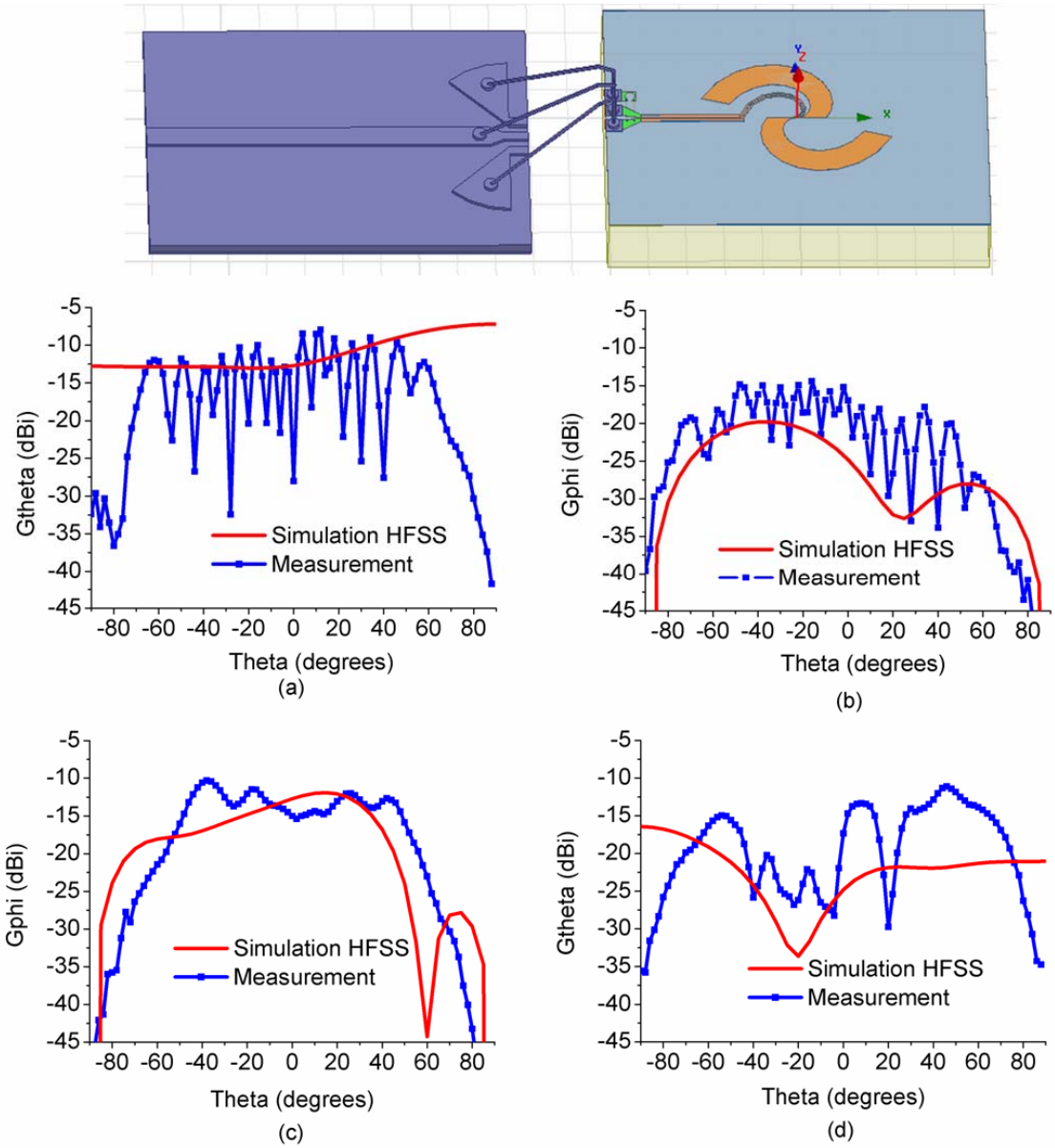

Figure 4. 34 Simulated and measured gain radiation patterns using wirebonding technique: (a) ZX plane co- polarization; (b) ZX plane cross-polarization; (c) YZ plane co-polarization; (d) YZ plane cross-polarization.

In conclusion, wirebonding is not suitable for making connections with integrated millimeter-wave antennas.

VII.II Characterization with the AUT using the flip chip wirebonding

The t-line is mounted as shown in Figure 4. 35 with a connection similar to flip chip. Figure 4. 36 presents a longitudinal section of the bracket with the AUT, the t-line and

the 2.40mm-connector. The AUT is facing upwards, the transmission line is facing downwards and the 2.40 mm-connector is fixed up-side-down. The transmission line starts to bend above the hole. There are 2-3 mm of the t-line in the upper hemi-sphere, the rest of the line lies under the ground plane.

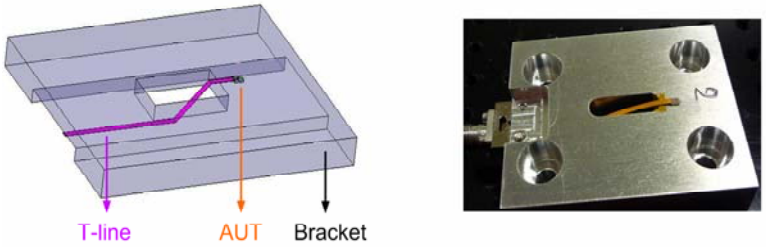

Figure 4. 35 The simulation model and the photo of the bracket with the AUT, the t-line and the 2.40 mm-connector. (modified flip chip technique).

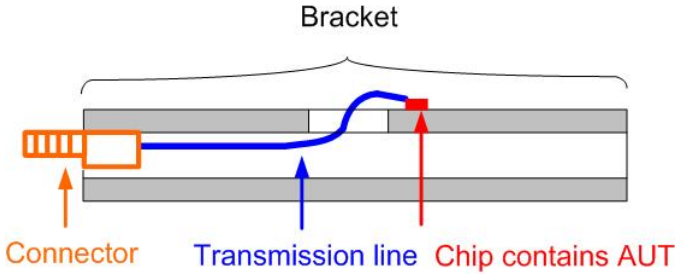

Figure 4. 36 The longitudinal section of the bracket with the AUT, the t-line and the 2.40 mm-connector. (modified flip chip technique).

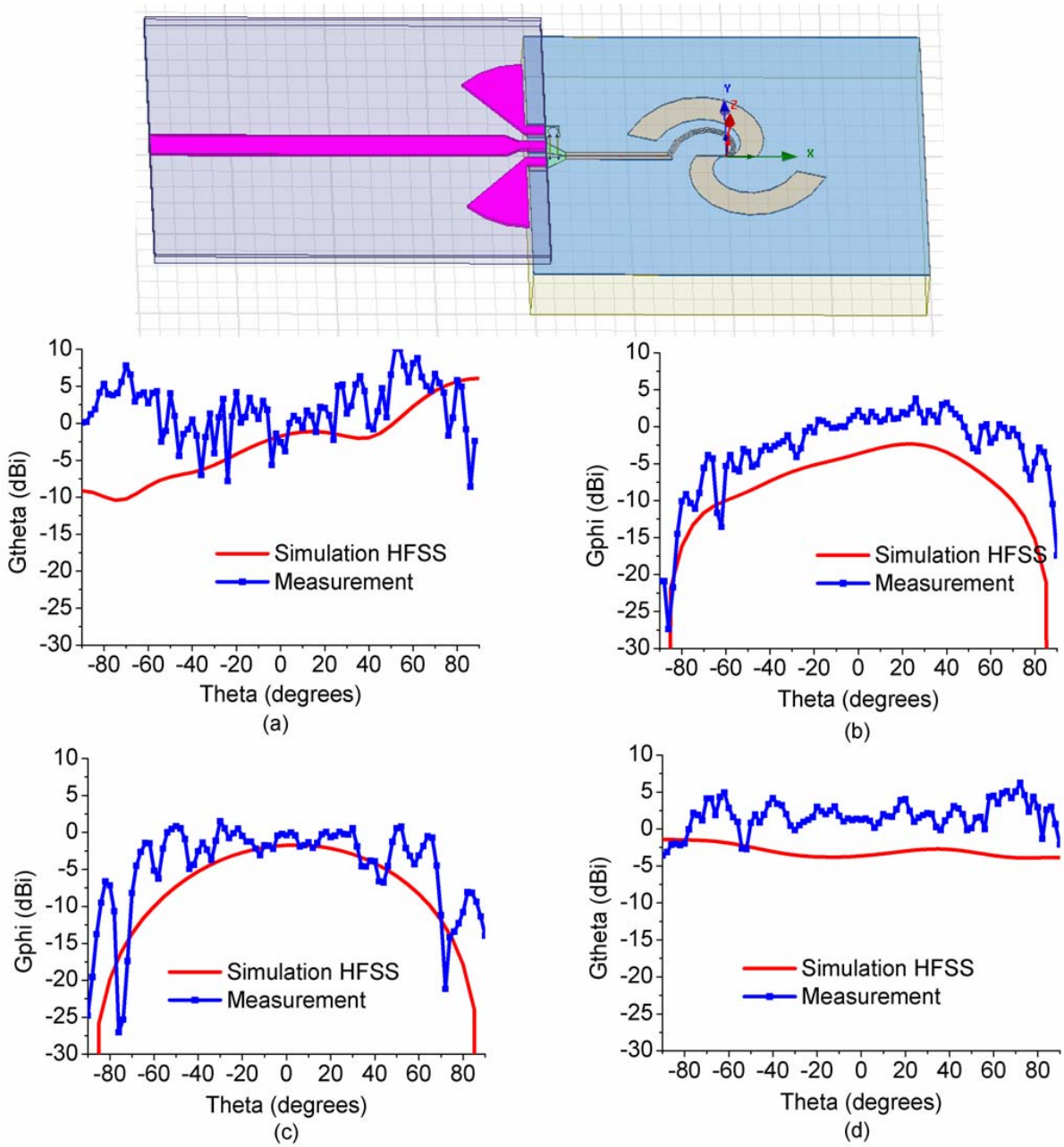

Figure 4. 37 Simulated and measured gain radiation patterns using modified flip chip technique: (a) ZX plane co- polarization; (b) ZX plane cross-polarization; (c) YZ plane co-polarization; (d) YZ plane cross-polarization.

Figure 4. 37 shows the simulated and measured gains of the AUT with a flip-chip connection in the ZX- and YZ-planes at 59 GHz. There is no more masked zone: the effective angular scanning sector achieved is [-90º, 90º], so that it is possible to cover the whole hemisphere with this method.

As we can see, the shape and average level of the measured gain components in the all planes exhibit a reasonable agreement with the simulation results. Indeed, using the flip-chip connection we see a decreasing ratio of co- and cross- polarization in

both simulation and measurement.

However, as shown in Table 2, substantial ripples are obtained, which are likely due to the scattering of the AUT radiation on the bracket. A possible solution would be to cover the bracket with a thin absorbing material. For the cross-polarization components, the gain is approximately 5 dB higher than the simulation results. The main difficulty and uncertainty in this measurement technique comes from the flip-chip connection which requires a highly accurate alignment of the contact-pads because of their small dimension and pitch. The dimensions of the GSG contact pads are 86×70 μm^2 on the chip and 100×50 μm^2 on the t-line both with a pitch of 100 μm. A small misalignment may lead to an asymmetric excitation of the two spiral arms. We have conducted simulations with and without the flip-chip connection (results not shown). This uncertainty about the connection is currently under investigation at the time of submission of this thesis, but it may explain the discrepancies observed between the measured and simulated gains.

Furthermore, in reality, the presence of three bond wires sticking on the radial quarter-wavelength stubs and centre line may cause decreasing ratio of the gain in co- and cross-polarization which is not included in the simulation model.

Table 4.2 Analysis of the measurement results with the flexible t-line feeding technique (flip-chip connection).

Kapton	**ZX plane** (co-polarization)	**YZ plane** (co-polarization)	**ZX plane** (cross-polarization)	**YZ plane** (cross-polarization)
$\Delta\bar{G}$ (dB)	5.09	3.13	4.74	5.11
R_{rms} (dB)	4.33	3.12	1.90	1.73

VIII Conclusion

In this chapter we presented a feeding technique based on the use of a flexible transmission line. This t-line enables the use of a standard 2.40 mm-connector placed below the antenna's ground plane. The experimental results confirmed the absence of masking effect. To implement this technique, we designed and fabricated a t-line on a flexible substrate and demonstrated that Kapton is a suitable substrate for millimeter-wave frequencies. We compared the performance of wirebonding and a modified flip chip connection. As expected the wirebonding did not perform well.

However, the results with the modified flip chip connection are promising as there was significantly less parasitic radiation as with the wirebonds. Future improvements of this technique will require specific designs of the bonding pads on the chip and a more accurate flip-chip bonding.

References:

[1] Y. Xu, "Chracterization and modeling of static properties and low-freuqency noise in organic field –fffect transistor (OFETs)", Ph.D thesis, Grenoble University, Grenoble, 2011.

[2] W.S. Wong, and A. Salleo, "*Flexible electronics: materials and applications"*, Springer Verlag, 2009.

[3] "LG.Philips LCD Develops World's First Flexible Color A4-Size E-Paper," [online]. Available: http://www.keyimagery.com/community/articles/article/132/lgphilips-lcd-develops-worlds-first-flexible-color-a4-size-e-paper

[4] Samsung [online].Available: http://www.samsung.com/us/business/components/lcdpanels/index.html

[5] Business Wire 2004, "Universal Display Corporation and PARC Announce Collaboration to Develop Backplane Technology for OLED Displays on Flexible Metallic Substrates" [online]. Available: http://findarticles.com/p/articles/mi_m0EIN/is_2004_June_23/ai_n6086333/

[6] Dupond [online]. Available: http://www2.dupond.com/Kapton/en_US/

[7] R.V. Goteti, R.E. Jackson, and R. Ramadoss, "MEMS-Based Frequency Switchable Microstrip Patch Antenna Fabricated Using Printed Circuit Processing Techniques," *Antennas and Wireless Propagation Letters, IEEE*, vol. 5, no. 1, 2006, pp. 228-230.

[8] G. DeJean, R. Bairavasubramanian, D. Thompson, G.E. Ponchak, M.M. Tentzeris, and J. Papapolymerou, "Liquid Crystal polymer (LCP): a new organic material for the development of multilayer dual-frequency/dual-polarization flexible antenna arrays," *Antennas and Wireless Propagation Letters, IEEE*, vol. 4, 2005, pp. 22-26.

[9] S. Hage-Ali, N. Tiercelin, P. Coquet, R. Sauleau, V. Preobrazhensky, and P. Pernod, "Millimeter-wave patch array antenna on ultra flexible micromachined Polydimethylsiloxane (PDMS) substrate," *Antennas and Propagation Society International Symposium, 2009. APSURSI '09. IEEE*, pp. 1-4.

[10] ADS Momentum [online]. Available: http://www.home.agilent.com/agilent/product.jspx?cc=FR&lc=fre&ckey=1887116&nid=-33748.0.00&id=1887116&pselect=SR.GENERAL

[11] Cibel [online]. Available:: http://www.cibel.com/upload/limite-faisabilite-2011.pdf

[12] Edgeflex [online]. Available: http://www.edgeflex.com

[13] Db electronics ® Daniel Böck AG [online]. Available: http://ww.neust-pcb.de/index.php?nav=38subnav=2&lang=fr

[14] Southwest Microwave [online]. Available: http://mpd.southwestmicrowave.com/pdf/series_endlaunch.pdf

[15] Y. Wang, and M.J. Lancaster, "Coplanar to microstrip transitions for on-wafer measurements," Microwave and Optical Technology Letters, vol. 49, no. 1, 2007, pp. 100-103.

[16] H. Yousef, C. Shi, and H. Kratz, "Substrate Integrated Waveguides (SIWs) in a Flexible Printed Circuit Board for Millimeter-Wave Applications," Microelectromechanical Systems, Journal of, vol. 18, no. 1, 2009, pp. 154-162.

[17] H. Sharifi, R.R. Lahiji, L. Han-Chung, P.D. Ye, L.P.B. Katehi, and S. Mohammadi, "Characterization of Parylene-N as Flexible Substrate and Passivation Layer for Microwave and Millimeter-Wave Integrated Circuits," Advanced Packaging, IEEE Transactions on, vol. 32, no. 1, 2009, pp. 84-92.

[18] Heraeus [online]. Available: http://heraeus-contactmaterials.com/en/services/bondlabor/bondlabor_1.aspx

[19] http://www.finetechusa.com/bonders/technologies/ultrasonic-thermosonic-bonding.html

[20] I.W. Qin, "Wire Bonding Tutorial," Advanced Packaging, vol. 14, no. 7, 2005.

[21] Siliconfareast [online]. Available: http://www.siliconfareast.com/leadframes.htm

Chapter V
Characterizing millimeter-wave antennas using Radar Cross-Section Measurement

I Introduction

In the previous two chapters, we presented two characterization methods which involve supplying the AUT through a cable, while in this chapter we investigate a cable-free antenna characterization method: the RCS (Radar Cross Section) method. The advantage of this technique is that the AUT is not fed by any probe system or any special connector, thus there is no perturbation from any feeding system. Instead, the AUT is connected to three known loads successively and the gain pattern is determined from its scattering properties when connected to these loads. While this characterization technique has been experimented for a long time at microwave frequencies, its implementation at millimeter-wave for the integrated antenna investigated in this thesis is challenging. Therefore, this chapter presents a feasibility study using electromagnetic simulations.

II Radar systems

The measurement method is based on a classical radar technique in which the radar emits electromagnetic waves towards a target, the waves are reflected by the surface of the target and detected by the radar.

According to the IEEE Standard Definitions of Terms [1], the radar cross section (RCS) of a target is defined as: “For a given scattering object, upon which a plane wave is incident, that portion of the scattering cross-section corresponding to a specified polarization component of the scattered wave.” From this definition, the RCS could be written in units of m^2 as

$$\sigma = \lim_{R \to \infty} 4\pi R^2 \frac{|E_r|^2}{|E_i|^2} \tag{5.1}$$

where

- E_r is the far-field scattered electrical field (V/m)
- E_i is the far-field incident electrical field (V/m)
- R is the distance between the scattering object and the source of the plane wave (m).

The larger the RCS, the easier the target can be detected. There are two main types of factors that influence the RCS measurement: one relates to the target, such as the material, the shape, the size of the object compared with the wavelength; and the other relates to the radar system (radar plus propagation media plus the target), such as the incident angle of the energy, the distance between the radar and the target, and the transmission power of the radar.

Figure 5. 1 shows a typical monostatic (*i.e.* using a single antenna for both emission and reception) radar system [2] in which R is the distance between the emitting/receiving antenna and the target. The principle of this method is that the radar emits an electromagnetic wave at power P_t, which impinges on the target. The electromagnetic wave induces oscillation charges and currents inside and on the surface of the target body. Even dielectric materials are capable of supporting induced RF currents on their surface and volume. The electromagnetic wave is re-emitted by the target and captured by the radar receiver with power P_r.

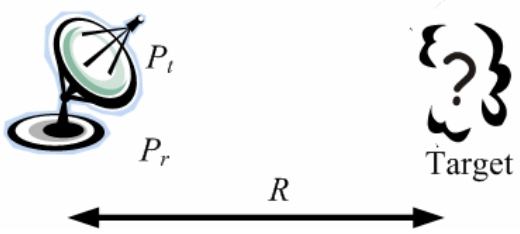

Figure 5. 1 Monostatic radar system measurement.

By definition, the scattered power from a scattering target is (in W):

$$P_s = \frac{P_t G_t}{4\pi R^2}\sigma \tag{5.2}$$

and the power received by the receiving antenna is (in W)

$$P_r = \frac{P_t G_t}{4\pi R^2}\sigma \frac{1}{4\pi R^2} A_{eff} \tag{5.3}$$

where P_r is defined as the power received back from the target by the radar (in W) and A_{eff} is the effective aperture of the receiving antenna, which is defined in terms of the

gain G_r and wavelength λ as:

$$A_{eff} = \frac{\lambda^2 G_r}{4\pi} \tag{5.4}$$

From equations (5.2) and (5.3), equating G_r and G_t, gives the radar equation:

$$P_r = \frac{P_t G^2 \lambda^2}{(4\pi)^3 R^4} \sigma \tag{5.5}$$

which is a relationship we will use in the calculations below.

III Application of the RCS method to antenna characterization

III.I Motivation

In this section, we study the feasibility of characterizing the gain and radiation pattern of integrated millimeter-wave antennas by measuring their RCS. In our method, the AUT is considered as the scattering target and a horn antenna is used as an emitting/receiving antenna.

Some work has been reported regarding the analysis and measurement of antennas' scattering properties in [3-28]. Among these references, [10-15] only need to study the RCS σ in order to check the functionality of an RFID system, whereas references [17-27] extract other antenna characteristics from the RCS measurements, such as the radiation impedance [16], the reflection coefficient S_{11} [17-21] and the gain [19-27].

We are particularly interested in characterizing the gain, so let us consider references [19-27] in more detail. References [19-24] modeled and measured the gain with the help of different loads, whereas [26, 27] used maximum and minimum σ values to determine the gain. The references considered different frequency bands, ranging from patch antennas at 433 MHz [24], flat printed dipoles at 800 MHz [19, 20], monopolar wire patch antennas at 950 MHz [19, 20], UWB dipoles for 1.5-3 GHz [19, 20], S-band horns [27], X-band horns [23], planar patch array antennas at 10.3 GHz [23], although none of these references considered millimeter waves.

One potential issue with applying this technique to millimeter-wave integrated antennas is that the power scattered by the AUT could be weak compared with the power reflected by the horn antenna due to its imperfect impedance matching. Thus in the next section, we are going to analyze the order of magnitude of the scattered power for millimeter-wave antennas.

III.II Simulation model

In order to analyze the power budget of the monostatic radar system, we created two simulation models using Ansys-HFSS. In both models, the AUT is the spiral antenna integrated using CMOS SOI technology that was described in Chapter II.

Simulation Model 1:

As the RCS σ (Radar Cross Section) can be directly calculated by the simulator, the AUT is connected with a 50 Ω load and excited by "plane waves" with polarization x and y successively. The convergence parameter is set to 0.001 to ensure a precision of -60 dB. We get simulated RCS σ_{simu} in co-polarization with three different loads (50 Ω, short and open) at 60 GHz.

- σ_{simu_short} = -47.35 dBsm
- σ_{simu_50} =-49.96 dBsm
- $\sigma_{simu\_open=}$ -48.68 dBsm.

Rmk: dBsm – decibel measure of the RCS of a target relative to one square meter.

This model gives a reference RCS of σ_{simu}.

Simulation Model 2:

As in practice, a horn antenna generates the incident wave and receives the scattering wave, our model 2 simulates a monostatic radar system. It is composed of a horn antenna and the integrated spiral antenna. Before presenting the power budget of the whole monostatic radar system, we firstly give the horn antenna's characteristics in the model.

- **An emitting and receiving horn antenna**

The dimensions of the radiating aperture of the horn antenna are 6.1×3.5 mm^2 and

its length is 12 mm (Figure 5. 2). The reflection coefficient is under -18 dB in the [50, 70] GHz range (Figure 5. 3). It has a nominal gain of 10.42 dBi at 60 GHz and its cross-polarization level is below -35 dB (Figure 5. 4).

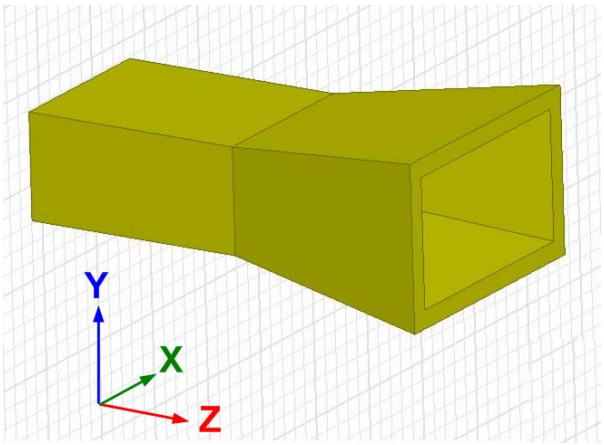

Figure 5. 2 Simulation model of the horn antenna

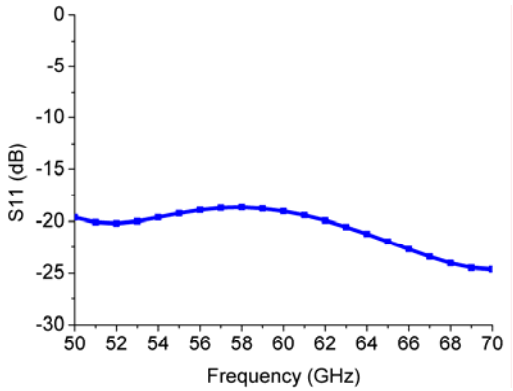

Figure 5. 3 Reflection coefficient of the horn antenna.

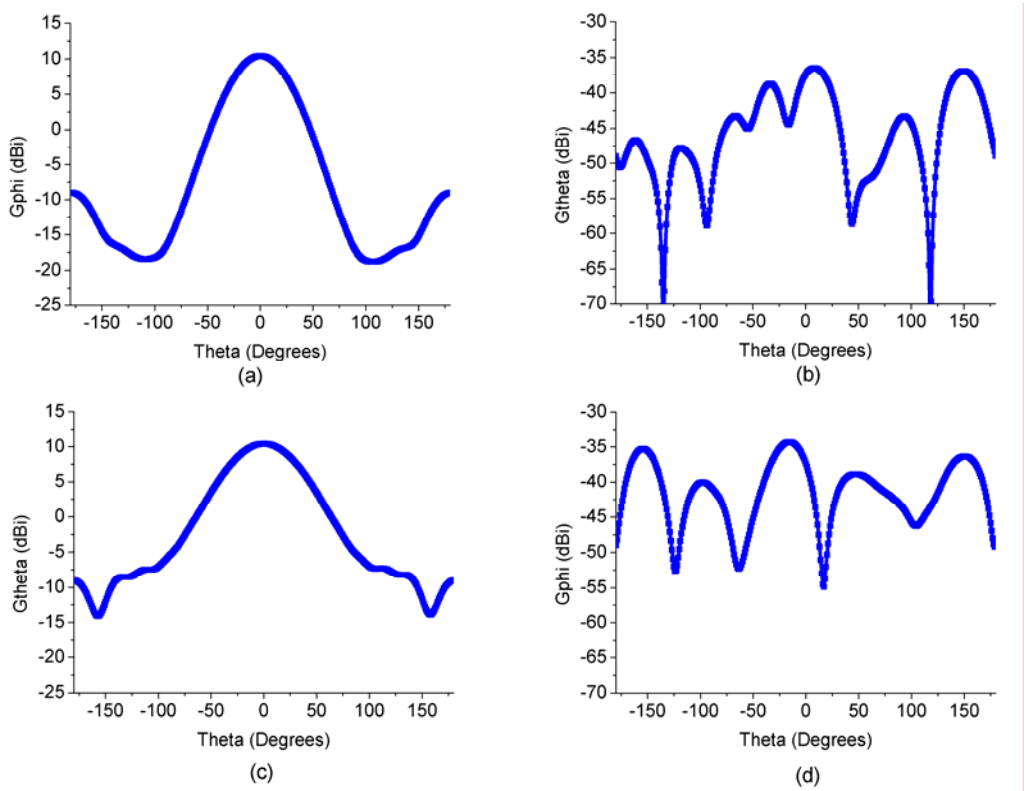

Figure 5. 4 Horn antenna simulated radiation pattern at 60 GHz: (a) ZX plane co-polarization; (b) ZX plane cross-polarization; (c) YZ plane co-polarization; (d) YZ plane cross-polarization.

As we can see from Figure 5. 3, the horn is not perfectly matched and this will influence the RCS method's precision. In particular, the reflected power due to the mismatch of the horn may be much higher than the power scattered from the AUT, so we should take the reflection coefficient of the horn into consideration.

- **Model of the measurement system**

The simulation model and the schematic of the complete system are shown in Figure 5. 5 and Figure 5. 6 respectively. The distance between the two antennas is 30 mm which is measured from the aperture of the horn antenna to the integrated spiral antenna. This distance satisfies the far-field condition ($R > 2D^2/\lambda = 14.88$ mm). A waveguide port is set to feed horn antenna. The AUT is connected to a 50 Ω load. S_{11_sys} represents the reflection coefficient of the whole system.

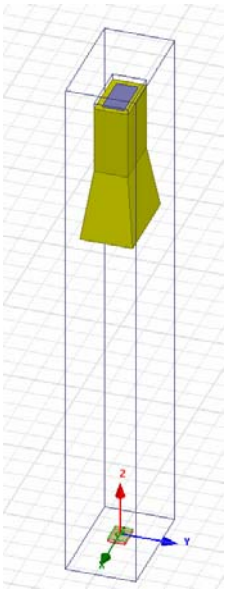

Figure 5. 5 Simulation model of the complete system.

P_0, P_1 and P_2 are the incident, reflected and transmitted power vectors at the port of the horn. w_3 and w_4 are the incident and scattered power densities on the surface of the AUT. P_5, P_6 and P_7 are the incident, reflected and transmitted return power vectors.

The convergence parameter was set to 0.0005, corresponding to a simulation precision of -66 dB.

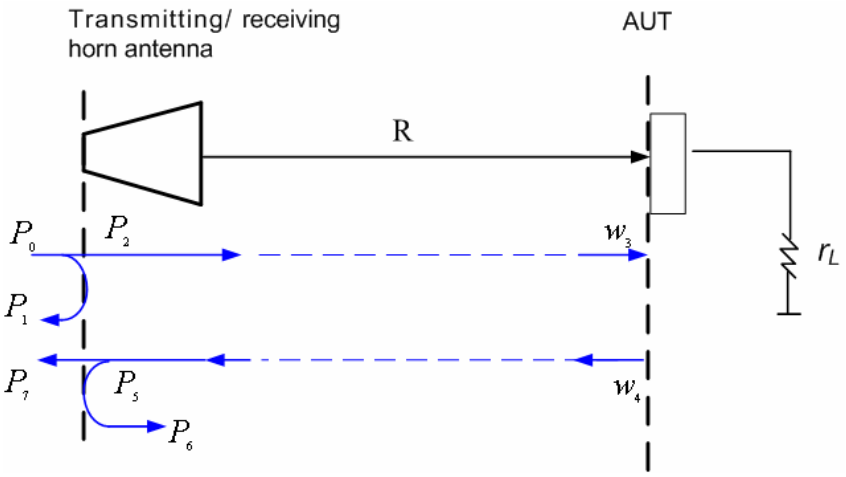

Figure 5. 6 Schematic of the simulated complete system.

As we discussed previously, the horn is not perfectly matched. This phenomenon is modeled by S_{11_horn} which in our notation is given by

$$\left|S_{11\_horn}\right| = \frac{\sqrt{P_1}}{\sqrt{P_0}} \tag{5.6}$$

The same is also true for scattered waves that impinges on the horn, so

$$\left|S_{11\_horn}\right| = \frac{\sqrt{P_6}}{\sqrt{P_5}} \tag{5.7}$$

In the simulation of the monostatic radar system measurement, S_{11_sys} corresponds to the sum of the reflected power vector and scattered power vector:

$$\frac{\sqrt{P_1 - P_7}}{\sqrt{P_0}} \le \left|S_{11\_sys}\right| \le \frac{\sqrt{P_1 + P_7}}{\sqrt{P_0}} \tag{5.8}$$

The power values must satisfy the principle of conservation of energy, thus we have

$$P_1 + P_2 = P_0 \tag{5.9}$$

$$P_6 + P_7 = P_5 \tag{5.10}$$

In our application, radar equation 5.5 can be written:

$$\frac{P_5}{P_2} = \frac{G_{horn}}{4\pi R^2} \cdot \sigma \cdot \frac{1}{4\pi R^2} \cdot \frac{\lambda^2 G_{horn}}{4\pi} \tag{5.11}$$

$\frac{P_5}{P_2}$ can also be expressed as function of $\frac{P_7}{P_0}$ from equations (5.6-5.7, 5.9-5.10):

$$\frac{P_5}{P_2} = \frac{\dfrac{P_7}{\left(1-\left|S_{11\_horn}\right|^2\right)}}{\left(1-\left|S_{11\_horn}\right|^2\right) \cdot P_0} = \frac{1}{\left(1-\left|S_{11\_horn}\right|^2\right)^2} \cdot \frac{P_7}{P_0} \tag{5.12}$$

From equations 5.6 and 5.8, we have:

$$-P_7 \le P_0\left(\left|S_{11\_sys}\right|^2 - \left|S_{11\_horn}\right|^2\right) \le P_7 \quad \text{or} \quad P_0\left|\left|S_{11\_sys}\right|^2 - \left|S_{11\_horn}\right|^2\right| \le P_7$$

Thus, from equations 5.12, we have:

$$\frac{P_5}{P_2} \ge \frac{\left|\left|S_{11\_sys}\right|^2 - \left|S_{11\_horn}\right|^2\right|^2}{\left(1-\left|S_{11\_horn}\right|^2\right)^2} \tag{5.13}$$

Thus, the estimated minimum RCS σ can be written:

$$\sigma_{\min} \geq \frac{\left|\left|S_{11\_sys}\right|^2 - \left|S_{11\_horn}\right|^2\right|^2}{\left(1-\left|S_{11\_horn}\right|^2\right)^2} \cdot \frac{(4\pi)^3 R^4}{\lambda^2} \cdot \frac{1}{G^2{}_{horn}} \tag{5.14}$$

In conclusion, this simple calculation gives only a minimum value for the RCS σ_{min} because we don't know the relative phase of the waves P_1 and P_7 in equation 5.8. Applying this estimate to our simulation gives RCS σ_{min} at 60 GHz in co-polarization when the AUT is connected to three loads 50 Ω, short and open. It confirms that $\sigma_{simu} > \sigma_{min}$ with a difference of 2-2.5 dB.

Table 5.1 RCS σ_{min} of the AUT terminated with different loads at 60 GHz for co-polarization.

	Short	50Ω	Open
S_{11_horn}	-19.85dB / -58.67°		
S_{11_sys}	-19.49dB / -57.66°	-19.62dB / -57.35°	-19.52dB / -58.14°
σ_{min}	-49.21 dBsm	-51.44 dBsm	-50.55 dBsm
$\sigma_{simulated}$	-47.35 dBsm	-49.96 dBsm	-48.68 dBsm

As we can see in Table 5.1, the variation in S_{11_sys} with load is small for co-polarization at 60 GHz. Furthermore the RCS σ_{50} is smaller than σ_{short} and σ_{open} which meets our expectations.

In our simulation model, the returned scattered wave can be subtracted from S_{11_sys} since we are able to set very low convergence parameters to ensure high precision. However in practice, the feasibility of the RCS method will greatly depend on the sensitivity of the available measuring apparatus. As the power of the returned scattered wave is quite weak, if the apparatus has low sensitivity, this signal may be under the noise floor. As the variation in S_{11_sys} with load is of the order of 0.1 dB in the simulation, a practical implementation of the RCS method would require an instrumentation capable of measuring variations of 0.1 dB at low signal levels.

Now, model 2 simulates a monostatic radar system, which requires the use of a VNA. For a typical VNA, at 60 GHz, the dynamic range and accuracy in measurements of S_{11} are small which would limit the measurement accuracy of the scattered wave, so it would be difficult to record the small power variations of the scattered waves.

IV Conclusion and Future Work

In this chapter we simulated a monostatic radar system using Ansys-HFSS. We compared the RCS of a millimeter-wave antenna as computed directly by the simulator, with the estimated RCS as calculated from a simulation of the RCS measurement method. A favourable agreement was found. As the return loss of the horn antenna is large compared with the scattered power and the change in scattered power between the three loads is relatively weak, the scattered power could be masked in the noise level.

Thus it may be difficult to realize such a measurement setup using standard measurement equipments. One possible solution could be to use a bistatic radar system to make measurements in the time domain with separated emitted and scattered signals thanks to their relative time delay.

References:

[1] "IEEE Standard Definitions of Terms for Antennas," *IEEE Std 145-1983*, 1983, pp. 0_1.

[2] E.F. Knott, J.F. Shaeffer, and M.T. Tuley, *Radar cross section*, SciTech Publishing, 2004.

[3] R. Green, "Scattering from conjugate-matched antennas," *Antennas and Propagation, IEEE Transactions*, vol. 14, no. 1, 1966, pp. 17-21.

[4] J. Wang, *et al.*, "Precision experimental characterization of the scattering and radiation properties of antennas," *Antennas and Propagation, IEEE Transactions on*, vol. 30, pp. 108-112, 2002.

[5] Y. Liu, S.X. Gong, and D.M. Fu, "A novel model for analyzing the RCS of microstrip antenna," *Antennas and Propagation Society International Symposium, 2003*, pp. 835-838 vol. 834.

[6] S.H. Dike, and D. King, "The absorption gain and back-scattering cross section of the cylindrical antenna," *Proceedings of the IRE*, vol. 40, no. 7, 1952, pp. 853-860.

[7] G. Rafi, R. Moini, and A. Tavakoli, "Radar cross section of cross-shaped microstrip patch antennas," Electromagnetic Compatibility, 1995 IEEE International Symposium , pp. 303-307.

[8] R.B. Green, "The general theory of antenna scattering," OSU Report 1223-17, November, 1963.

[9] W.M. Boerner, W.L. Yan, A.Q. Xi, and Y. Yamaguchi, "Basic concepts of radar polarimetry," Proc. NATO Adv. Res. Worksh. Dir. Inv. Meth. Radar Polar, 1988.

[10] A. Pouzin, "Qualification d'element RFID en environnement operationnel," Ph.D thesis, INP Grenoble, 2009.

[11] P. Nikitin, and K. Rao, "Theory and measurement of backscattering from RFID tags," *IEEE Antennas and Propagation Magazine*, vol. 48, no. 6, 2006, pp. 212-218.

[12] S. Hu, C. Law, and W. Dou, "Measurements of UWB antennas backscattering characteristics for RFID systems," IEEE, pp. 94-99.

[13] K.J. Lee, D. Kim, M. Kim, M. Tanaka and K. Matsugatani, "A 2.4-GHz dual-patch RFID tag antenna scattering analysis," Microw. Opt. Technol. Lett., 48, 2006, pp. 2241–2244.

[14] J. Zhang, Z. Xie, S. Lai, and Z. Wu, "A design of RF receiving circuit of RFID reader," ICMMT, 2004, pp. 406-409.

[15] K. Penttila, M. Keskilammi, L. Sydanheimo and M. Kivikoski, “Radar cross-section analysis for passive RFID systems,” IET, pp. 103-109.

[16] M.H. Capstick, J.O. Jekkonen, A. Marvin, I.D. Flintoft, and L. Dawson, “A novel indirect method to determine the radiation impedance of a handheld antenna structure,” *Instrumentation and Measurement, IEEE Transactions*, vol. 58, no. 3, 2009, pp. 578-585.

[17] P. Pursula, D. Sandstrom, and K. Jaakkola, “Backscattering-based measurement of reactive antenna input impedance,” *Antennas and Propagation, IEEE Transactions,* vol. 56, no. 2, 2008, pp. 469-474.

[18] B. Monsalve, S. Blanch, J. Romeu, and L. Jofre, “A contact-less small antenna characterization through impedance modulation,” *Antennas and Propagation, 2009. EuCAP 2009. 3rd European Conference on*, pp. 696-698.

[19] S. Bories*, et al.*, "Small antennas impedance and gain characterization using backscattering measurements," Eucap 2010, pp. 1-5.

[20] K. Haj Khlifa, “Caractérisation expérimentale d’antennes électriquement petites,” DRT, CEA-LETI, Grenoble, 2009.

[21] W. Wiesbeck and E. Heidrich, "Wide-band multiport antenna characterization by polarimetric RCS measurements," *Antennas and Propagation, IEEE Transactions on,* vol. 46, pp. 341-350, 2002.

[22] H.C. Lu and T.H. Chu, “Antenna gain and scattering measurement using reflective three-antenna method,” *Antennas and Propagation Society International Symposium*, 1999, *AP*-S, vol. 371, pp. 374-377.

[23] E. Heidrich, and W. Wiesbeck, “Features of advanced polarimetric RCS-antenna measurements,” *Antennas and Propagation Society International Symposium, 1989. AP-S. Digest* IEEE, pp. 1026-1029.

[24] O. Vicencio, and J. Romeu, “Application of RCS measurement method for characterization of small antennas,” *Antennas and Propagation Society International Symposium, 2008. AP-S*, pp. 1-4.

[25] R. Hansen, “Relationships between antennas as scatterers and as radiators,” *IEEE Proceedings*, vol. 77, no. 5, 1989, pp. 659-662.

[26] R. Garbacz, “Determination of antenna parameters by scattering cross section measurements,” *IEEE Proceedings*, vol. 111, 1964.

[27] J. Appel-Hansen, “Accurate determination of gain and radiation patterns by radar cross-section measurements,” *Antennas and Propagation, IEEE Transactions*, vol. 27, no. 5, 2002, pp. 640-646.

[28] S. Shrestha, M.D. Balachandran, M. Agarwal, L.H. Zou, and K. Varahramyan, “A method to measure radar cross section parameters of antennas,” *Antennas and Propagation, IEEE Transactions*, vol. 56, no. 11, 2008, pp. 3494-3500.

General conclusion and perspectives

I Conclusion

In this thesis, we first designed and built a new test bench for low-directivity integrated antennas at millimeter-wave frequencies. The test bench consists of a measuring antenna, which is a horn antenna mounted on a Plexiglas arm, which rotates about the antenna under test (AUT). Both antennas are connected via coaxial cables to a vector network analyzer (VNA). If the coaxial cable between the horn antenna and VNA is *inflexible* then either: the Plexiglas arm must comply, which would reduce the angular accuracy of the measurement and is therefore unacceptable; or, the connector to the VNA might break, which would be expensive.

Three possible solutions to this problem are evident. We could use:

- ✓ A flexible cable rather than an inflexible cable – this was our first solution but while it can give good measurements of the modulus of the gain, it results in some instability in the phase measurements.
- ✓ A rotating and translating connector between the VNA and cable – this does not exist today and might be expensive to fabricate.
- ✓ A structure in which (part of) the VNA can rotate with the cable.

We therefore designed a second test-bench based on the third of these principles which involved two VNA modules, one of which rotates with the cable, and the other of which is just next to the AUT.

As described in the thesis, the main problem with radiation gain characterization for millimeter-wave integrated antennas is that the measuring system has metallic elements of enormous size compared with the size of the AUTs. Such measuring equipment which produces a masking effect and limits the available range of measuring angles.

To overcome this limitation, we proposed two customized probes as a novel feeding tool. The first of these techniques improved the scanning zone from 100° to 166° and at the same time, the proposed probe reduced the ripples due to the diffractions and reflections from the probe's metallic body. The second of these feeding techniques

used a special connector involving a flexible transmission line. This technique further improves the scanning zone to 180° which covers the whole upper-hemi-sphere. Furthermore, this feeding system is much easier to use than a conventional probe system, as it is more portable and more convenient to install in an anechoic chamber. However this technique depends on a modified flip-chip connection, and due to the imperfect fabrication of this connection, there are still some ripples in the measurement results which need further investigation. Finally, we studied the feasibility of a free-cable characterization method: the RCS method via simulation. The AUT connects to a 50 Ω, short and open loads successively. A horn above the AUT records the reflection coefficient of the whole system. However simulation results demonstrated that there is insufficient variation in the ratio of received power to incident power as the load on the AUT is varied in order to make precise measurement with conventional measurement equipment.

II Perspectives

The second method with a flexible transmission-line enabled us to fully characterize the gain pattern in the upper hemi-sphere. However there was significant parasitic radiation in the gain pattern, which is due to the difficulty of accurately aligning the pads of two components of different size. Future improvements of this technique might involve specific designs of the bonding pads on the chip and a more accurate flip-chip bonding.

In our exploration of the RCS method, measuring in time domain might be a possible solution.

The other feeding technique as we mentioned in the state of the art, VCOs connect to an AUT with a flip-chip connection could be tempting, as the same reason as the flexible-t-line flip chip connection, a more rigorous and accurate connection with resized pads will be necessary.

Finally optically-fed technique is quite promising if the optical fibre could be integrated with the photodetector and AUT.

Étude d’un banc de caractérisation d’antennes intégrées miniatures aux fréquences millimétriques

Lors de cette thèse, on a développé un banc automatisé de relevé du diagramme de rayonnement particulièrement pour des antennes millimétriques avec faible directivité. On propose trois méthodes d’alimentation. La première méthode développée a été de concevoir une nouvelle sonde ayant un accès micro-coaxial de plus de 5cm afin de réduire la zone de masquage au minimum. Associée à une configuration de type flip-chip inversée, cette méthode a permis d’avoir une réduction de la zone de masquage de 80° à 20°. La deuxième méthode a été de concevoir une liaison souple par film souple de Kapton. Cette méthode présente l’avantage de placer une plus grande partie des connexions métalliques sous un plan de masse, mais nécessite une connexion optimale à la puce. Les résultats obtenus présentent une zone de masquage pratiquement inexistante, et sont conformes à l’état de l’art. La troisième méthode SER est basée sur la mesure de l’antenne sans placer de sondes ou de connecteurs spéciaux, mais en utilisant un système à charges connues. La simulation nous montre qu'il nous manque une dynamique par ces trois charges.

Mots clés : Antennes millimétriques, diagramme de rayonnement, sonde, ligne de transmission souple, SER.

Development of a test bench for characterization of integrated antennas at millimeter-wave frequencies

In this thesis, we designed and built a new 3D test bench, particularly for low-directivity integrated antennas at millimeter-wave frequencies. We proposed three feeding techniques for the antenna under test (AUT): a probe-fed technique, a flexible-transmission-line-fed technique and a radar-cross-section (RCS) method. The probe-fed method was developed with a customized probe, which involves an elongated (50 mm) coaxial line between the probe tip and the probe body, wherein the probe body is reversed (relative to the conventional measurement configuration) so it lies below the plane of the AUT. This method reduces the range of angles that are masked from 80° (for a conventional probe setup) to 20°. The second method was developed using a flexible transmission line with a modified flip-chip connection to the AUT. This method completely eliminates the masked zone. The third method characterizes the radiation pattern using a radar cross-section (RCS) method. This method requires neither a probe system nor connectors. However the simulation results demonstrate that there is insufficient variation in the ratio of received power to incident power as the load on the AUT is varied in order to make precise measurement with conventional measurement equipment.

Key words: Millimeter-wave antenna measurement, antenna radiation pattern, probe-fed technique, flexible transmission line, RCS.